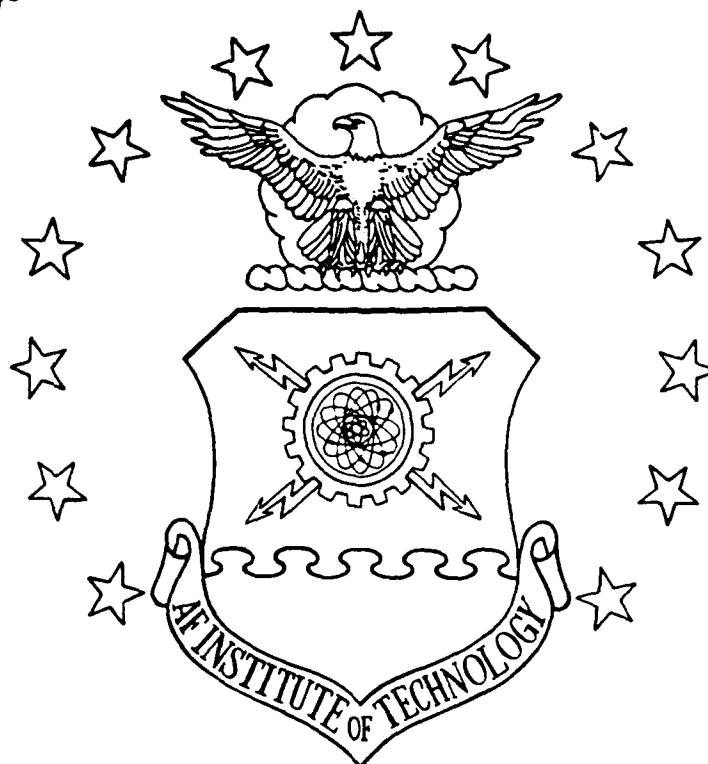


BTTC FILE COPY

AD-A206 138



NUMERICAL STUDY OF THE INFLUENCE OF
LEADING AND TRAILING EDGE FLAPS ON
THE PERFORMANCE OF AIRFOILS

THESIS

Faran Hafeez
Flight Lieutenant, PAF

AFIT/GAE/AA/89M-2

DISTRIBUTION STATEMENT A

Approved for public release
Distribution Unlimited

DEPARTMENT OF THE AIR FORCE
AIR UNIVERSITY

AIR FORCE INSTITUTE OF TECHNOLOGY

Wright-Patterson Air Force Base, Ohio

DTIC
ELECTE
APR 04 1989
D C

89 4 03 046

AFIT/GAE/AA/89M-2

①

DTIC
ELECTE
APR 04 1989
S D
D &

NUMERICAL STUDY OF THE INFLUENCE OF
LEADING AND TRAILING EDGE FLAPS ON
THE PERFORMANCE OF AIRFOILS

THESIS

Faran Hafeez
Flight Lieutenant, PAF

AFIT/GAE/AA/89M-2

Approved for public release; distribution unlimited

NUMERICAL STUDY OF THE INFLUENCE OF LEADING AND TRAILING
EDGE FLAPS ON THE PERFORMANCE OF AIRFOILS

THESIS

Presented to the Faculty of the School of Engineering
of the Air Force Institute of Technology
Air University
in Partial Fulfillment of the
Requirements for the Degree of
Master of Science in Aeronautical Engineering

Faran Hafeez, B.E.
Flight Lieutenant, PAF

March 1989

Accession For	
NTIS	<input checked="checked" type="checkbox"/>
CRA&I	<input type="checkbox"/>
DTIC	<input type="checkbox"/>
TAB	<input type="checkbox"/>
Unannounced	<input type="checkbox"/>
Justification	
By _____	
Distribution /	
Availability Codes	
Dist	Avail and/or Special
A-1	

Approved for Public release; distribution unlimited

Preface

The purpose of this study is to develop a code based on the Approximate Navier Stokes (ANS) equations, to allow flow computation at low Reynolds Number (less than 500,000) about highly cambered airfoils. The camber may either be the airfoil characteristic or created by deflecting portions of the Leading edge (Slat) or Trailing edge (Flap), or both.

This study specifically looks at the highly cambered Wortman FX 63-137 airfoil, fitted with flaps and slats at various combinations of deflections and angles of attack. The flow has been computed using the ANS equations in delta form of the Vorticity Stream Function equations. Good agreement with experimental results has been obtained for small angles of attack.

The significance of this study is based on the fact that recently there has been an increased application of low Reynolds Number aerodynamics, Remotely Piloted Vehicles (RPV's), Helicopter rotors and turbine blades are only few of such applications. This, combined with the dearth of knowledge in this area has created an environment where detailed information of the flow's structure is needed. It is hoped that this study will help fill a portion of this knowledge gap by providing to the practicing aerodynamicist and experimenters, the tool to allow numerical flow prediction, and a reference data set on the wortman airfoil, which is contained herein.

I would like to thank Dr. A. Halim for his supervision and able guidance during this study, Dr. Shang who sponsored this research and extended to me more than ample computer resources and foremost his knowledge, and encouragement, Capt. Phil Beran who patiently heard my problems and suggested remedies, and last but not the least my wife, who has endured rather alone, some toughest of times and has patiently supported me during these long months.

Finally I dedicate this work to my parents, whose prayers and blessings have helped me reach this stage.

Table of Contents

	Page
Preface	ii
List of Figures	vii
List of Tables	xii
List of Symbols	xiii
Abstract	xvi
I. Introduction	1
Purpose and Scope	2
Significance	2
Leading Edge Device (Slat)	5
Trailing Edge Device (Flap)	5
II. Analysis	10
Basic Equations	10
Non-Dimensionalization	10
Stream Function and Vorticity Equations	11
Coordinate Transformation	13
Parabolization	13
III. Numerical Solution	17
Grid Generation	17
Airfoil Deflections	18
Wake Profile	21
Numerical Method	26
Time Dependent Approach	26
Steady State Approach	27
Discretization	28
Boundary Conditions	30
Airfoil Surface	30
Outer Boundary	31
Outflow Boundary	32
Wake (Branch Cut)	33
Initial Conditions	35
Turbulence Modeling	35
Transition	36
Pressure and Force Computations	38
Boundary conditions for Pressure	39
Convergence Criterion	41
IV. Results and Discussion	42
Code Verification	42

Case-1: Laminar Flow ($Re = 12,500$)	42
Case-2: Turbulent Flow ($Re = 6.5 \times 10^5$)	44
Case-3: Non-Symmetric Turbulent Flow, Airfoil ($Re = 200,000$)	52
Results	52
Wortman Airfoil no Deflections	54
Wortman Airfoil $\delta_{1e} = 5^\circ$, $\delta_{1e} = 0^\circ$	54
Wortman Airfoil $\delta_{1e} = 5^\circ$, $\delta_{1e} = 20^\circ$	57
Effect of Angle of Attack	57
On Lift Coefficient	57
On Drag Coefficient	67
On Moment Coefficient	68
On Pressure Peak	68
On Laminar Separation	70
Effect of Slat Deflection	72
On Lift Coefficient	72
On Drag Coefficient	74
On Moment Coefficient	75
On Pressure Peak	75
On Separation Point	76
Effect of Flap Deflection	76
On Lift Coefficient	76
On Drag Coefficient	77
On Moment Coefficient	79
On Pressure Peak	79
On Separation Point	79
V. Conclusions and Recommendations	81
Appendix A: Derivation of Stream Function and Vorticity Transport Equations	83
Appendix B: Coordinate Transformation Relations	86
Appendix C: Program Airfoil, Fortran Listing	87
Appendix D: Comparison of Coordinates, Before and After Smoothing	98
Appendix E: Linearization of Vorticity and Stream Function Equations	100
Appendix F: Derivation of Poisson Equation for Pressure	102
Appendix G: Derivation of Force and Moment Coefficients	105
Appendix H: Contour plots; Stream Function, Velocity and Vorticity	110

Appendix 1:	Variation of Pressure and Skin friction	
	Coefficient for Wortman FX 63-137	
	Airfoil	127
Bibliography		144
Vita		147

List of Figures

Figure	Page
1. Chord Reynolds Number vs. Mach Number for Variety of Flight Vehicles	3
2. Transformation from Physical to Computational Domain	14
3. Comparison of Un-deflected and Deflected Wortman FX 63-137 Airfoil	19
4. Comparison of Local Slope, Before and After Smoothing	20
5. Wortman FX 63-137 Airfoil, Before and After Smoothing	20
6. Wake Profile	22
7. Boundaries of C-type Grid	24
8. C-Grid Created by the Elliptic-Grid Generator ...	24
9. C-Grid Generated Using Hyperbolic-Grid Generator.	25
10. Differential Element	28
11. Grid for NACA-12 Airfoil	43
12. Comparison of Skin Friction Coefficient Distribution, Present with Ref. [11]	44
13. Comparison of Constant Stream Function Contours NACA-12 Airfoil, $Re=12,500$	45
14. Grid Flat Plate	46
15. Comparison of Skin Friction Coefficient vs. x/c Flat Plate, $Re = 6.5 \times 10^5$	48
16. Comparison of Velocity Profile ($x/c=0.98$) Flat Plate, $Re = 6.5 \times 10^5$	49
17. Comparison of Eddy Viscosity Profile ($x/c=0.98$) Flat Plate, $Re = 6.5 \times 10^5$	50
18. Pressure Coefficient Comparison for Wortman FX 63-137 Airfoil	53

19.	279x60 Grid Wortman FX 63-137 Airfoil	55
20.	Grid Detail Wortman FX 63-137 Airfoil	56
21.	Comparison of Lift Coefficient vs. Angle of Attack Wortman Airfoil, $\delta_{t_e}=0^\circ$, $\delta_{l_e}=0^\circ$	58
22.	Comparison of Drag Coefficient vs. Angle of Attack Wortman Airfoil, $\delta_{t_e}=0^\circ$, $\delta_{l_e}=0^\circ$	59
23.	Comparison of Moment Coefficient vs. Angle of Attack Wortman Airfoil, $\delta_{t_e}=0^\circ$, $\delta_{l_e}=0^\circ$	60
24.	Comparison of Lift Coefficient vs. Angle of Attack Wortman Airfoil, $\delta_{t_e}=0^\circ$, $\delta_{l_e}=5^\circ$	61
25.	Comparison of Drag Coefficient vs. Angle of Attack Wortman Airfoil, $\delta_{t_e}=0^\circ$, $\delta_{l_e}=5^\circ$	62
26.	Comparison of Moment Coefficient vs. Angle of Attack Wortman Airfoil, $\delta_{t_e}=0^\circ$, $\delta_{l_e}=5^\circ$	63
27.	Comparison of lift Coefficient vs. Angle of Attack Wortman Airfoil, $\delta_{t_e}=20^\circ$, $\delta_{l_e}=5^\circ$	64
28.	Comparison of Drag Coefficient vs. Angle of Attack Wortman Airfoil, $\delta_{t_e}=20^\circ$, $\delta_{l_e}=5^\circ$	65
29.	Comparison of Moment Coefficient vs. Angle of Attack Wortman Airfoil, $\delta_{t_e}=20^\circ$, $\delta_{l_e}=5^\circ$	66
30.	Effect of Slat and Flap Deflections on Lift Coefficient	73
31.	Effect of slat and flap Deflections on Drag Coefficient	74
32.	Effect of slat and flap Deflections on Moment Coefficient	75
33.	Velocity vector plots, Wortman airfoil $\delta_{t_e}=20^\circ$, $\delta_{l_e}=5^\circ$	78
34.	Forces acting on Airfoil Surface	105
35.	Moment acting on Airfoil Element	108
36.	Constant Stream Function, Velocity and Vorticity Contour Plots for Wortman FX 63-137 Airfoil, $\alpha = -4^\circ$, $\delta_{l_e} = 0^\circ$, $\delta_{t_e} = 0^\circ$, $Re = 1 \times 10^5$	111

37.	Constant Stream Function, Velocity and Vorticity Contour Plots for Wortman FX 63-137 Airfoil, $\alpha = 0^\circ$, $\delta_{1e} = 0^\circ$, $\delta_{te} = 0^\circ$, $Re = 1 \times 10^5$	112
38.	Constant Stream Function, Velocity and Vorticity Contour Plots for Wortman FX 63-137 Airfoil, $\alpha = 4^\circ$, $\delta_{1e} = 0^\circ$, $\delta_{te} = 0^\circ$, $Re = 1 \times 10^5$	113
39.	Constant Stream Function, Velocity and Vorticity Contour Plots for Wortman FX 63-137 Airfoil, $\alpha = 8^\circ$, $\delta_{1e} = 0^\circ$, $\delta_{te} = 0^\circ$, $Re = 1 \times 10^5$	114
40.	Constant Stream Function, Velocity and Vorticity Contour Plots for Wortman FX 63-137 Airfoil, $\alpha = 12^\circ$, $\delta_{1e} = 0^\circ$, $\delta_{te} = 0^\circ$, $Re = 1 \times 10^5$	115
41.	Constant Stream Function, Velocity and Vorticity Contour Plots for Wortman FX 63-137 Airfoil, $\alpha = 16^\circ$, $\delta_{1e} = 0^\circ$, $\delta_{te} = 0^\circ$, $Re = 1 \times 10^5$	116
42.	Constant Stream Function, Velocity and Vorticity Contour Plots for Wortman FX 63-137 Airfoil, $\alpha = -4^\circ$, $\delta_{1e} = 5^\circ$, $\delta_{te} = 0^\circ$, $Re = 1 \times 10^5$	117
43.	Constant Stream Function, Velocity and Vorticity Contour Plots for Wortman FX 63-137 Airfoil, $\alpha = 0^\circ$, $\delta_{1e} = 5^\circ$, $\delta_{te} = 0^\circ$, $Re = 1 \times 10^5$	118
44.	Constant Stream Function, Velocity and Vorticity Contour Plots for Wortman FX 63-137 Airfoil, $\alpha = 4^\circ$, $\delta_{1e} = 5^\circ$, $\delta_{te} = 0^\circ$, $Re = 1 \times 10^5$	119
45.	Constant Stream Function, Velocity and Vorticity Contour Plots for Wortman FX 63-137 Airfoil, $\alpha = 8^\circ$, $\delta_{1e} = 5^\circ$, $\delta_{te} = 0^\circ$, $Re = 1 \times 10^5$	120
46.	Constant Stream Function, Velocity and Vorticity Contour Plots for Wortman FX 63-137 Airfoil, $\alpha = 12^\circ$, $\delta_{1e} = 5^\circ$, $\delta_{te} = 0^\circ$, $Re = 1 \times 10^5$	121
47.	Constant Stream Function, Velocity and Vorticity Contour Plots for Wortman FX 63-137 Airfoil, $\alpha = -4^\circ$, $\delta_{1e} = 5^\circ$, $\delta_{te} = 20^\circ$, $Re = 1 \times 10^5$	122
48.	Constant Stream Function, Velocity and Vorticity Contour Plots for Wortman FX 63-137 Airfoil, $\alpha = 0^\circ$, $\delta_{1e} = 5^\circ$, $\delta_{te} = 20^\circ$, $Re = 1 \times 10^5$	123

49. Constant Stream Function, Velocity and Vorticity
Contour Plots for Wortman FX 63-137 Airfoil,
 $\alpha = 4^\circ$, $\delta_{1e} = 5^\circ$, $\delta_{te} = 20^\circ$, $Re = 1 \times 10^5$ 124
50. Constant Stream Function, Velocity and Vorticity
Contour Plots for Wortman FX 63-137 Airfoil,
 $\alpha = 8^\circ$, $\delta_{1e} = 5^\circ$, $\delta_{te} = 20^\circ$, $Re = 1 \times 10^5$ 125
51. Constant Stream Function, Velocity and Vorticity
Contour Plots for Wortman FX 63-137 Airfoil,
 $\alpha = 12^\circ$, $\delta_{1e} = 5^\circ$, $\delta_{te} = 20^\circ$, $Re = 1 \times 10^5$ 126
52. Pressure Coefficient (C_p) and Skin Friction
Coefficient (C_f) vs. x/c , Wortman Airfoil,
 $\alpha = -4^\circ$, $\delta_{1e} = 0^\circ$, $\delta_{te} = 0^\circ$, $Re = 1 \times 10^5$ 128
53. Pressure Coefficient (C_p) and Skin Friction
Coefficient (C_f) vs. x/c , Wortman Airfoil,
 $\alpha = 0^\circ$, $\delta_{1e} = 0^\circ$, $\delta_{te} = 0^\circ$, $Re = 1 \times 10^5$ 129
54. Pressure Coefficient (C_p) and Skin Friction
Coefficient (C_f) vs. x/c , Wortman Airfoil,
 $\alpha = 4^\circ$, $\delta_{1e} = 0^\circ$, $\delta_{te} = 0^\circ$, $Re = 1 \times 10^5$ 130
55. Pressure Coefficient (C_p) and Skin Friction
Coefficient (C_f) vs. x/c , Wortman Airfoil,
 $\alpha = 8^\circ$, $\delta_{1e} = 0^\circ$, $\delta_{te} = 0^\circ$, $Re = 1 \times 10^5$ 131
56. Pressure Coefficient (C_p) and Skin Friction
Coefficient (C_f) vs. x/c , Wortman Airfoil,
 $\alpha = 12^\circ$, $\delta_{1e} = 0^\circ$, $\delta_{te} = 0^\circ$, $Re = 1 \times 10^5$ 132
57. Pressure Coefficient (C_p) and Skin Friction
Coefficient (C_f) vs. x/c , Wortman Airfoil,
 $\alpha = 16^\circ$, $\delta_{1e} = 0^\circ$, $\delta_{te} = 0^\circ$, $Re = 1 \times 10^5$ 133
58. Pressure Coefficient (C_p) and Skin Friction
Coefficient (C_f) vs. x/c , Wortman Airfoil,
 $\alpha = -4^\circ$, $\delta_{1e} = 5^\circ$, $\delta_{te} = 0^\circ$, $Re = 1 \times 10^5$ 134

59. Pressure Coefficient (C_p) and Skin Friction
Coefficient (C_f) vs. x/c , Wortman Airfoil,
 $\alpha = 0^\circ$, $\delta_{1e} = 5^\circ$, $\delta_{te} = 0^\circ$, $Re = 1 \times 10^5$ 135
60. Pressure Coefficient (C_p) and Skin Friction
Coefficient (C_f) vs. x/c , Wortman Airfoil,
 $\alpha = 4^\circ$, $\delta_{1e} = 5^\circ$, $\delta_{te} = 0^\circ$, $Re = 1 \times 10^5$ 136
61. Pressure Coefficient (C_p) and Skin Friction
Coefficient (C_f) vs. x/c , Wortman Airfoil,
 $\alpha = 8^\circ$, $\delta_{1e} = 5^\circ$, $\delta_{te} = 0^\circ$, $Re = 1 \times 10^5$ 137
62. Pressure Coefficient (C_p) and Skin Friction
Coefficient (C_f) vs. x/c , Wortman Airfoil,
 $\alpha = 12^\circ$, $\delta_{1e} = 5^\circ$, $\delta_{te} = 0^\circ$, $Re = 1 \times 10^5$ 138
63. Pressure Coefficient (C_p) and Skin Friction
Coefficient (C_f) vs. x/c , Wortman Airfoil,
 $\alpha = -4^\circ$, $\delta_{1e} = 5^\circ$, $\delta_{te} = 20^\circ$, $Re = 1 \times 10^5$ 139
64. Pressure Coefficient (C_p) and Skin Friction
Coefficient (C_f) vs. x/c , Wortman Airfoil,
 $\alpha = 0^\circ$, $\delta_{1e} = 5^\circ$, $\delta_{te} = 20^\circ$, $Re = 1 \times 10^5$ 140
65. Pressure Coefficient (C_p) and Skin Friction
Coefficient (C_f) vs. x/c , Wortman Airfoil,
 $\alpha = 4^\circ$, $\delta_{1e} = 5^\circ$, $\delta_{te} = 20^\circ$, $Re = 1 \times 10^5$ 141
66. Pressure Coefficient (C_p) and Skin Friction
Coefficient (C_f) vs. x/c , Wortman Airfoil,
 $\alpha = 8^\circ$, $\delta_{1e} = 5^\circ$, $\delta_{te} = 20^\circ$, $Re = 1 \times 10^5$ 142
67. Pressure Coefficient (C_p) and Skin Friction
Coefficient (C_f) vs. x/c , Wortman Airfoil,
 $\alpha = 12^\circ$, $\delta_{1e} = 5^\circ$, $\delta_{te} = 20^\circ$, $Re = 1 \times 10^5$ 143

List of Tables

Table	page
1. Comparison of Constants: Modified and Un-modified Baldwin-Lomax Model	52
2. Comparison of Separation and Reattachment Points Wortman Airfoil, $\delta_{te}=0^\circ$, $\delta_{le}=0^\circ$	69
3. Comparison of Separation and Reattachment Points Wortman Airfoil, $\delta_{te}=0^\circ$, $\delta_{le}=5^\circ$	71
4. Comparison of Separation and Reattachment Points Wortman Airfoil, $\delta_{te}=20^\circ$, $\delta_{le}=5^\circ$	72
5. Lower Surface Coordinates Wortman FX 63-137 Airfoil	98
6. Upper Surface Coordinates Wortman FX 63-137 Airfoil	99

List of Symbols

<u>Symbol</u>	<u>Definition</u>
c	Airfoil chord length
C_d	Drag Coefficient
C_f	Skin Friction Coefficient
C_l	Lift Coefficient
C_m	Moment Coefficient
C_p	Pressure Coefficient
F_f	Force due to skin friction
F_p	Force due to pressure
F_x	Force in direction of body x-axis
F_y	Force in direction of body y-axis
J	Transformation metrics jacobian
LHS	Left hand side of equation
p	Pressure
r	moment arm
Re	Reynolds Number
RHS	Right hand side of equation
S	Reference surface area
t	Time
u	Cartesian x-component of velocity
U	Total velocity
U_∞	Free stream velocity
v	Cartesian y-component of velocity
x	Cartesian streamwise coordinate

y	Cartesian normal coordinate
α	Angle of attack and metric definition
β	Transformation metrics definition
γ	Transformation metrics definition
γ_{tr}	Turbulence transition factor
δ	Difference in a property between two time or iteration levels
δ_{le}	Leading edge (flap) deflection angle
δ_{te}	Trailing edge (flap) deflection angle
$\Delta\eta$	Grid spacing in normal direction
$\Delta\xi$	Grid spacing in streamwise direction
ϵ	Turbulent eddy viscosity
η	Curvilinear coordinate in Computational domain, normal to body
θ_i	Local slope of i^{th} node on airfoil surface
θ_m	Angle between airfoil body axis and moment arm
ξ	Curvilinear coordinate in computational domain, tangent to body (streamwise direction)
μ	Molecular dynamic viscosity
ρ	Density
ψ	Stream function
ω	Vorticity

Superscripts

n	Time or iteration level
\circ	Vorticity equation
\bullet	Stream function equation
$*$	Dimensional variable

Subscripts

i	Node index in streamwise direction (tangent to body)
j	Node index in normal direction (normal to body)
∞	Property with Free stream value
t	Partial derivative with respect to time
x	Partial derivative with respect to x
y	Partial derivative with respect to y
η	Partial derivative with respect to η
ξ	Partial derivative with respect to ξ

Abstract

✓
The purpose of this study is to develop a code based on the Approximate Navier Stokes (ANS) equations (in the Vorticity Stream Function delta form). The Wortman FX 63-137 airfoil fitted with leading and trailing edge devices has been analyzed at low Reynolds Number (100,000) at various angles of attack and various deflection angles. results are compared to the experimental data. The agreement is very good at small angles of attack. However, at large angles of attack the disparity is larger, and improvements have been recommended which will resolve this disparity. Overall the present scheme produces very reasonable results, with good repeatability and fast convergence, and has the potential of being developed into an effective design tool. Thesis. (cdc)

X

NUMERICAL STUDY OF THE INFLUENCE OF LEADING AND TRAILING
EDGE FLAPS ON THE PERFORMANCE OF AIRFOIL

1. Introduction

The aim of every aerodynamicist is to be able to predict the aerodynamic characteristics of a given design. Accurate prediction of these parameters is very important as they form the basis for the designs of the aircraft's control and propulsion systems, and hence effect the safety of the vehicle.

The tools available to an aerodynamicist are the wind tunnels and computational methods. To date, most aircraft designs depend on wind tunnel testing and empirical data, but, lately, some designs have also been developed primarily through the use of computational methods. This has largely been possible due to the enormous growth of research and success in the area of Computational Fluid Dynamics (CFD). Computational methods are more economical and faster compared to wind tunnel testing and give much more detailed information on flow characteristics. Geometric changes and their effects on flow can also be seen very quickly, resulting in reliable design decisions.

Computational methods can be broken down into two

distinct techniques, finite element and finite difference algorithms. This research is based on the finite difference approach and is an attempt to develop a fast and efficient algorithm for computing flow about arbitrary bodies (primarily airfoils), using the approximate Navier-Stokes (ANS) equations. These equations are not as accurate as the Navier-Stokes (NS), but the advantages are that the ANS equations offer significantly reduced computational effort and storage compared to the complete Navier Stokes equations.

Purpose and Scope

The basic purpose of this research is to develop a code which would allow flow computation at low Reynolds Number (less than 500,000) about highly cambered airfoil sections. The high camber is usually produced by installing leading edge (Slats) and trailing edge (Flaps) devices to the basic section. These devices can then be rotated to effectively change the shape (camber) and hence the aerodynamic characteristics of the airfoil.

Significance. Motivation for this research is the fact that extensive experimental and empirical data is available for airfoils with flaps and slats at high Reynolds number, but very little is known about the aerodynamic behavior of highly cambered airfoils in low Reynolds number flow. The second factor was the ready availability of experimental data for the Wortman FX 63-137 in various configurations and at

varying Reynolds number from the University of Notre Dame [16] and the College of Aeronautics, Cranfield, England [28]. The third and most important factor, is that recently there has been recently increased application of low Reynold number aerodynamics, remotely piloted vehicles (RPV), helicopter rotors, turbine blades and wind turbines are only few of such applications. These are all characterized as having either short chord length or low operating speed or both. A diagram showing the range of Reynolds Numbers for several applications appears below as Figure 1. Therefore, it is very natural to anticipate a vast need for performance characteristics in the low Reynolds number regime, and how these may be enhanced using various techniques.

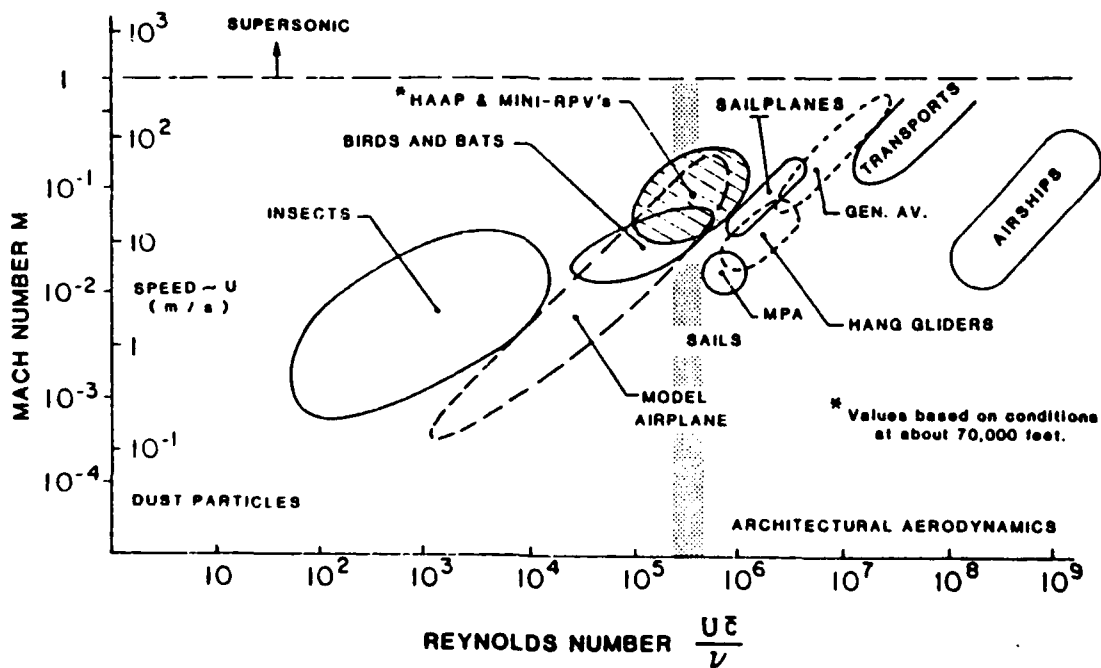


Figure 1 Chord Reynolds Number vs. Mach Number for a variety of flight Vehicles

Before the issue of performance enhancement can be discussed, it would be appropriate to highlight a typical characteristic of airfoils in low Reynolds Number flow, the formation of separation bubbles and their role in determining the flow pattern and the performance characteristics of the airfoil.

Extensive research has been carried out on separation bubbles, and it has been determined that the significant parameters affecting the formation of separation bubbles are the angle of attack, profile geometry, Reynolds Number and free stream turbulence [16:3]. The separation bubbles are usually classified as either long or short, Arena and Muller [3] summarize that long bubbles tend to decrease lift due to lower suction peak, while short bubbles have negligible effect on lift or suction peak.

The separation bubble forms as the fluid moving over the airfoil encounters an adverse pressure gradient. If the flow does not possess sufficient momentum to overcome this gradient, the laminar boundary layer separates from the surface and then undergoes transition to turbulent flow. It then gains momentum by entraining fluid from the free stream, and if the fluid gains sufficient momentum to overcome the gradient, it will reattach to the airfoil surface. Hence the process of separation and reattachment, creates a reverse flow region over the airfoil surface, usually known as the separation bubble. On the other hand, if the flow is

unable to gain sufficient momentum to reattach, then it remains separated. This type of separation is known to yield an open wake of an airfoil and is the primary cause of stall.

The performance of an airfoil may be enhanced by management of the boundary layer using any one, or combination, of the following techniques.

- (a) Attachment of leading and or trailing edge devices to the airfoil.
- (b) Use of surface roughness.
- (c) Suction and blowing.

Because this study is concerned primarily with the effects of leading and trailing edge devices, it would be appropriate to draw on general conclusions based on previous work done in this area.

Leading Edge Device (Slat). The primary purpose of these devices is to avoid or delay leading edge separation, particularly at low Reynolds number. Positive deflections of the leading edge (downwards) causes an effective reduction of the angle of attack relative to the airfoil's leading edge, and leads to downstream shift of the separation point.

Trailing Edge Device (Flap). Positive deflection of the flap (downward) causes an increase in pressure acting on the lower surface and a decrease of pressure on the upper surface. This produces an increase in the circulation around the airfoil, thereby increasing lift, but only at the

penalty of increased drag. The increase in drag is due to an increase in the effective angle of attack of the trailing section of the airfoil, and low pressure in the wake downstream of the flap. The overall effect of the flap is to shift the lift curve, without changing the slope. This may be predicted by the following relation, derived using the thin airfoil theory [12:492-517,14].

$$C_L = 2\pi(\alpha + 2z)$$

where α is the angle of attack and z is the maximum camber

It can be seen from this relation that the lift coefficient will increase linearly as the camber is increased. It should be mentioned that this relation is only applicable to thin airfoils in ideal flow, but is not applicable to highly cambered airfoils in viscous flow.

Viscous effects are generally nonlinear and therefore cannot be approximated by such simple linear relations. Hence, to be able to predict complex viscous flow patterns effectively, we have to turn to mathematical models using either the Navier-Stokes or the approximate Navier-Stokes (ANS) equations. The main thrust of this study is to use the ANS model to approximate the flow pattern and the performance characteristics of the Wortman FX 63-137 airfoil, which has been appropriately modified with slats extending to 13% and flaps measuring 25% chord (a Fortran program named "AIRFOIL" has been developed to carry out deflections of the

airfoil). To be able to analyze this problem the code developed by Halim [11] has been extended from the purely steady state laminar symmetric flow solver to the present version. The present version is flexible, easy to use, and can handle nonsymmetric turbulent flows. Using this code in either steady state or time accurate unsteady solutions can be obtained and either Neumann or Dirichlet Boundary conditions can be enforced. Routines have also been added to compute pressure distribution and the global parameters lift (C_L), drag (C_D) and moment (C_m) coefficients. Also as a part of this effort an elliptic grid generator has been developed, which allows the user complete control over all aspects of the grid generation process. A special wake model handles the interaction of the trailing edge deflection and the angle of attack to produce a C-type grid which honors these conditions.

The code developed in this study is based on the approximate Navier-Stokes equations in the vorticity, stream function delta form and has been validated by computing and comparing three different types of flows: symmetric, low Reynolds Number ($Re=12,500$), laminar flow around NACA-12 airfoil, turbulent flow on a finite flat plate ($Re=6.5 \times 10^5$) and turbulent flow around the nonsymmetric Wortman FX 63-137 airfoil ($Re=200,000$). Each of these test cases probes one or more specific areas of the code, which allows a systematic validation process. The results obtained in each

of the three cases are in very good agreement with previous data.

Having completed the validation process, flow around the Wortman airfoil was computed at $Re=100,000$. Because of time constraint, one flap deflection of 20 degrees, one slat deflection of 5 degrees was analyzed at different angles of attack, in addition to the case of no deflection. Results obtained are compared to previous data [16,26], agreement with experimental data is good at lower angles of attack, with under prediction of C_L and over prediction of C_D and C_m at higher angles of attack ($-4 < \alpha < 8$ deg).

Based on the present results, an attempt has been made to look at the flow structure more closely, which is not always possible experimentally (the measurement process may alter the flow pattern and gives rise to un-certainty [7]). It is hoped that the insight so gained will benefit future experiments and vehicle designs.

The present system of predicting flow can be improved so as to allow good prediction capabilities by using different turbulence models and some minor improvements in the algorithm. Overall, it can be said that the present code has good potential of developing into an effective design tool and this study is only the first step in this direction.

The following chapters discuss at length, details of the mathematical model, the solution algorithm, the validation process and the results for the Wortman airfoil,

finally suggestions have been made to enhance the present work and specific areas identified in which an in-depth analysis is required.

II Analysis

In this chapter, the mathematical model used in this study will be developed, starting from the fundamental equations for viscous flow and building up to the model finally used in finite difference form.

Basic Equations

The fundamental equations governing two-dimensional incompressible flow of a fluid with no body forces and constant properties are the Navier Stokes (NS) equations [20:65].

$$\text{continuity} \quad \frac{\partial u}{\partial x} + \frac{\partial v}{\partial y} = 0$$

$$\text{x-mom.} \quad \frac{\partial u}{\partial t} + u \frac{\partial u}{\partial x} + v \frac{\partial u}{\partial y} = -\frac{1}{\rho} \frac{\partial P}{\partial x} + \frac{\partial}{\partial x} \left(\mu \frac{\partial u}{\partial x} \right) + \frac{\partial}{\partial y} \left(\mu \frac{\partial u}{\partial y} \right) \quad (1)$$

$$\text{y-mom.} \quad \frac{\partial v}{\partial t} + u \frac{\partial v}{\partial x} + v \frac{\partial v}{\partial y} = -\frac{1}{\rho} \frac{\partial P}{\partial y} + \frac{\partial}{\partial x} \left(\mu \frac{\partial v}{\partial x} \right) + \frac{\partial}{\partial y} \left(\mu \frac{\partial v}{\partial y} \right)$$

It should be noted that equations (1) are in dimensional form and viscosity has not been assumed constant. This has been done to facilitate simulation of turbulent flow, using the concept of eddy viscosity.

Non-dimensionalization

The above equations (1) can be non-dimensionalized using

the following normalization definitions.

$$\begin{aligned}
 x &= \frac{x^*}{c} & y &= \frac{y^*}{c} & u &= \frac{u^*}{u_{\infty}^*} & v &= \frac{v^*}{v_{\infty}^*} \\
 P &= \frac{P^*}{\rho_{\infty}^* u_{\infty}^{*2}} & \rho &= \frac{\rho^*}{\rho_{\infty}^*} & \mu &= \frac{\mu^*}{\mu_{\infty}^*} & t &= \frac{t^*}{c} u_{\infty}^* \\
 Re &= \frac{\rho_{\infty}^* u_{\infty}^* c}{\mu_{\infty}^*}
 \end{aligned} \tag{2}$$

where c is the characteristic length (airfoil chord: $c = 1$) and subscript ∞ indicates free stream properties.

In the above relations starred (*) variables represent dimensional quantities and non-starred variables represent the nondimensional variables. Equations (2) take the following form after normalization.

$$\frac{\partial u}{\partial x} + \frac{\partial v}{\partial y} = 0 \tag{3b}$$

$$\frac{\partial u}{\partial t} + u \frac{\partial u}{\partial x} + v \frac{\partial u}{\partial y} = \frac{\partial P}{\partial x} + \frac{1}{Re} \frac{\partial}{\partial x} \left(\mu \frac{\partial u}{\partial x} \right) + \frac{\partial}{\partial y} \left(\mu \frac{\partial u}{\partial y} \right) \tag{3a}$$

$$\frac{\partial v}{\partial t} + u \frac{\partial v}{\partial x} + v \frac{\partial v}{\partial y} = \frac{\partial P}{\partial y} + \frac{1}{Re} \frac{\partial}{\partial x} \left(\mu \frac{\partial v}{\partial x} \right) + \frac{\partial}{\partial y} \left(\mu \frac{\partial v}{\partial y} \right) \tag{3c}$$

Stream function and Vorticity transport equations

The above non-dimensionalized equations (3) can be cast into the stream function and vorticity transport equation by differentiating equation (3b) with respect to y and differentiating equation (3c) with respect to x . Subtracting the two resulting equations from each other eliminates the

pressure term, and the rest of the terms can be simplified using the following definitions for vorticity and stream function. (for more details, see Appendix A)

$$\text{(vorticity)} \quad \omega = \frac{\partial v}{\partial x} + \frac{\partial u}{\partial y} \quad (4a)$$

$$\text{(stream function)} \quad u = \frac{\partial \psi}{\partial y} \quad \& \quad v = - \frac{\partial \psi}{\partial x} \quad (4b)$$

where ψ is the stream function and ω the vortic

The Navier-Stokes equations in vorticity and stream function form are

(vorticity equation)

$$\begin{aligned} \omega_t + \psi_y \omega_x - \psi_x \omega_y = & \left(\mu \omega \right)_{xx} + \left(\mu \omega \right)_{yy} \\ & - 2\mu_{xy} \psi_{xy} + \mu_{xx} \psi_{yy} + \mu_{yy} \psi_{xx} \end{aligned} \quad (5a)$$

(stream function equation)

$$\psi_{xx} + \psi_{yy} = \omega \quad (5b)$$

here subscripts indicate differentiation

In the above set of equations (5), the NS equations in primitive variables, (3b) & (3c), transform to the vorticity transport equation (5a). The continuity equation (3a) is satisfied identically by the definition of stream function equation (3a). Thus equations (5) represent two unknown variables ω and ψ in two equations, forming a closed set, provided μ is known from the turbulence modeling. The solution of (5) can be obtained by solving them simultaneously, or through a procedure, that will be

discussed in chapter 4 in detail.

Coordinate transformation

The stream function and vorticity transport equations are in the Cartesian coordinates and therefore can be applied easily to only rectangular domains. To facilitate application to irregular boundaries, a transformation is required that would map the equations and the boundary conditions from the irregular, physical domain to a body conformal coordinate system.

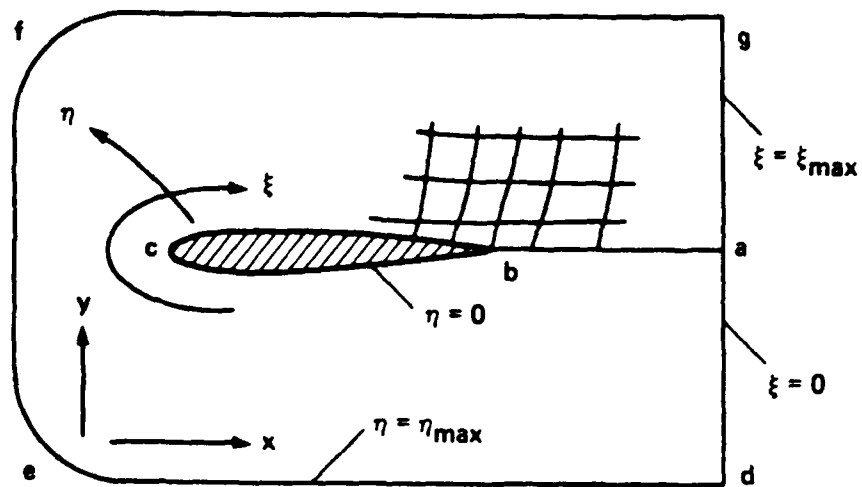
The physical domain represents the actual geometry of the problem and may be of any shape, as shown in Figure 2. Let x and y be the co-ordinate variables in the physical domain and η , ξ be the co-ordinate variables in the computational domain as shown in Figure 2. Then if the following transformation exists;

$$\begin{aligned}\xi &= \xi(x,y) \\ \eta &= \eta(x,y)\end{aligned}$$

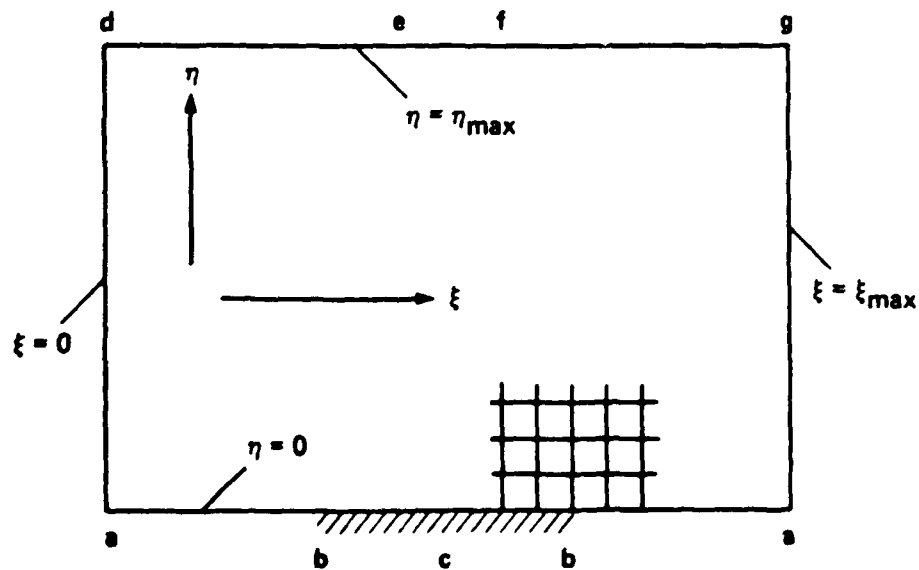
The vorticity stream function equations can be transformed into the computational domain using the chain rule of partial differentiation. This results in the co-ordinate transformation relations (25:122-133) given in Appendix B.

Parabolization

The complete Navier Stokes equations are the most



(a) Physical Domain



(b) Computational Domain

Figure 2 Transformation from physical to computational domain

accurate for any flow situation, but these are very difficult to solve in their complete form. In general, a very large amount of computer storage and computational time is necessary to obtain a solution of these equations [2:420]. However for some situations, assumptions may be made that will reduce these equations to a simpler form. Boundary-layer (BL) equations and the Approximate Navier Stokes (ANS) equations fall into that category. Following are some of the advantages of using the ANS equations [2:420].

- (a) There are fewer terms in the equations, which leads to reduction in computation.
- (b) The equations are parabolic in the streamwise direction, so that their solution can be obtained using spatial-marching techniques. This results in substantial savings of computational time and storage requirements.
- (c) Unlike the boundary-layer equations, which are singular at the point of separation, the ANS equations can easily handle reverse flow.

The derivation of the ANS equations from the NS equations is not as rigorous as the derivation for Boundary-layer equations. However, the following assumptions are usually made to arrive at the ANS form of the NS equations.

- (a) The normal pressure gradient term is retained.

(b) The second derivatives with respect to the streamwise direction are omitted.

The assumptions given above have also been applied in this work, and equations (4) reduce to the following set (after the transformation into general coordinate system and application of ANS assumptions).

stream function

$$\frac{\partial}{\partial \xi} \left(\frac{\alpha}{J} \frac{\partial \psi}{\partial \xi} - \frac{\beta}{J} \frac{\partial \psi}{\partial \eta} \right) + \frac{\partial}{\partial \eta} \left(\frac{\gamma}{J} \frac{\partial \psi}{\partial \eta} - \frac{\beta}{J} \frac{\partial \psi}{\partial \xi} \right) + J\omega = 0 \quad (6a)$$

vorticity transport

$$J \frac{\partial \omega}{\partial \xi} + \frac{\partial \psi}{\partial \eta} \frac{\partial \omega}{\partial \xi} - \frac{\partial \psi}{\partial \xi} \frac{\partial \omega}{\partial \eta} = \frac{1}{Re} \left[\frac{\partial}{\partial \eta} \left(-\frac{\gamma}{J} \frac{\partial \mu \omega}{\partial \eta} \right) \right] \quad (6b)$$

III Numerical solution

In this chapter, numerical grid generation is discussed, followed by the numerical method for solving the vorticity stream function equations, the differencing scheme, the boundary conditions, the turbulence closure. The transition from laminar to turbulent flow, the convergence criterion, computation of pressure and force coefficients.

Grid Generation

As mentioned earlier the purpose of numerical grid generation is to remove the problem of boundary shape from finite-difference methods. Numerically generated grids allow implementation of numerical algorithms on a rectangular computational domain, regardless of the shape and configuration of the physical region [25:v].

Numerical grid generation is not in the scope of this thesis. But efforts were made to develop a grid generator, primarily because a grid was required to solve the present problem. Secondly no available grid generator could handle the specifics of this study, these being.

(a) The ability to numerically regenerate the surface of the airfoil so as to simulate leading and trailing edge deflections.

(b) The grid generator should also be able to handle

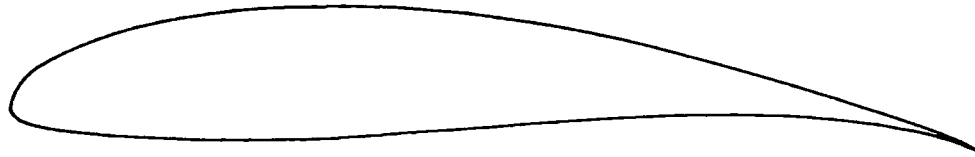
the combined effect of trailing edge deflections and angle of attack on the wake branch cut (C-grid).

(c) Capability to control spacing and clustering of points anywhere in the physical field and on the boundaries.

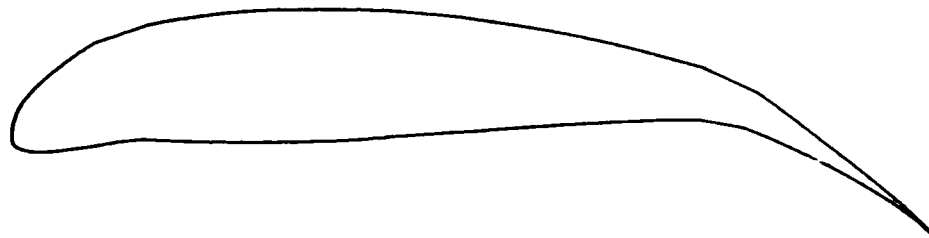
Airfoil Deflections. The solution of problem (a) involves numerical rotation (transformation) of airfoil coordinates about rotation centers based upon given deflection data. A code named "AIRFOIL" was developed (Fortran listing attached as Appendix C), that takes as input the airfoil coordinates, lengths/deflections of the leading and trailing edge devices and regenerates the surface satisfying the given conditions, Figure 3 represents a comparison of the basic Wortman section before and after rotating the leading edge by 15° and trailing edge by 20° using the program AIRFOIL.

The code Airfoil also has the ability to smooth coordinate data, so that C^1 (first derivative) continuity of the metrics is ensured on the surface. The smoothing of coordinates is implemented with an IMSL routine that uses cubic splines and least squares to minimize metric variation. The addition of smoothing was necessitated for to the following reasons.

(a) After rotation of the airfoil coordinates some of the points have to be removed or altered due to overlap or



(a) No deflections



(b) deflections: Leading edge 15° trailing edge 20°

Figure 3 Comparison of un-deflected and deflected Wortman FX63-137 Airfoil

separation. A first cut to this approximation is done as part of the rotation itself, but this does not ensure C^1 continuity, therefore a need arises to apply mathematical smoothing.

(b) The coordinate of the Wortman FX 63-137 airfoil obtained from references [16:110] and [5:688], are not C^1 smooth which caused problems with solution convergence and inaccuracy, and forced unwanted spikes and noise into the computed data. Thus, smoothing of the airfoil coordinates was necessary.

Figure 4 shows that smoothing has considerably improved the C^1 variation along the surface (though it could

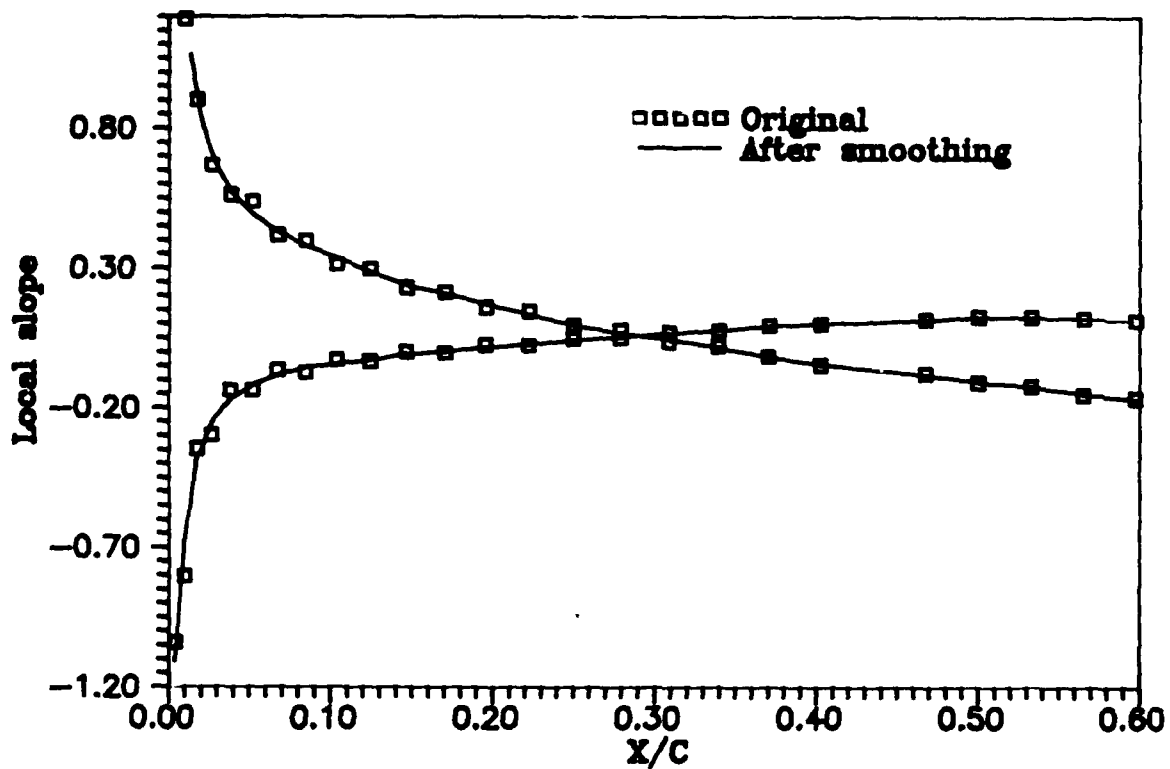


Figure 4 Comparison of local slope, before and after smoothing

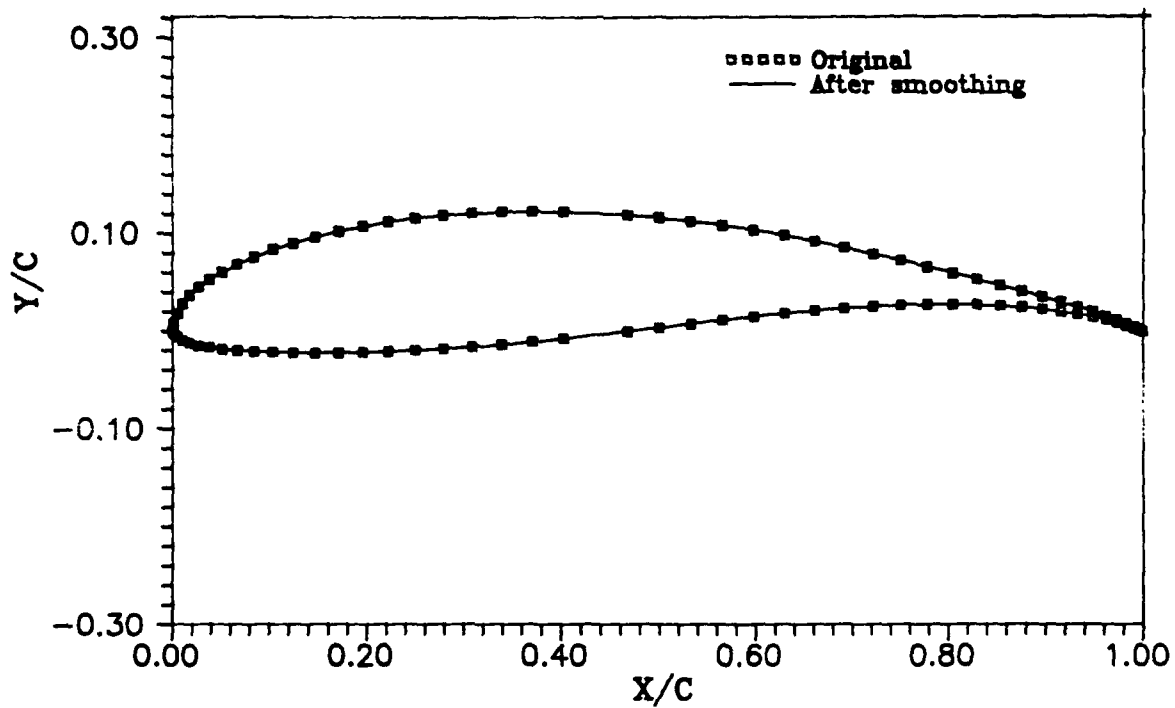


Figure 5 Wortman FX63-137 airfoil, before and after smoothing

have been better), without significantly changing the geometry of the airfoil, Figure 5, Appendix D tabulates the coordinates before and after smoothing..

Wake Profile. The problem of approximating the wake profile or the branch cut for the C-grid has been solved by piecing together three polynomials. The first segment is a sixth-order polynomial, which approximates the start of the profile based on mean trailing edge deflection and location. The first patch terminates $0.6c$ downstream of the trailing edge, where the final wake angle is enforced. The wake angle can be either a user input or the angle of attack (default).

Figure 6 shows a sketch of the wake profile. Coefficients a_0 through a_6 of the polynomial approximating this curve are found by applying the following conditions.

- (a) $x = 0 \quad y = 0$
- (b) $x = 0 \quad \frac{\partial y}{\partial x} = \delta_{te}$ (mean trailing edge slope)
- (c) $x = 0 \quad \frac{\partial^2 y}{\partial x^2} = 0$
- (d) $x = x_1 \quad \frac{\partial y}{\partial x} = \alpha$ (angle of attack)
- (e) $x = x_1 \quad \frac{\partial^2 y}{\partial x^2} = 0$
- (d) $x = x_2 \quad \frac{\partial y}{\partial x} = \alpha$
- (e) $x = x_2 \quad \frac{\partial^2 y}{\partial x^2} = 0$

$$y = a_0 x^6 + a_1 x^5 + a_2 x^4 + a_3 x^3 + a_4 x^2 + a_5 x + a_6$$

The second patch is nearly the same as the sixth order polynomial described above. The only differences being in the values of x_1 and x_2 , which are so chosen as to be optimum for this patch, and would allow y variation without

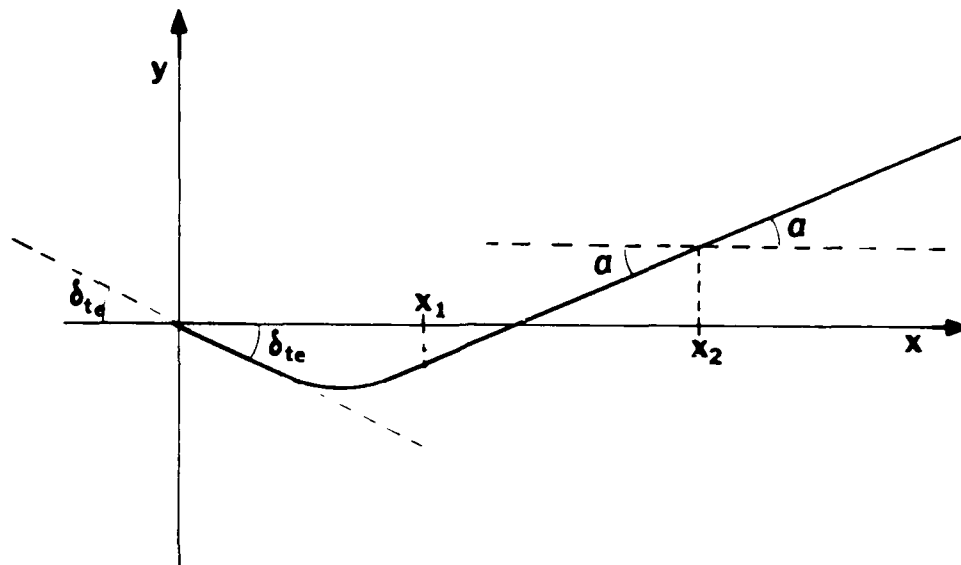


Figure 6 Wake Profile

oscillations (characteristic of higher-order polynomials).

This patch picks the slope error at the end of first patch and blends it down to zero. Thus by the end of this patch, the profile has acquired the required slope.

The third and final patch linearly extrapolates the co-ordinates till the end of the branch cut based on the slope information provided to it by the second patch.

The overall problem of grid generation (c) poses the most stringent requirement, and, in the opinion of the author, is best solved by an elliptic grid generation scheme, such a scheme has the inherent property of generating very smooth grids and provides complete control over grid point

distribution. A core program was thus acquired from Lt. Amdhal (AFWAL) [1], that solves equations (7) to generate a grid (based on the boundary point spacing).

$$\begin{aligned}\alpha x_{\xi\xi} - 2\beta x_{\xi\eta} + \gamma x_{\eta\eta} &= -J^2(Px_{\xi} + Qx_{\eta}) \\ \alpha y_{\xi\xi} - 2\beta y_{\xi\eta} + \gamma y_{\eta\eta} &= -J^2(Py_{\xi} + Qy_{\eta})\end{aligned}\quad (7)$$

where α , β , γ , J are defined in Appendix B, and P and Q are terms used to control point spacing in the interior of the domain.

Because the core program required boundary definition data to generate grids, a program named "BOUNDARY" was developed. This program is interactive and allows the user complete control over point distribution and spacing on all four boundaries of the C-grid see Figure 7.

This program borrows some stretching and curve fitting routines from a hyperbolic-grid generator developed by Kinsey and Barth, AFWAL [13], and employs the Vinokur stretching function [26] for point distribution and spacing variation. The hyperbolic-grid generator is based upon the algorithm developed by Steger and Chaussee [22].

The elliptic-grid generator thus creates grids based on boundary point and spacing output of the program Boundary. An example of a grid so generated, is given as Figure 8.

In practice however, it was found that elliptic grid generation does indeed provide complete control over all aspects of the grid, but has the serious short-coming of being computationally expensive. Also, convergence is not

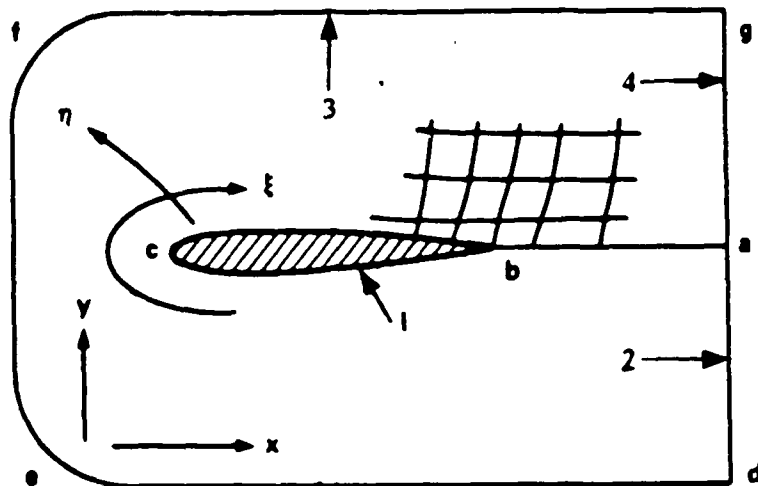


Figure 7 Boundaries of C type grid

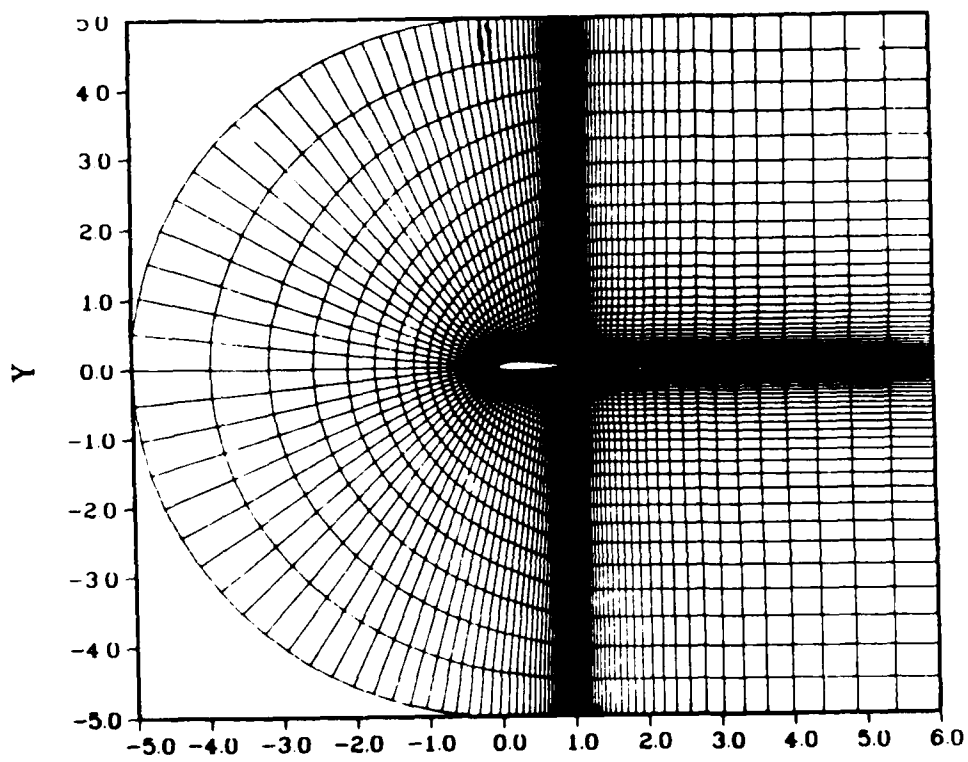


Figure 8 C-grid created by the Elliptic grid generator

always ensured and if it does occur it can take a very long time to converge to an acceptable tolerance. Therefore, the grids used in this study were generated using a modified version of the hyperbolic grid generator, described earlier in this section. The modifications were primarily restricted to generation of the wake profile.

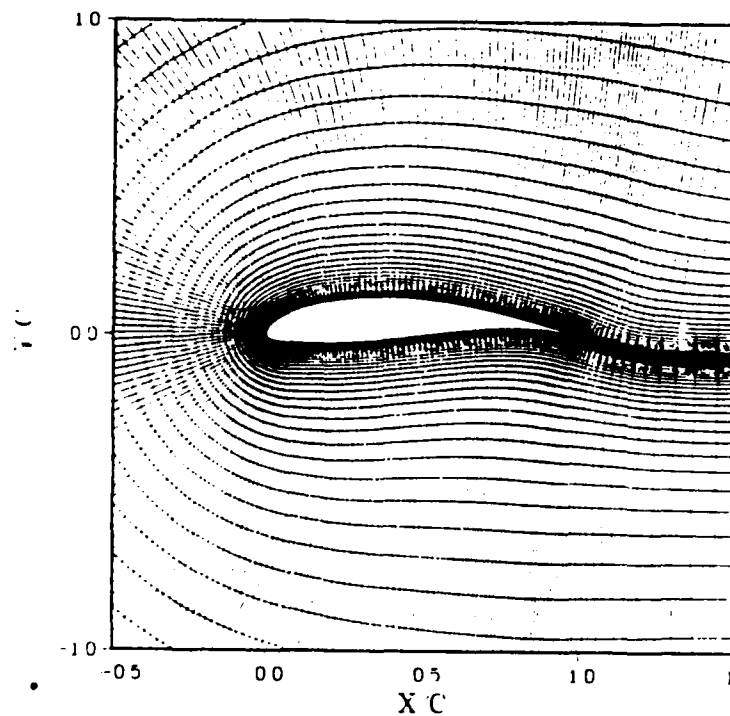


Figure 9 C-grid generated using Hyperbolic grid generator

The advantages of this grid-generation system are that it is unconditionally stable and produces smooth and nearly orthogonal grids. Furthermore it is very inexpensive to use and generates grids interactively in a very short time. The disadvantage is that very little control is available on

spacing and distributions of grid lines in the marching direction (normal to the inner boundary). The theory and program details of the hyperbolic-grid generation system are discussed at length in Ref. [13]. Figure 9 is an example of a grid generated hyperbolically.

Numerical method

The vorticity-transport equation, (6a) consists of an unsteady term ω_t , the advective terms $\psi_\xi \omega_\eta$ and $\psi_\eta \omega_\xi$, and the viscous diffusion term $(\mu\omega)_{\eta\eta}$. This equation is nonlinear in the advective terms, and must be linearized before any numerical algorithm can be applied to it. Furthermore, the equation is parabolic in time and in the streamwise direction (ξ), but due to the nonlinearity must be solved iteratively. On the other hand, the the stream function equation is linear and elliptic and may be solved using either direct methods or iterative techniques.

Basically there are two approaches to solve the vorticity-stream function equations, one is the time dependent approach (unsteady problem) and the other is the steady-flow approach (steady state problem) (18:107). In this study, both of these approaches have been incorporated into the code so that the user may benefit from the advantages of either scheme. A comparison of the two approaches follows.

Time-dependent approach. The Poisson equation for

stream function is iterated to convergence at each time step of the vorticity-transport equation. The solution is marched in time, therefore is time accurate. This approach is more stable numerically than the steady state approach, but is computationally intensive.

Steady-state approach. In this approach, the stream function equation is not iterated to convergence at each time step. Instead both equations are iterated simultaneously, and, if convergence takes place, steady state can be reached more quickly than with the time-dependent approach. However, because the stream function equation is not converged at each vorticity iteration, a poor initial condition can lead to non-linear instability (18:107-108).

The pseudo-linearized vorticity equation is given below along with the stream function equation. These equations are expressed for a general curvilinear coordinate system and are in delta (δ) form (see Appendix C for derivations).

$$\begin{aligned} J \frac{\delta \omega}{\Delta t} + \omega_{\xi} \delta \psi_{\eta} + \psi_{\eta} \delta \omega_{\xi} - \omega_{\eta} \delta \psi_{\xi} - \psi_{\xi} \delta \omega_{\eta} - \frac{1}{Re} \left(\frac{\gamma}{J} (\mu \delta \omega)_{\eta} \right)_{\eta} \\ = - \omega_{\xi} \psi_{\eta} + \psi_{\eta} \omega_{\xi} + \frac{1}{Re} \left(\frac{\gamma}{J} (\mu \omega)_{\eta} \right)_{\eta} \quad (8a) \end{aligned}$$

$$\begin{aligned} \left(\frac{\alpha}{J} \delta \psi_{\xi} - \frac{\beta}{J} \delta \psi_{\eta} \right)_{\xi} + \left(\frac{\gamma}{J} \delta \psi_{\eta} - \frac{\beta}{J} \delta \psi_{\xi} \right)_{\eta} + J \delta \omega \\ = - \left(\frac{\alpha}{J} \psi_{\xi} - \frac{\beta}{J} \psi_{\eta} \right)_{\xi} - \left(\frac{\gamma}{J} \psi_{\eta} - \frac{\beta}{J} \psi_{\xi} \right)_{\eta} - J \omega \quad (8b) \end{aligned}$$

Discretization

In order to be able to handle arbitrary geometries, a second-order accurate (in space) conservative differencing scheme is generated for the stream function equation (8b) by integrating the equation around a differential element in the physical domain, see Figure (10).

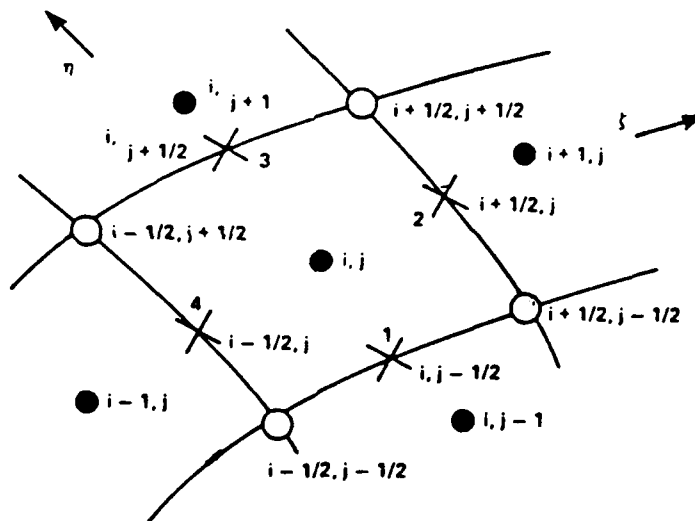


Figure 10 Differential element [11:3]

The resulting system of algebraic equations is solved iteratively using SLOR (Successive Line Over Relaxation). For each ξ -line (constant- i) in the computational domain, the finite-difference equations at each node can be written as; [11:3].

$$\begin{aligned}
& A_j^* \delta \psi_{i,j-1} + B_j^* \delta \psi_{i,j} + C_j^* \delta \psi_{i,j+1} \\
& + D_j^* \delta \omega_{i,j-1} + E_j^* \delta \omega_{i,j} + F_j^* \delta \omega_{i,j+1} = R_j^*
\end{aligned} \tag{9a}$$

$$\begin{aligned}
& A_j^o \delta \psi_{i,j-1} + B_j^o \delta \psi_{i,j} + C_j^o \delta \psi_{i,j+1} \\
& + D_j^o \delta \omega_{i,j-1} + E_j^o \delta \omega_{i,j} + F_j^o \delta \omega_{i,j+1} = R_j^o
\end{aligned} \tag{9b}$$

where superscript "*" denotes a coefficient of the stream function equation; "o" identifies coefficient of the vorticity equation; "j" indicates the location of the node in the η -direction, and " $\delta\psi$ " is the change between two successive iterations or time levels, given by

$$\psi^{n+1} = \psi^n + \delta\psi^n \tag{10}$$

Thus along each ξ -line a tridiagonal system of equations is generated from the stream function equation, which can be solved using the Thomas algorithm until convergence is reached at each step of the vorticity equation. Note that the coefficients D_j^* , E_j^* and F_j^* would be zero for the stream function equation in time-accurate mode).

For the vorticity equation, (8a), central-difference approximations are used for all terms except for the term $(\psi_\eta \delta \omega_\xi)$, which is treated as an upwind difference. In the limit of the steady state a second order accurate solution is obtained ref. [11].

Thus, at each node along an ξ -line, the correction equations from Newton linearization have the general form

given by (9). Equations (9) is a set of, a block (2x2) tridiagonal system of equations, and is solved using the modified Thomas algorithm (simultaneous solution of (9) in steady state mode).

Boundary conditions

Since the governing equations remains the same, what distinguishes one flow field from the other are the boundary conditions, the initial conditions and of course flow parameters, such as Reynolds Number (Re).

The specification of boundary conditions not only affects the numerical stability of a computational scheme, but also greatly affects the numerical accuracy of the finite-difference solution. The boundary conditions therefore take on added significance and must be based upon physical phenomenon.

In this study, boundary conditions are initially specified in the physical domain in primitive variables. These are then transformed into boundary conditions in terms of vorticity and stream function for the computational domain.

Airfoil Surface. On this surface, the no-slip boundary condition is enforced, i.e.,

$$v = 0 \quad \& \quad u = 0 \quad (11)$$

It can be seen that an arbitrary constant value of the stream function ψ satisfies these conditions. In this study,

the value is chosen to be zero. Thus, the boundary conditions on the airfoil surface are.

$$\psi = 0 \quad \psi_y = 0 \quad (12)$$

As for the vorticity, because of no-slip at the wall, vorticity is produced on this surface and it is the diffusion and subsequent advection process, that actually drives the flow field [18:140].

The vorticity at the wall is computed using the conditions

$$2\Delta\eta \left. \frac{\partial}{\partial \eta} (\psi^n + \delta\psi^n) \right|_{j=1} = -3\delta\psi_{i,1} + 4\delta\psi_{i,2} - \delta\psi_{i,3} = 0 \quad (12)$$

$$\psi = 0 \quad (13)$$

and the recurrence relations

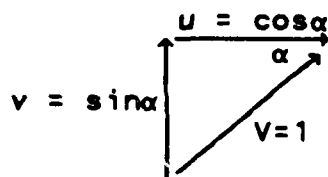
$$\delta\psi_j = R1_j \delta\psi_{j-1} + S1_j \delta\omega_{j-1} + T1_j \quad (14)$$

$$\delta\omega_j = R2_j \delta\psi_{j-1} + S2_j \delta\omega_{j-1} + T2_j \quad (15)$$

Algebraic manipulation of equations (12) to (15) results in the following relation for the change in vorticity on the airfoil surface.

$$\delta\omega_{i,1} = \frac{[R1_3 - 4]T1_2 + S1_3 T2_2 + T1_3 - 2\Delta\eta \psi_\eta}{[4 - R1_3]S1_2 - S1_3 S2_2} \quad (16)$$

Outer boundary. On this surface (Figure 7, surface no 3), the free-stream conditions due to velocity are enforced



$$u = \cos\alpha \quad \text{and} \quad v = \sin\alpha \quad (17)$$

where the non-dimensional free stream velocity has unity value and ' α ' is the angle of attack.

Applying the chain rule of partial differentiation results in the following condition.

$$\frac{\partial\psi}{\partial\eta} = \frac{\partial y}{\partial\eta} \cos\alpha - \frac{\partial x}{\partial\eta} \sin\alpha \quad (18)$$

This is the Neumann form of boundary condition, and the Dirichlet form can be obtained by integrating relation (18), which results in

$$\psi = y \cos\alpha - x \sin\alpha + \psi_0 \quad (19)$$

where ψ_0 is the arbitrary constant of integration and in this case has already been set to zero (airfoil surface $\psi = 0$, equation 13).

Outflow boundary. On this surface (Figure 7, surfaces 2 and 4), the free stream conditions given by equations (17) have also been enforced, which results in the following Neumann form.

$$\frac{\partial\psi}{\partial\xi} = \frac{\partial y}{\partial\xi} \cos\alpha - \frac{\partial x}{\partial\xi} \sin\alpha \quad (20)$$

The corresponding Dirichlet condition is

$$\psi = y \cos\alpha - x \sin\alpha + \psi_0 \quad (21)$$

where $\psi_0 = 0$

In this study both the Neumann as well as the Dirichlet type of boundary conditions have been incorporated in the source code, either of which can be selected by the user,

for any surface (outer or outflow). Based on the author's experience with the code, it was been found that the Neumann condition works better on the outflow boundary, especially when nonsymmetric flow is being computed. On the outer boundary, the Dirichlet condition works very well and helps accelerate convergence, with greater stability than the Neumann condition. This was found to be especially true at high angles of attack, when application of the Neumann condition can lead to oscillations and divergent behavior.

It must also be emphasized that each problem poses a different requirement and it is not necessary that one type of boundary condition will work best under all conditions. Thus advantage of the codes flexibility can be taken and different boundary conditions tested, to determine the optimal set for the problem being considered.

Wake (branch cut). Implementation of a boundary condition on the branch cut poses a very special problem, especially for non-symmetric flows, as values of ψ and ω at the cut have to be computed. The situation is further complicated by the fact that at the branch cut (C-grid), a discontinuity of the curvilinear coordinates exist (reversal of directions). Continuity can be maintained, however, by conceptually remaining on the same overlapping sheet as the cut is crossed. All derivatives thus do exist at the cut, but careful attention in difference formulations is necessary to represent derivatives correctly across the cut [25:70].

The unknowns ψ and ω are computed on the branch cut by solving the following system of equations along ξ -direction ($j=1$).

$$A_i^s \delta \psi_{i-1} + B_i^s \delta \psi_i + C_i^s \delta \psi_{i+1} + D_i^s \delta \omega_{i-1} + E_i^s \delta \omega_i + F_i^s \delta \omega_{i+1} = R_i^s \quad (21)$$

$$A_i^o \delta \psi_{i-1} + B_i^o \delta \psi_i + C_i^o \delta \psi_{i+1} + D_i^o \delta \omega_{i-1} + E_i^o \delta \omega_i + F_i^o \delta \omega_{i+1} = R_i^o \quad (22)$$

where superscript 's' denotes a coefficient of the stream function equation and 'o' denotes a coefficient of the vorticity equation.

It should be noted here that the coefficients in equation (21) and (22) are not computed in the same manner as for rest of the domain. Instead a special finite-difference formulation is employed to enable handling of the branch cut discontinuity, as discussed in the paragraphs above. Also, the system of equations is collated by marching along the constant η -line ($j=1$) in the ξ -direction. This results in a block [2x2] tridiagonal system, that is solved by using the modified Thomas algorithm. Thus, evaluation of ψ and ω represents a two point boundary value or elliptic problem. That must be solved at each iteration level, based on the known boundary conditions at either end of the branch cut. That is, at the trailing edge, the boundary condition given by equation (11) is enforced and at the other end, the boundary condition given by either equations (20) or (21) is employed.

Initial conditions

For unsteady flow solutions the proper initial conditions are critical. However, for situations in which only the steady state solution is sought, the accuracy of initial conditions takes on a slightly lesser significance, as the (theoretically) steady state can be achieved without any regard to the initial conditions. But, due to the non-linearity of the problem, it is necessary that the initial conditions be not too far from the physics. Under certain conditions improper initial conditions may lead to solutions, which may not have any physical significance and resemblance to the actual solution.

In this study a second order velocity profile in terms of stream function is initialized in the viscous region above the airfoil surface. In the inviscid region, the stream function takes on a distribution based upon the free stream velocity. The vorticity is assumed zero every where in the viscous as well as the inviscid regions.

Turbulence modeling

The influence of turbulence is modeled by means of an eddy viscosity ϵ , leading to the total or effective viscosity

$$\mu_t = \mu + \rho \epsilon \quad (23)$$

where μ is the molecular viscosity.

The eddy viscosity is computed from the zero equation or algebraic model of Baldwin and Lomax [4:2]. The Baldwin and

Lomax model is patterned after the Cebeci and Smith model [10], which is difficult to use, because of the necessity of determining the displacement thickness. The Baldwin-Lomax model overcomes this short-coming and uses the distribution of vorticity to determine the length scale in the outer region of the shear layer. Vorticity is also used in the inner region, this is beneficial as vorticity is the natural output of the present algorithm. Interested readers are referred to [15:6] for an interesting discussion on shortcomings of Baldwin-Lomax model and how these can be overcome.

Details of the Baldwin-Lomax model are discussed at length in references [4:2] and [15:6], therefore these will not be repeated here.

The routine employed in the computation of eddy viscosity is basically developed by Visbal [27] and has been modified to suit the present study. Also a transition model has been added to account for eddy viscosity variation, along the streamwise direction in a gradual manner rather than the abrupt change proposed by Baldwin and Lomax [4:2].

Transition model

Flow transition from laminar to turbulent is a very complex phenomenon, for which very little understanding currently exists. The situation is compounded by the complex interaction of many factors, such as free stream turbulence,

surface roughness, pressure and thermal gradients, to name only a few. Hence prediction of transition relies very heavily on experimental data and empirical formulations. One such relation is due to Michel and is known as the Michel's correlation method [15:6].

$$R_{\theta} = 1.174 \left[1 + \frac{22,000}{R_x} \right] R_x^{0.46} \quad (24)$$

where subscripts θ and x identify the Reynolds Number based upon momentum thickness and surface distance respectively.

The relation above is known as the Michel's correlation formula, and is often used to predict location of transition. This empirical formula is sometimes coupled with the location of laminar separation and transition is assumed to occur at either the point of laminar separation or where ever(24) is satisfied, which ever comes first. It should be pointed out that Michel's method is not valid for flows with separation [15:8].

In this study, the transition location has been picked based on the criterion, presented below in the order of preference.

- (a) Experimental data, if available.
- (b) Extrapolation of related experimental data reported by Bastedo [5] and Williams [28] and correlation with location of laminar separation.
- (c) Location of laminar separation.

Having located the point of transition the process of transition from laminar to turbulent is simulated using the Cebeci-Smith model of transition [15:6,10], which is given by;

$$\gamma_{tr} = 1 - \exp \left[-G(x - x_{tr}) \int_{x_{tr}}^x \frac{dx}{U_*} \right] \quad (25)$$

where

$$G = \frac{Re^2 U_{*tr}^3}{1200} (Re U_{*tr} x_{tr})^{-1.34} \quad (26)$$

where subscript tr designates values at the beginning of transition and γ_{tr} is the transition factor.

Pressure and force computation

The advantage of working with Vorticity " ω ", Stream Function " ψ " formulation is that the number of unknown variables reduces, as the pressure term is eliminated from the primitive momentum equation (see Appendix A for details). Once ω and ψ have been computed, the pressure solution can be extracted from these known variables by integrating the following Poisson equation for Pressure (for derivations, see Appendix F).

Equation (27) is the Poisson equation for pressure and is in general curvilinear coordinates. The only unknown variable is the pressure " P " and the right hand of this

$$\begin{aligned}
& \left(\frac{\alpha}{J} P_{\xi} - \frac{\beta}{J} P_{\eta} \right)_{\xi} + \left(\frac{\gamma}{J} P_{\eta} - \frac{\beta}{J} P_{\xi} \right)_{\eta} = 2(u_{\xi} v_{\eta} - u_{\eta} v_{\xi}) \\
& + (x_{\xi} \mu_{\eta} - x_{\eta} \mu_{\xi}) \left\{ \left(\frac{\alpha}{J} v_{\xi} - \frac{\beta}{J} v_{\eta} \right)_{\xi} + \left(\frac{\gamma}{J} v_{\eta} - \frac{\beta}{J} v_{\xi} \right)_{\eta} \right\} \\
& + (y_{\eta} \mu_{\xi} - y_{\xi} \mu_{\eta}) \left\{ \left(\frac{\alpha}{J} u_{\xi} - \frac{\beta}{J} u_{\eta} \right)_{\xi} + \left(\frac{\gamma}{J} u_{\eta} - \frac{\beta}{J} u_{\xi} \right)_{\eta} \right\} \\
& + (y_{\eta} u_{\xi} - y_{\xi} u_{\eta}) \left\{ \left(\frac{\alpha}{J} \mu_{\xi} - \frac{\beta}{J} \mu_{\eta} \right)_{\xi} + \left(\frac{\gamma}{J} \mu_{\eta} - \frac{\beta}{J} \mu_{\xi} \right)_{\eta} \right\} \\
& + \left(\omega + 2(x_{\xi} u_{\eta} - x_{\eta} u_{\xi}) \right) \left\{ \left[\frac{\gamma}{J} (x_{\xi} \mu_{\eta} - x_{\eta} \mu_{\xi}) \right]_{\xi} \right. \\
& \quad \left. - \left[\frac{\gamma}{J} (x_{\xi} \mu_{\eta} - x_{\eta} \mu_{\xi}) \right]_{\eta} \right\} \quad (27)
\end{aligned}$$

equation is known from the ω, ψ solution. This equation is discretized using central differences and the following equation is obtained at each node point.

$$a_j P_{j-1} + b_j P_j + c_j P_{j+1} = d_j \quad (28)$$

Solution along each constant " η " line is obtained implicitly using Thomas algorithm and is advanced from one level to the next using SLOR, till convergence to a required tolerance is achieved.

Boundary Conditions for Pressure. The boundary conditions used for the Poisson pressure equation (27) are mixed, as on the outer boundary, the Dirichlet boundary condition $P = 0$ is employed, the Neumann boundary condition $\partial P / \partial \eta = 0$ is enforced on the airfoil surface and $\partial P / \partial \xi = 0$ is enforced on the outflow boundary. On the

branch-cut ($j=1$), the pressure is approximated by averaging the value above and below this constant η line.

It would be appropriate to point out that at each node if $P_{i,j} + C$ is the solution obtained by integrating equation 3.27 (C is the constant of integration), then the level of $P_{i,j}$ can be chosen by specifying the value of P at any point in the domain. In this study, the value of P so chosen is zero and is specified at the outer boundary. This approach facilitates the computation of the coefficient of pressure C_p , which is simply given by $C_p = 2P$. Thus the variable P physically represents

$$P = \frac{P^* - P_\infty^*}{\rho_\infty^* U_\infty^{*2}}$$

where "*" represents dimensional variables and " ∞ " free stream properties.

Having found the pressure and skin friction distribution (see Appendix G) on the airfoil surface, the force and moment coefficients can be computed using the following relations, the details on usage and derivation are given in Appendix G.

$$\begin{aligned} C_L &= \sum_{i=1}^{N-1} \left\{ \Delta s_i \left(C_{f_i} \sin(\theta_i - \alpha) - C_{p_i} \cos(\theta_i - \alpha) \right) \right\} \\ C_d &= \sum_{i=1}^{N-1} \left\{ \Delta s_i \left(C_{f_i} \cos(\theta_i - \alpha) + C_{p_i} \sin(\theta_i - \alpha) \right) \right\} \\ C_{m_{c/4}} &= \sum_{i=1}^{N-1} \left\{ r_i \Delta s_i \left(C_{p_i} \cos(\theta_i + \theta_m) - C_{f_i} \sin(\theta_i - \theta_m) \right) \right\} \end{aligned} \quad (29)$$

where C_L is the lift coefficient, C_D is the drag coefficient and $C_{m_{c/4}}$ is the moment coefficient at the quarter chord.

The other variables are defined in Appendix G

Convergence Criterion

There are three types of converged solutions in numerical simulations, steady-state, periodic and unsteady. Even though no solution is perfectly steady, there is always some oscillation. The unsteady behavior may be so small as to be negligible. When this is the case the solution can be said to have reached a steady-state. The steady-state solution is the easiest to resolve, and is characterized by the uniform convergence of some criteria after an initial transition period [6].

The criterion for convergence for this study were the coefficients of lift (C_L) and drag (C_D). When the variations in C_D and C_L are less than 0.1% over 2000 iterations, then the solution is considered to have converged to a steady state.

IV Results and Discussion

In this chapter the Numerical results obtained from the ANS code are presented. The verification of the code and grids is presented first, which considers three cases, for testing and evaluating various aspects of the code. This is followed by the results for the Wortman Airfoil and comparison with experimental data.

Code Verification

Before the Wortman FX 63-137 airfoil can be effectively analyzed, it is necessary to ensure that the code and its segments are working correctly and are predicting the flow field accurately. This has been done by considering three cases under different flow conditions and comparing the results so obtained.

Case-1: Laminar Flow ($Re = 12,500$). The first case considered is the symmetric NACA-12 airfoil in laminar flow at Reynolds Number of 12,500.

The grid used to study this case was symmetric and had outer boundaries located 20 chord lengths from the airfoil surface. The grid had 200 symmetrically placed grid points on the airfoil's surface, spacing in ξ -direction at the leading edge was 0.001 and at the trailing edge 0.008. 40 points were distributed on the wake profile, and in the

η -direction 60 points with minimum wall spacing of 0.0001. The grid so obtained is shown in Figure 11.

NACA 0012

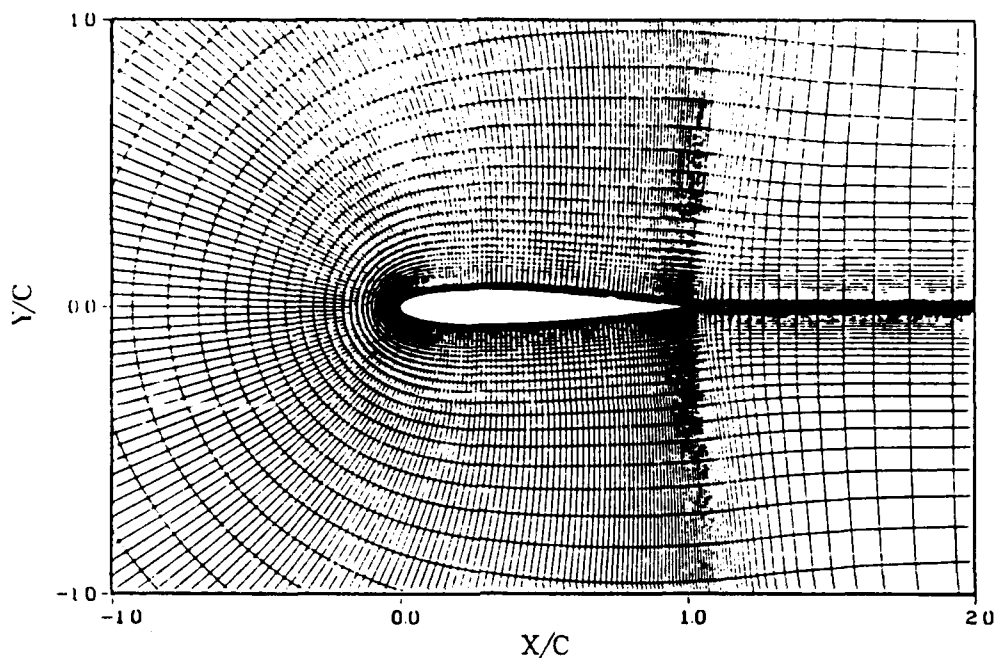


Figure 11 Grid for NACA-12 airfoil

The ANS code was executed for this case and convergence was achieved in only 9000 iterations, which took approximately 900 CPU seconds to execute on the Cray XMP. Figure 11 is a comparison of chord-wise skin friction distribution obtained using this code and the results obtained by Halim [11]. The streamline contours have been plotted in Figure 13a and these can be compared to contours from reference [11] in Figure 13b, it can be seen that agreement so far is very good. This is further

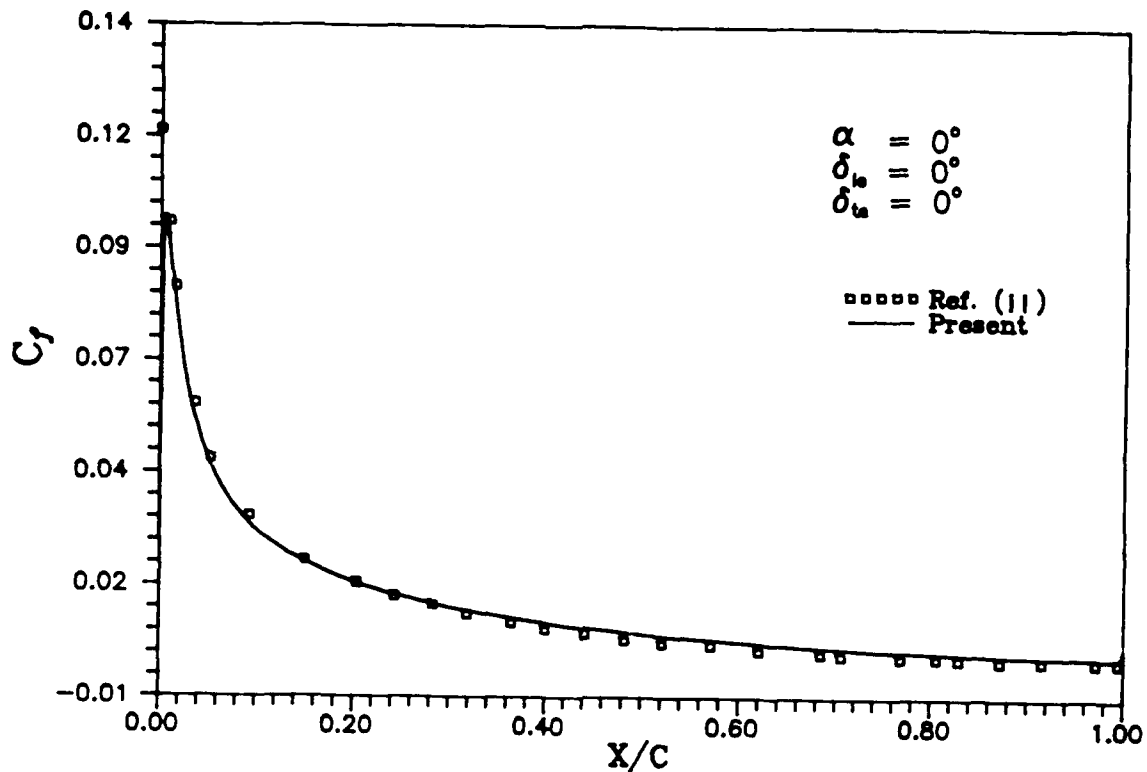


Figure 12 Comparison of skin friction coefficient distribution, present with Ref. [11].

substantiated by the fact that laminar separation was observed at $x/c = 0.818$, where the location reported by Halim [11] is $x/c = 0.8178$. Swanson and Turkel [23] solved the Navier-Stokes equations on a C-type grid for this airfoil and Reynolds number and the obtained laminar separation at $x/c = 0.817$. Based on the above given results, it can be concluded that the code does give excellent results for low Reynolds number laminar flow.

Case-2: Turbulent Flow ($Re = 6.5 \times 10^5$). This test case has been designed to check the accuracy of the turbulence and transition model, and the ability of the code to handle

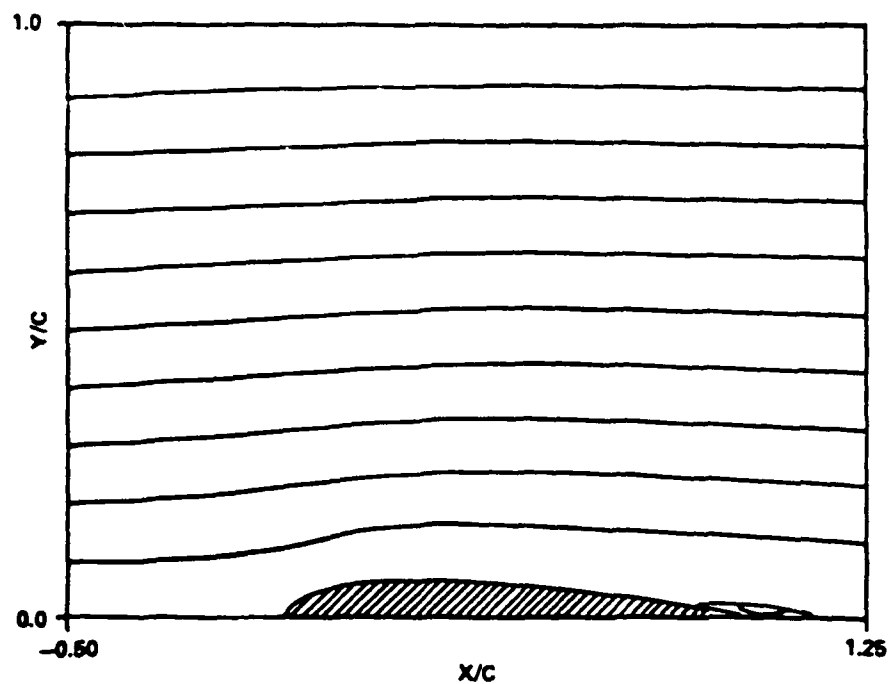
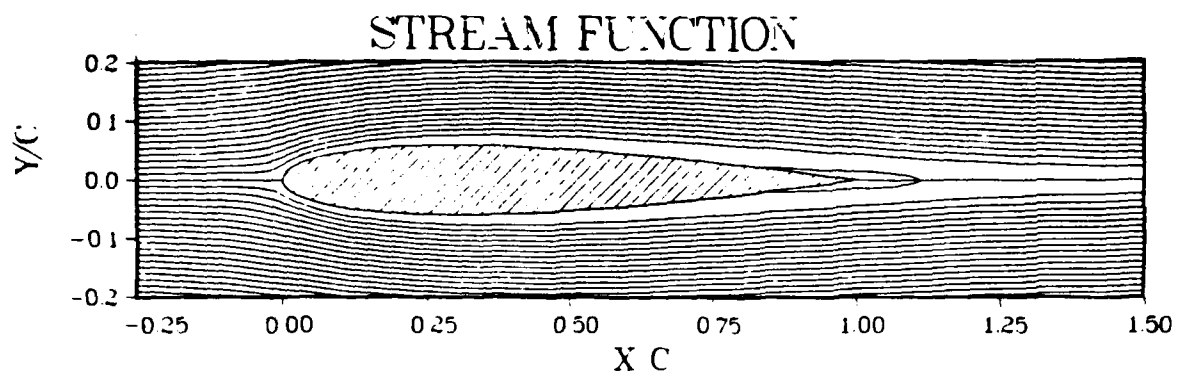


Figure 13 Comparison of constant stream function contours
NACA-12 airfoil, $Re = 12,500$

flows at high Reynolds Number.

The geometry considered is the flat plate at $Re=6.5 \times 10^5$, this value of Re has been chosen as turbulent flow under these conditions is ensured [20]. The flat plate has been chosen so that the geometry of the body does not complicate the analysis of the results.

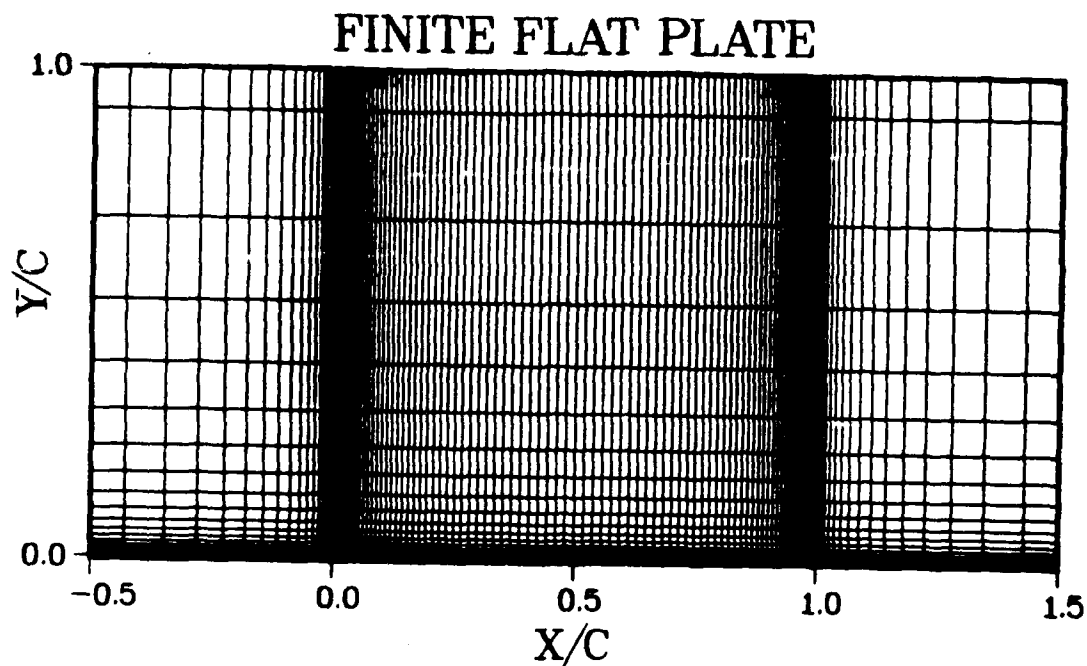


Figure 14 Grid used for Flat Plate

To allow flat plate computation, the code was slightly modified so that a H-type grid may be used (metrics singularity at the leading edge does not allow use of a C-type grid). The grid spacings used were the same as for

case-1, and Figure 14 is a portion of the grid finally used to compute flow.

To compare this test case with known and proven data, the boundary layer solver (developed by Cebeci & Smith) Ref. [9] was executed for Mach number of 0.001 and standard atmosphere free stream properties. This code solves the boundary layer equations on the infinite flat plate, advancing the solution parabolically in the streamwise direction, till the required Reynolds number is reached. In this case a constant step size $\Delta x = 0.02$ was used and transition to turbulent flow was triggered at $R_x = 3.2 \times 10^5$ [20].

The ANS code was also executed based on the above given transition criterion, the differences being the grid spacings and the Mach number, which was zero as the code is limited to incompressible flow only. The results so obtained are compared in Figures 15 through 17 and discussed below.

Figure 15 compares the skin friction distribution obtained from the two codes, and it can be seen that the results do compare favorably. Small deviation around $x/c = 0.6$ can be attributed to the differences in the transition location as it may not locate exactly at the same place due to non-presence of an appropriate node point.

Figure 16 compares the velocity profile close to the trailing edge ($x/c = 0.98$), with that obtained from ref. [9], the two profiles agree very nicely and the variations,

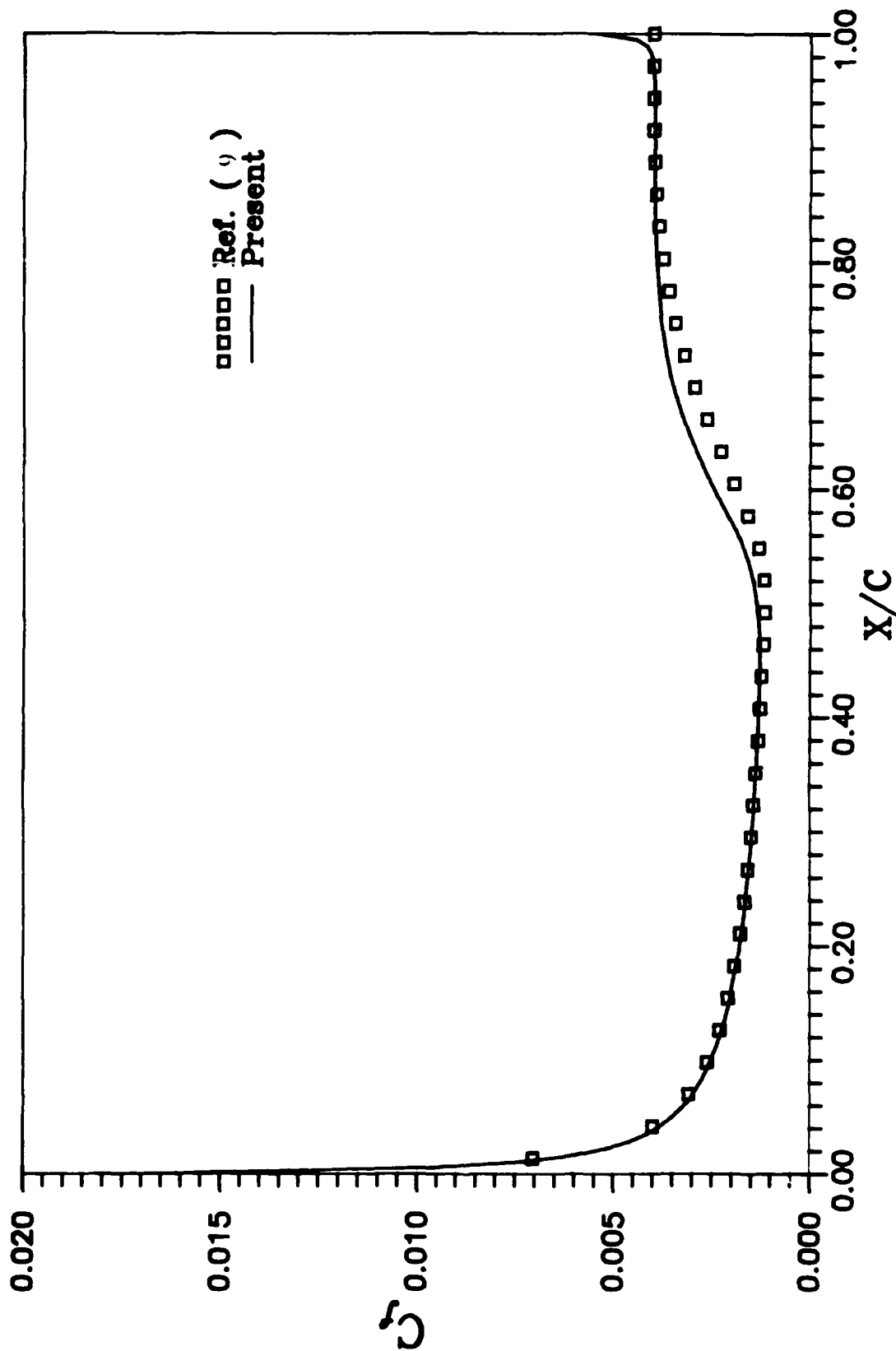


Figure 15 Comparison of skin friction coefficient vs. x/c
 Flat plate, $Re = 6.5 \times 10^5$

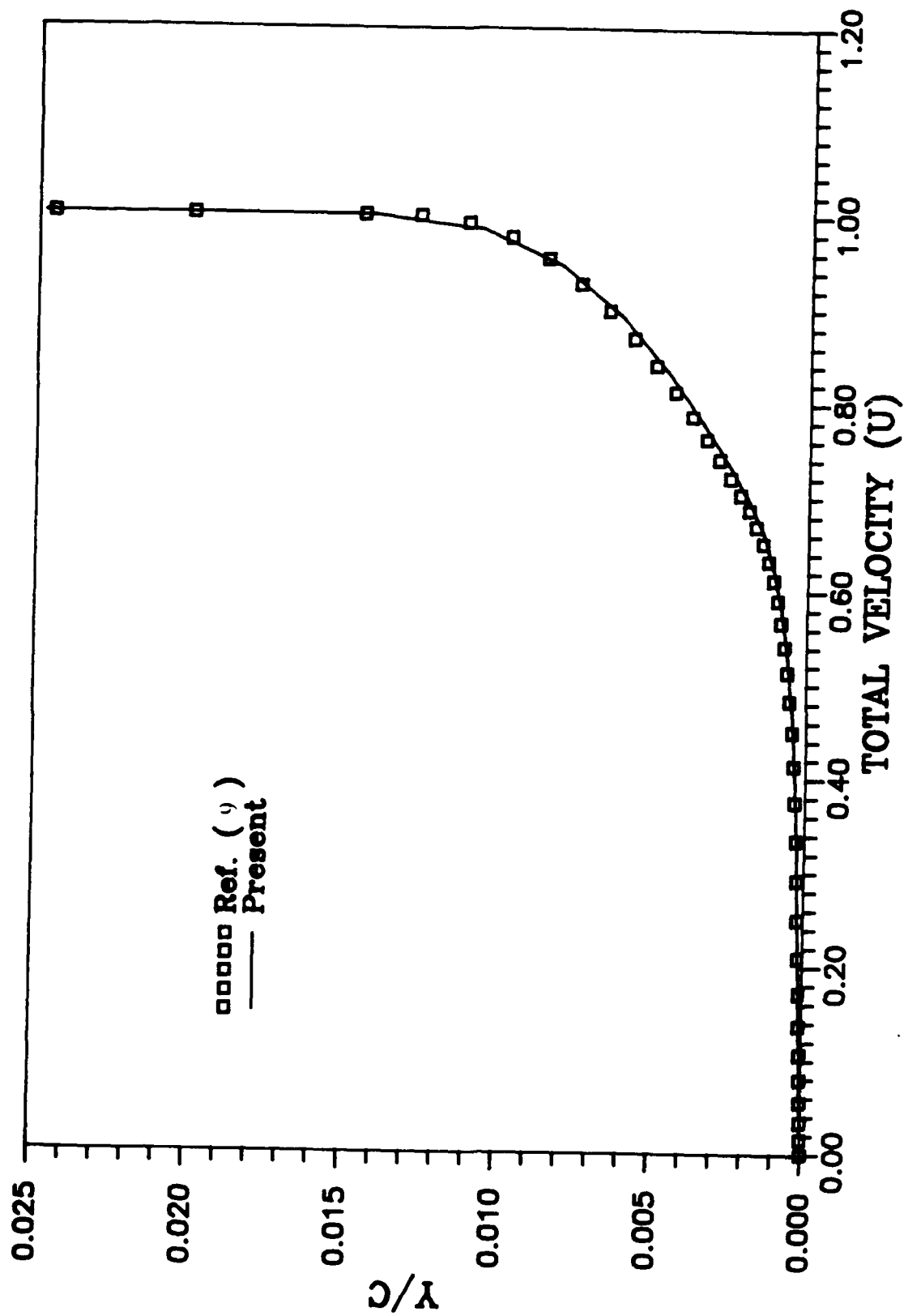


Figure 16 Comparison of velocity profile ($x/c = 0.98$)
Flat plate, $Re = 6.5 \times 10^5$

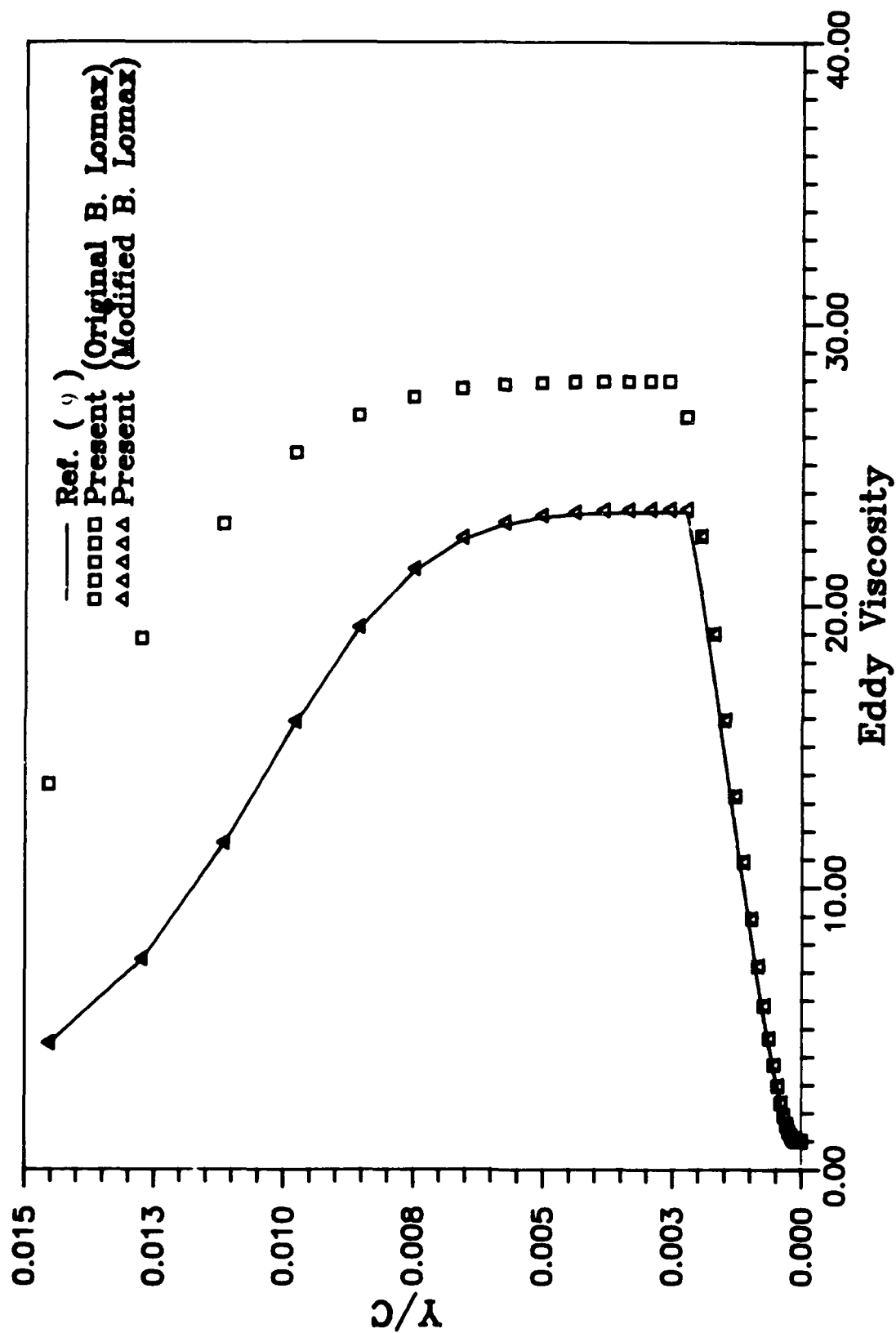


Figure 17 Comparison of eddy viscosity profiles,
Flat Plate, $Re = 6.5 \times 10^5$

though very small are within the tolerance ($\pm 5\%$).

The third and final plot for this case is Figure 17, this graph compares the Eddy Viscosity (ϵ) distribution obtained from the two codes. It can be seen that the Original Baldwin-Lomax model [4] predicts greater magnitude of ϵ in the outer region and also the distribution of the Klebanoff intermittency factor is slightly different, which causes the ϵ profile to be somewhat different from the one obtained using Cebeci-Smith model. Because the Baldwin-Lomax model is based on the Cebeci-Smith model therefore it is expected the later should predict the same ϵ distribution. On order to achieve this result the Baldwin Lomax model was modified with slightly different constants, given in Table 1. The constants C_{cp} is a scaling factor for the outer region and C_{kleb} is the scaling factor for computing the Klebanoff intermittency factor.

Figure 17 reveals that after modification the models do predict the same ϵ distribution. It should be noted that the constants used in this case are applicable to only this geometry and Reynolds number. A more general modification however, is proposed by Visbal and Knight [27] and York [29], the values of the constants for the outer model suggested by them are given in table 1.

The constants, used in this study, however, are the ones given by Baldwin-Lomax ref. [4], as use of any other values would have required a much more in-depth analysis, of

Table 1 Comparison of constants: modified and un-modified Baldwin-Lomax Model

Symbol	Original	Present(modified)	Ref.[27](modified)
C_{cp}	1.6	1.33	1.2
C_{kleb}	0.3	0.39	0.646

the models under different conditions, which is definitely not within the scope of this study.

Case-3: Non-Symmetric Turbulent Flow ($Re = 200,000$).

The third and final test case is the comparison of pressure distribution for Wortman FX 63-137 airfoil at an angle of attack of 1° and $Re = 200,000$.

The grid used used to study this case had grid spacing and point distribution exactly the same as for case-1, the grid however so obtained was non-symmetric due the characteristic high camber of Wortman airfoil.

Figure 18 compares present pressure distribution with data from Ref. [5]. Agreement between the two is very good and variations are within experimental tolerances.

Results

The results obtained for the Wortman FX 63-137 airfoil will now be presented, these were obtained using the ANS code developed in this study, wherein the original Baldwin-Lomax model has been used and the surface of the airfoil has been made mathematically smooth, using the program "Airfoil" (Appendix C).

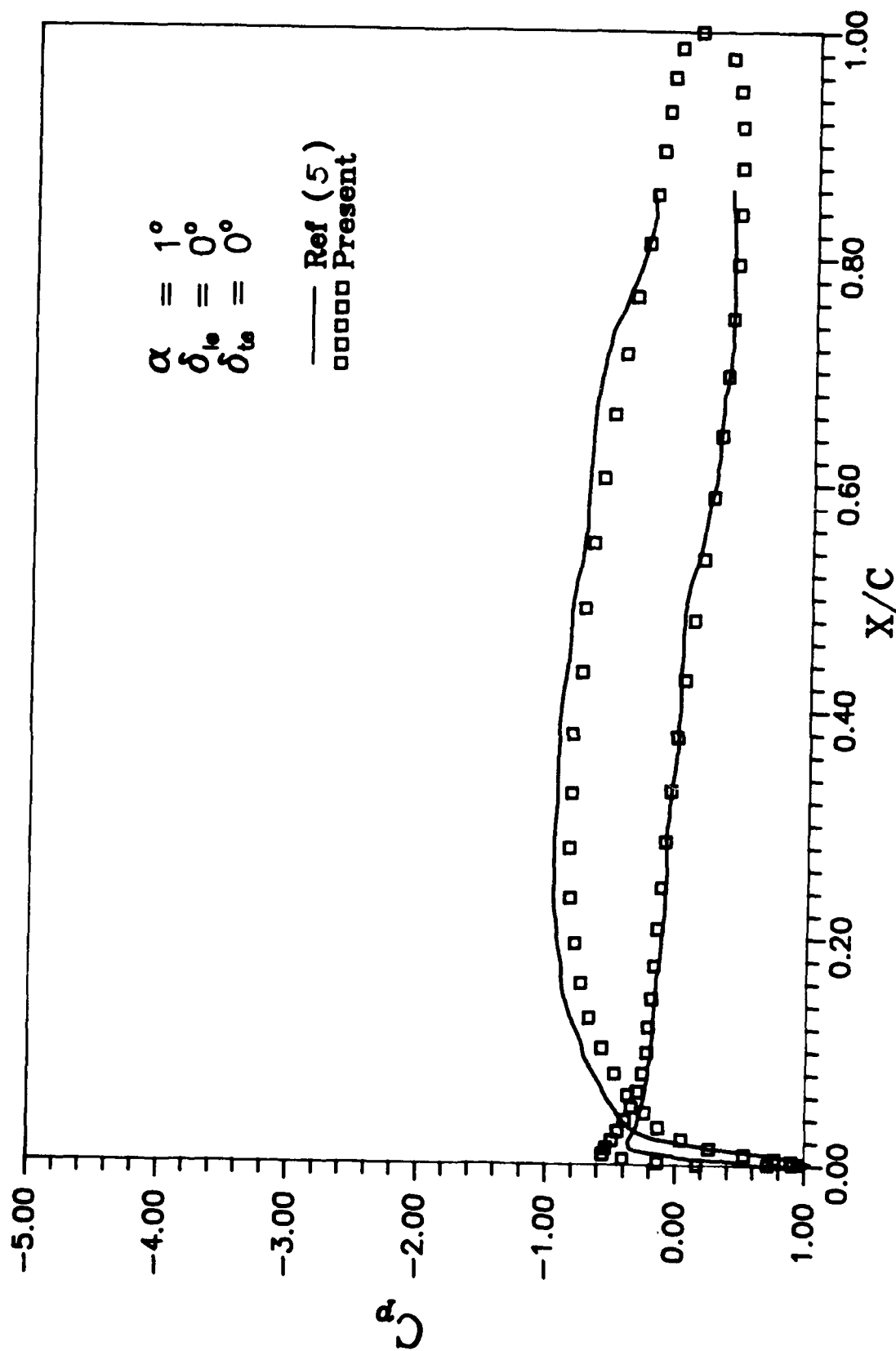


Figure 18 Comparison of pressure coefficient vs. x/c for Wortman airfoil, $Re = 2 \times 10^5$

The grids used to compute the different cases were all different from each other primarily in the wake region. As the wake profile (branch cut) had to honor the trailing edge deflection and the airfoil angle of attack, it is therefore not possible to show here each and every grid used in this study. However, Figure 19 is an example of a typical grid and Figure 20 shows the grid details of the leading as well as the trailing edge. The grid point distribution and spacings for all grids were exactly the same as defined for case-1 (NACA-12, $Re=12,500$).

Wortman airfoil, No deflections. Flow for this case was computed for 6 different angles of attack ie. $-4, 0, 4, 8, 12$ and 16 degrees. The constant stream function, velocity and vorticity contour plots for these cases are attached in Appendix H as Figures 36 through 51. The corresponding pressure coefficient and skin friction distribution are attached in Appendix I as Figures 52 through 67. The performance parameters; lift coefficient (C_L), Drag coefficient (C_D) and moment coefficient (C_m) are plotted against angle of attack in Figures 21, 22 and 23 respectively.

Wortman airfoil, $\delta_{l,e} = 5^\circ$, $\delta_{t,e} = 0^\circ$. Flow for this case was computed for 5 different angles of attack ie. $-4, 0, 4, 8$ and 12 degrees. The constant stream function, velocity and vorticity contour plots for these cases are attached in Appendix H as Figures 42 through 46. The corresponding

pressure coefficient and skin friction distribution are attached in Appendix I as Figures 58 through 61. The performance parameters; lift coefficient (C_L), Drag coefficient (C_D) and moment coefficient (C_m) are plotted against angle of attack in Figures 24, 25 and 26 respectively.

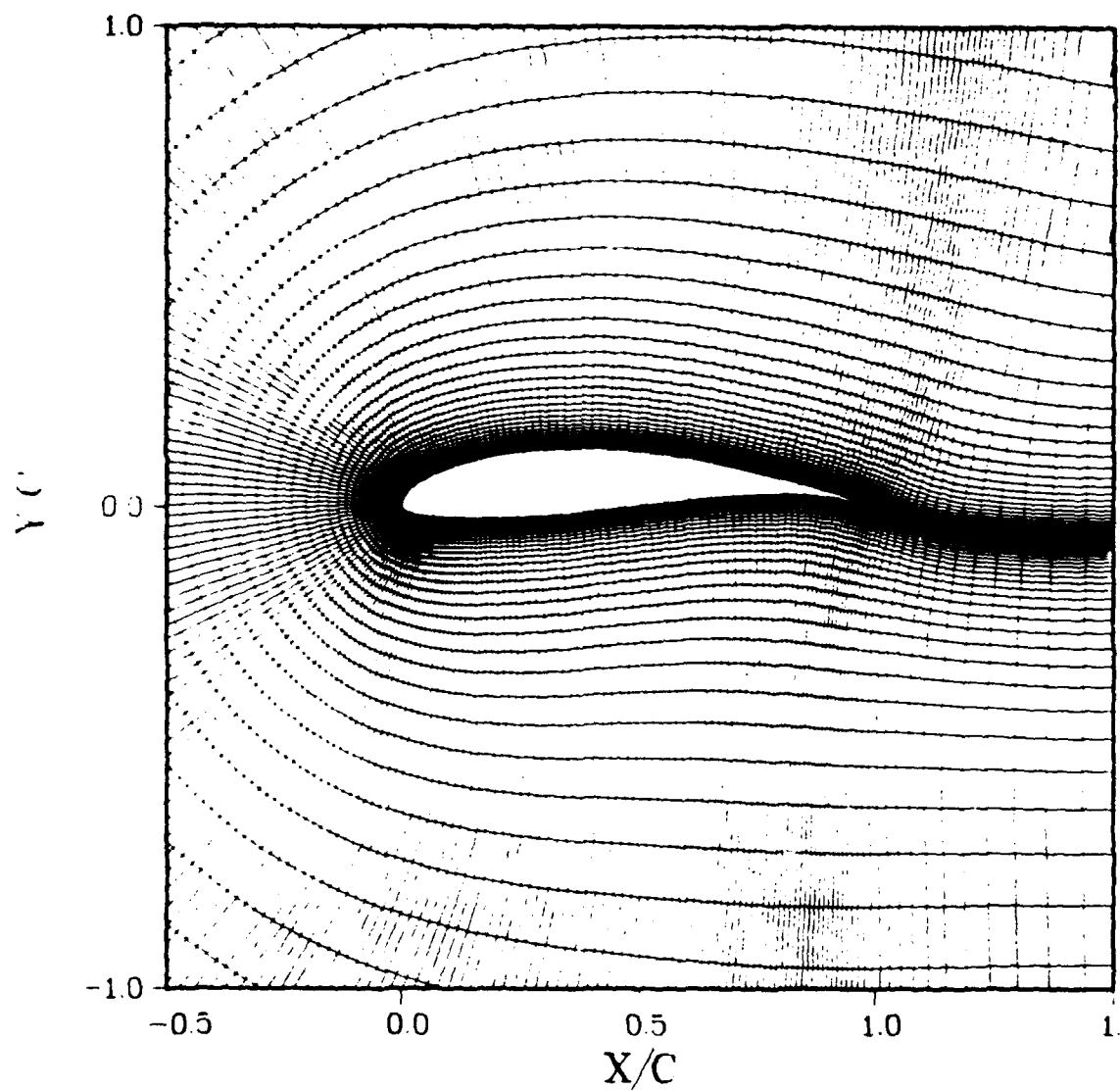


Figure 19 279x60 grid Wortman FX 63-137 airfoil

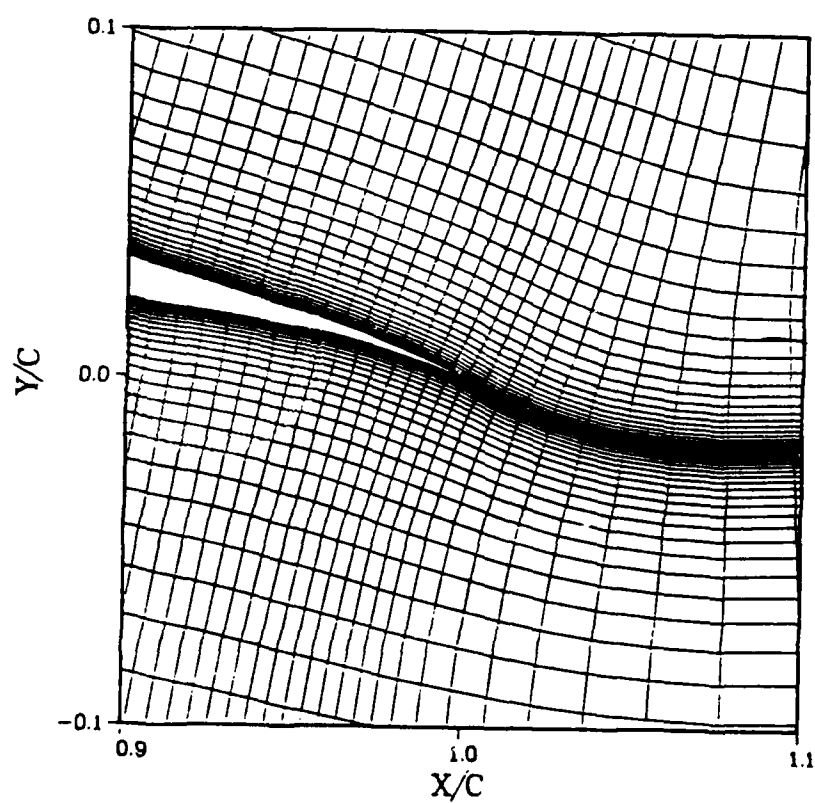
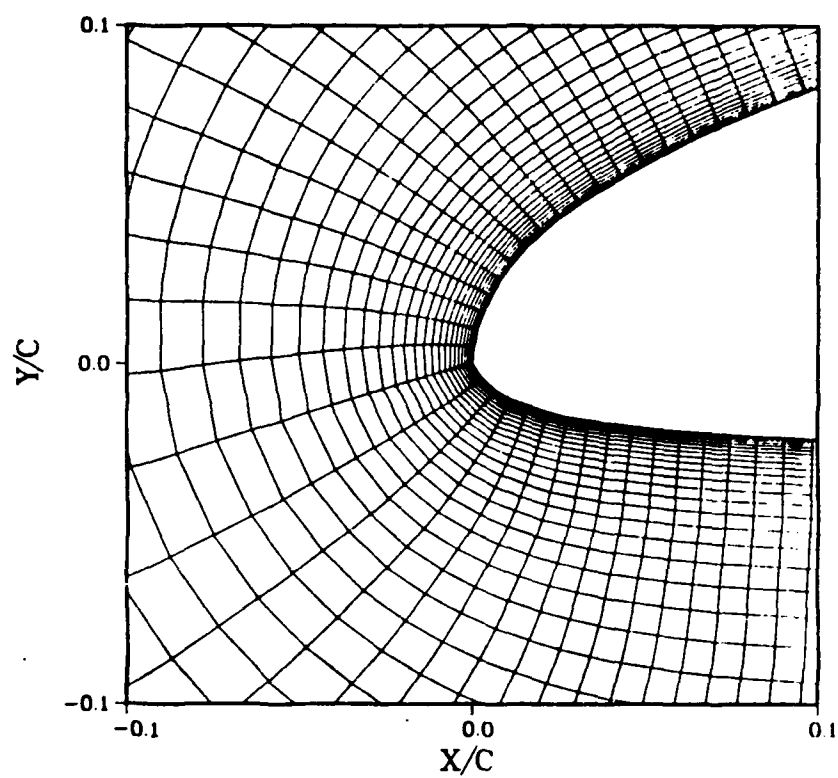


Figure 20 Grid detail Wortman FX 63-137 airfoil

Wortman airfoil, $\delta_{l,e} = 5^\circ$, $\delta_{t,e} = 20^\circ$. Flow for this case was computed for 5 different angles of attack ie. -4,0,4,8 and 12 degrees. The stream function, velocity and vorticity contour plots for these cases are attached in Appendix H as Figures 46 through 51. The corresponding pressure coefficient and skin friction distribution are attached in Appendix I as Figures 62 through 66. The performance parameters; lift coefficient (C_l), Drag coefficient (C_d) and moment coefficient (C_m) are plotted against angle of attack in Figures 27, 28 and 29 respectively.

Effect of Angle of Attack

On Lift Coefficient. The effect of angle of attack on the lift coefficient can be observed from Figures 21, 24 and 27. For all cases the lift curve (C_{l_α}) has a positive slope, implying a lift coefficient increase as the angle of attack is increased. It can be also observed that the lift curve slope remains essentially constant, however in Figure 21 the value of C_l obtained for $\alpha=16^\circ$ is less than the value predicted by the lift curve slope, this shows that the airfoil is approaching the stall condition and any further increase in α will trigger stall and would cause a significant drop in lift. The actual stall case could not be computed due to time limitation.

Comparison with experimental results is also made in Figures 21, 24 and 27, the present lift compare well with Perry [16] for $\alpha = -4, 0$ and 4 degrees. For greater angles

$\delta_{1e} = 0^\circ$
 $\delta_{1e} = 0^\circ$

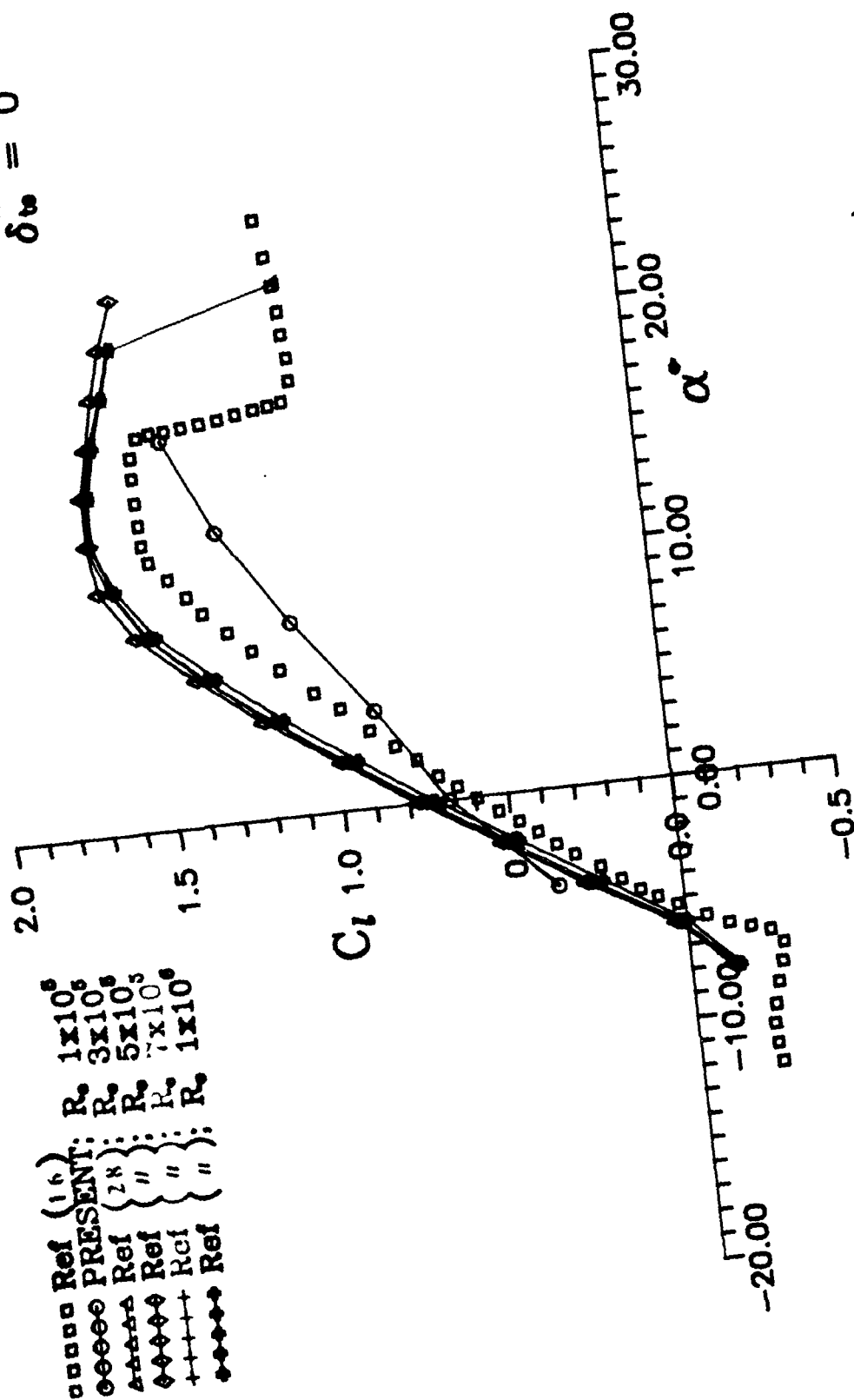


Figure 21 Comparison: Lift Coefficient vs. Angle of Attack
 Wortman Airfoil, $\delta_{1e} = 0^\circ$, $\delta_{1e} = 0^\circ$

$$\delta_{1e} = 0^\circ$$

$$\delta_{1e} = 0^\circ$$

□□□□ Ref (16) $R_e = 1 \times 10^6$
 ○○○○ PRESENT; $R_e = 1 \times 10^6$
 △△△△ Ref (28) $R_e = 3 \times 10^6$
 +++++ Ref " $R_e = 5 \times 10^6$
 ××××× Ref " $R_e = 7 \times 10^6$
 ♦♦♦♦♦ Ref " $R_e = 1 \times 10^7$

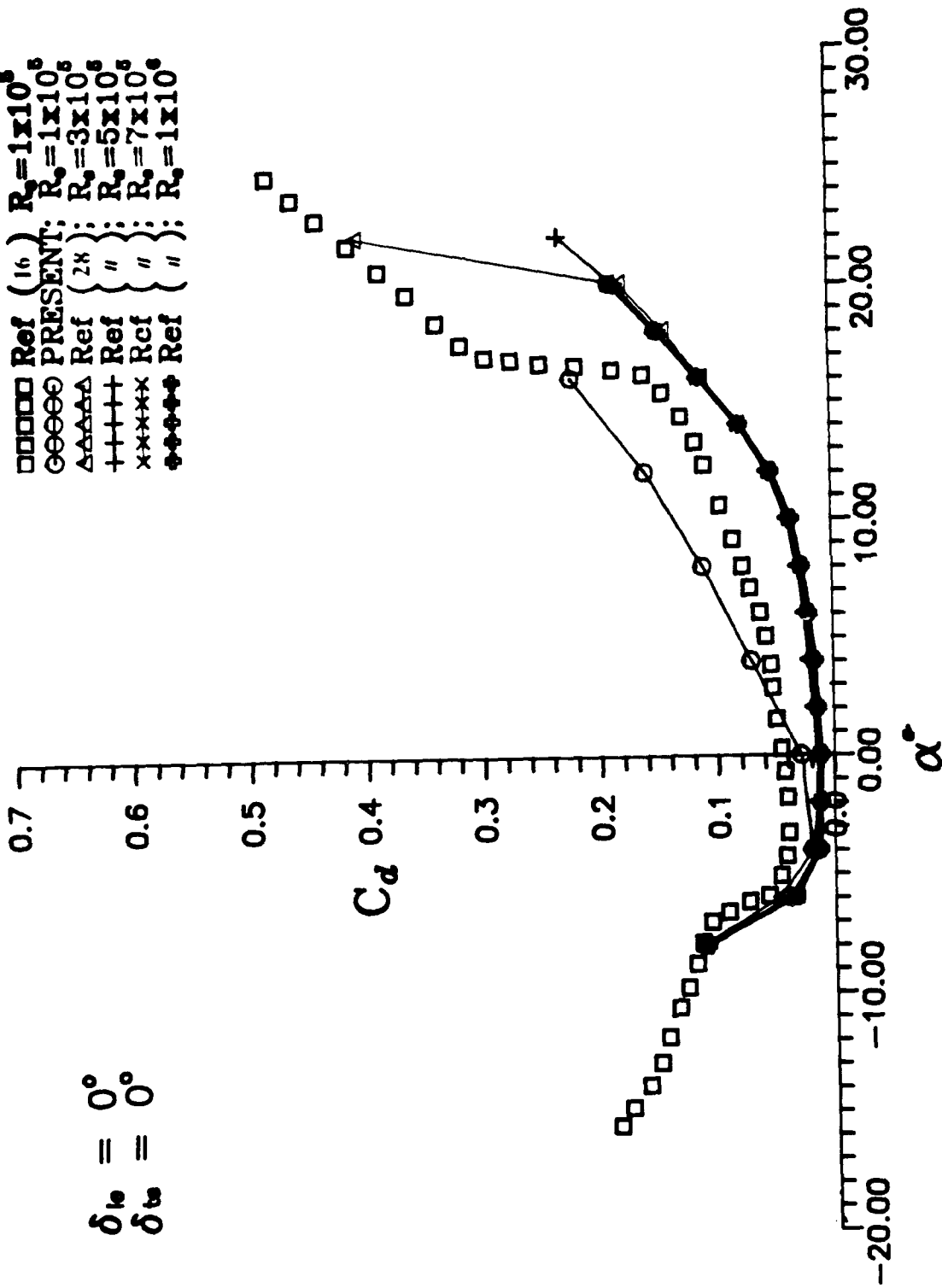


Figure 22 Comparison: Drag Coefficient vs. angle of Attack
Wortman Airfoil, $\delta_{1e} = 0^\circ$, $\delta_{1e} = 0^\circ$

□□□□ Ref (16)
 ○○○○ PRESENT; R_∞ 1x10⁶
 △△△△ Ref (28); R_∞ 3x10⁶
 ◇◇◇◇ Ref " ; R_∞ 5x10⁶
 +++++ Ref " ; R_∞ 7x10⁶
 ●●●● Ref " ; R_∞ 1x10⁶

$\delta_{t_0} = 0^\circ$
 $\delta_{i_0} = 0^\circ$

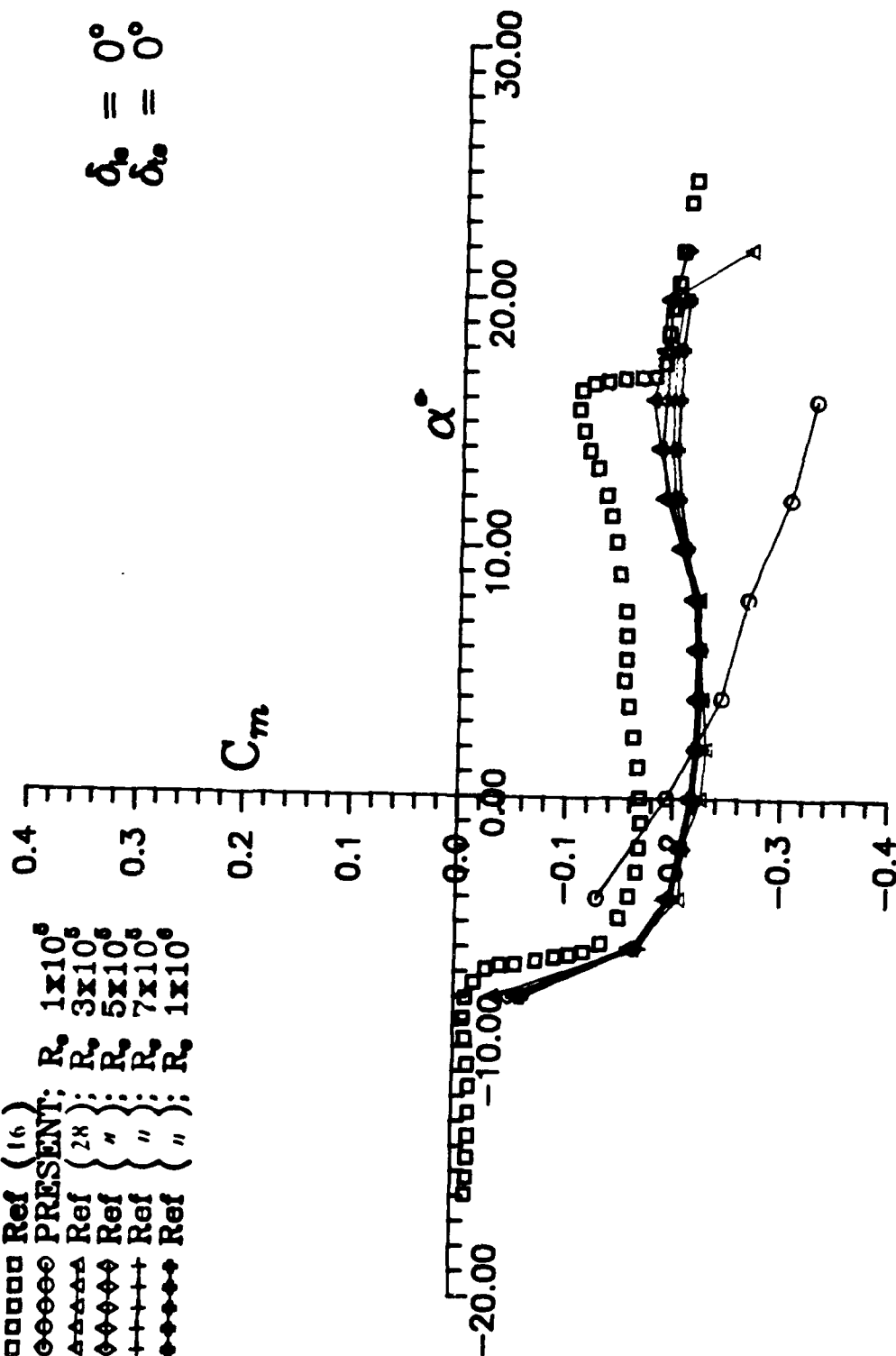


Figure 23 Comparison: Moment Coefficient vs. Angle of Attack Wortman Airfoil, $\delta_{t_0} = 0^\circ$, $\delta_{i_0} = 0^\circ$

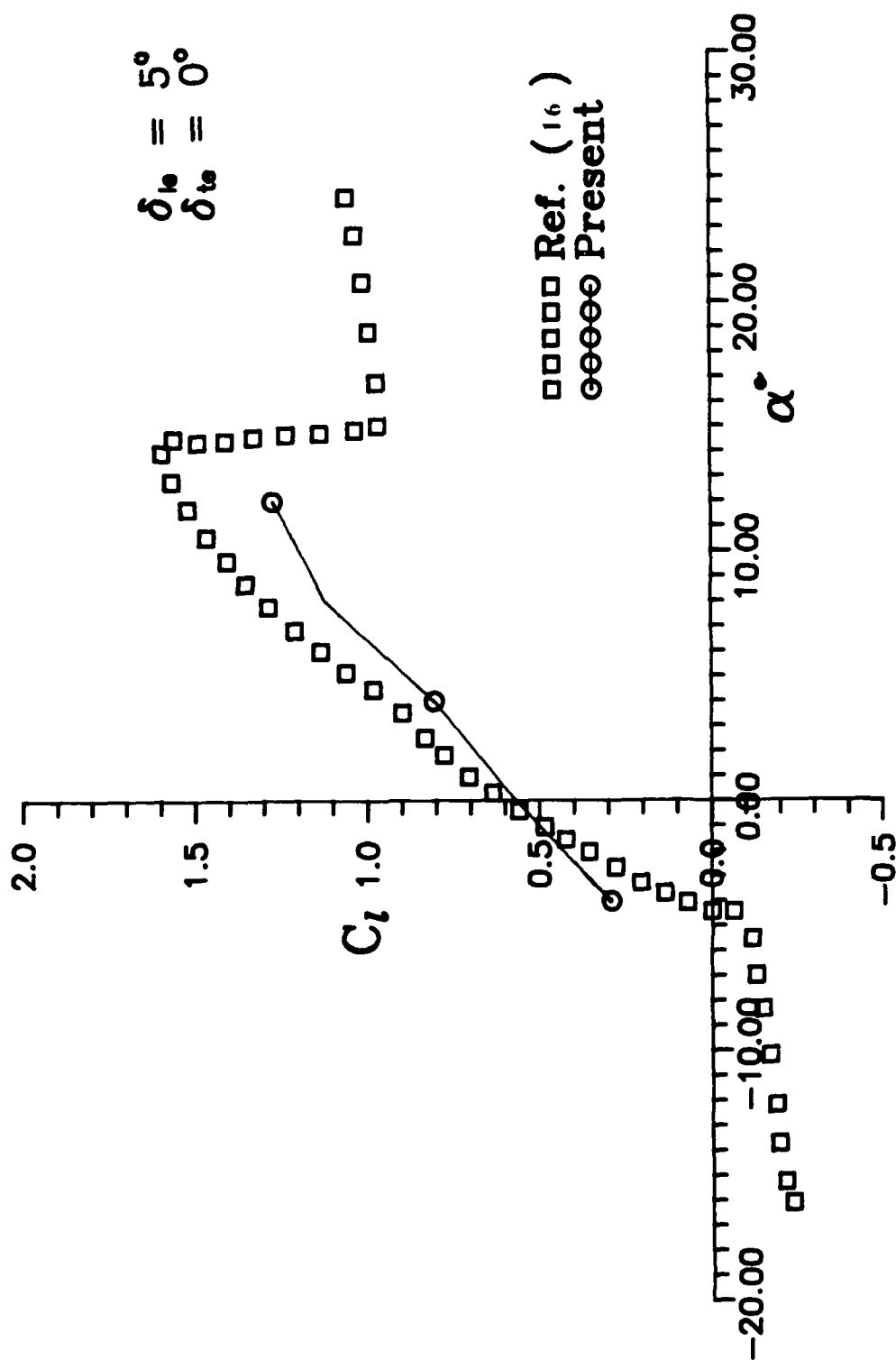


Figure 24 Comparison: Lift Coefficient vs. Angle of Attack
Wortman Airfoil, $\delta_{1e}=0^\circ$, $\delta_{1e}=5^\circ$

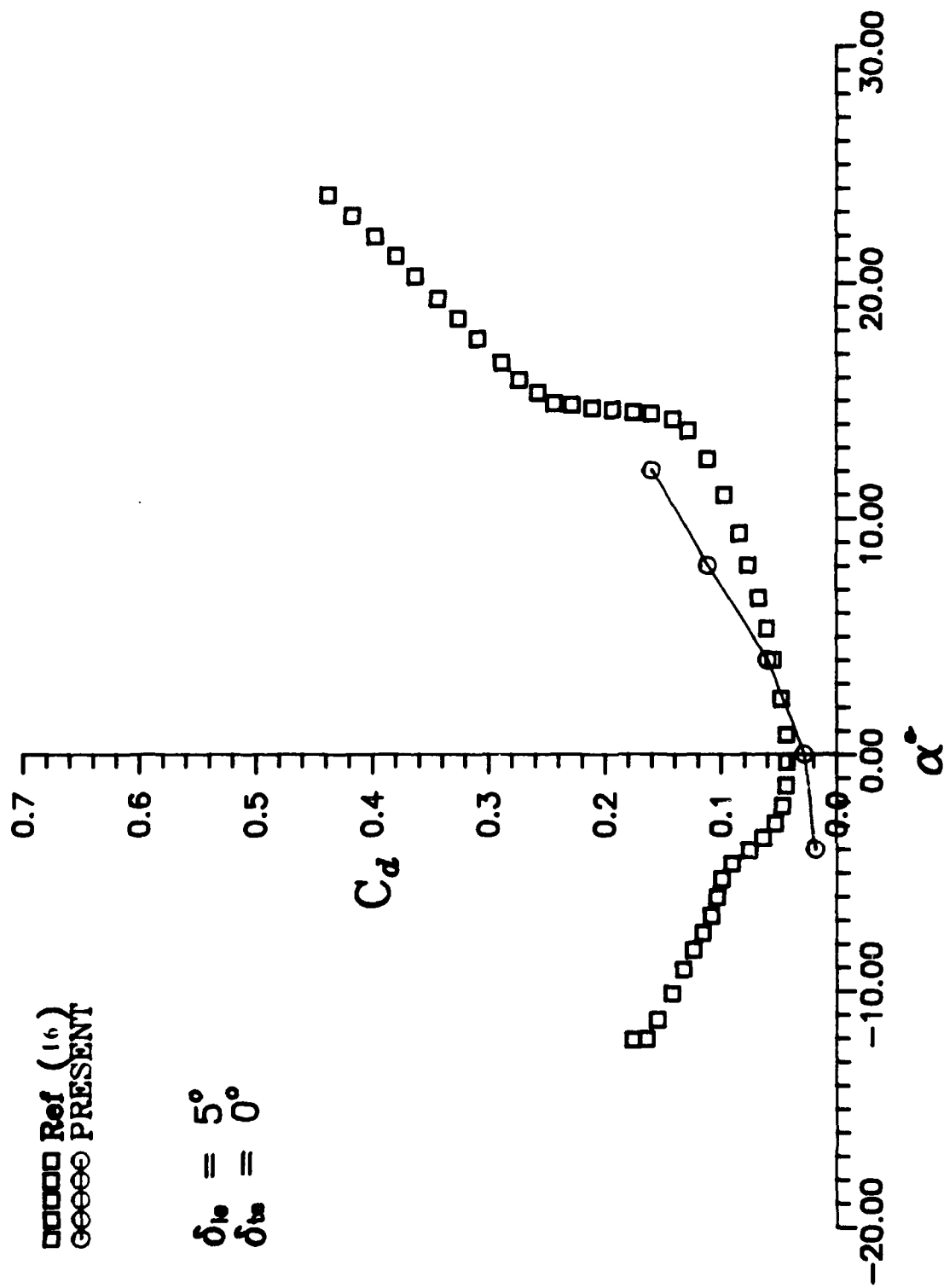


Figure 25 Comparison: Drag Coefficient vs. Angle of Attack
Wortman Airfoil, $\delta_{te} = 0^\circ$, $\delta_{1e} = 5^\circ$

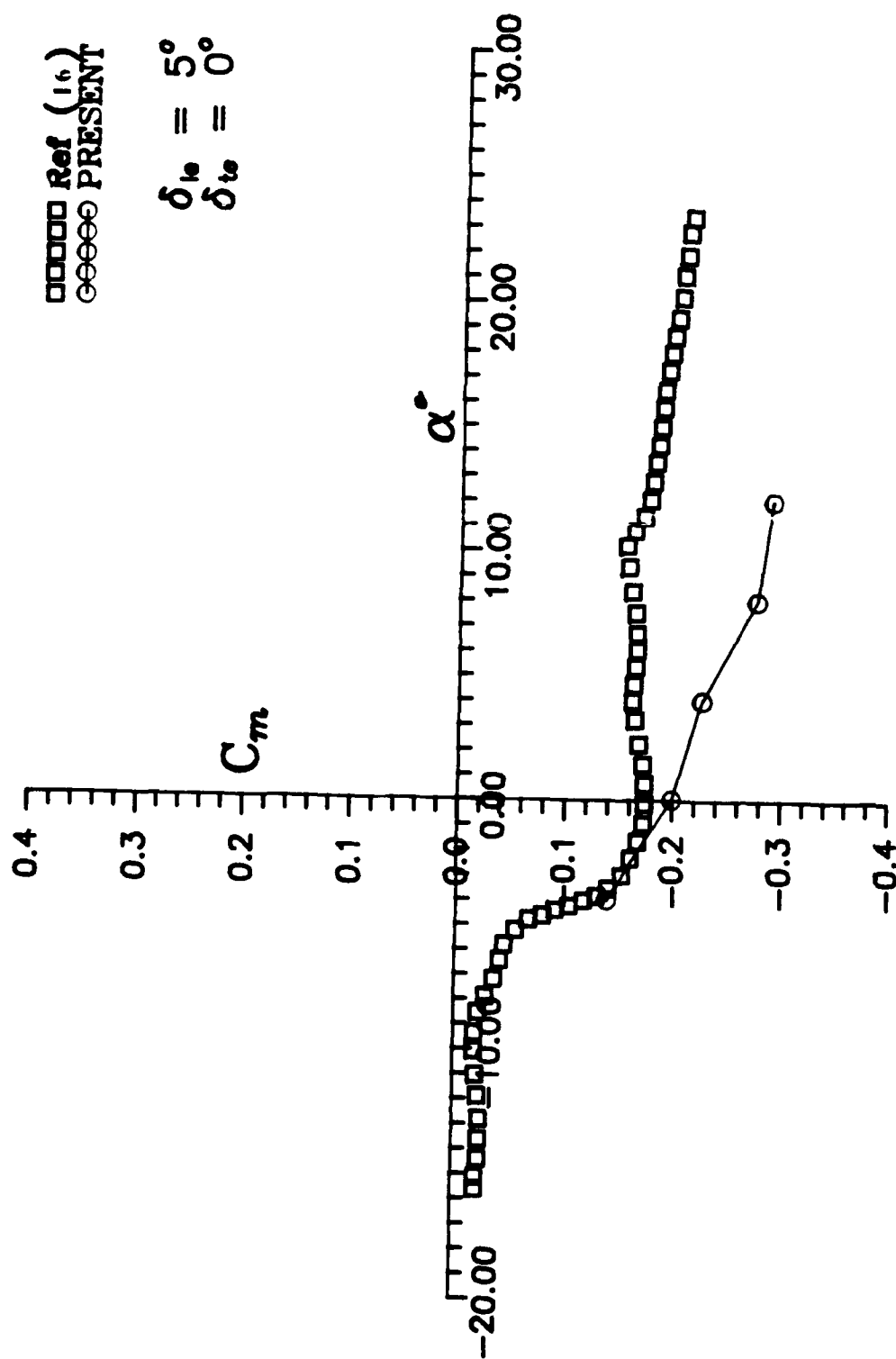


Figure 26 Comparison: Moment Coefficient vs. Angle of Attack
Wortman Airfoil, $\delta_{1e} = 0^\circ$, $\delta_{1e} = 5^\circ$

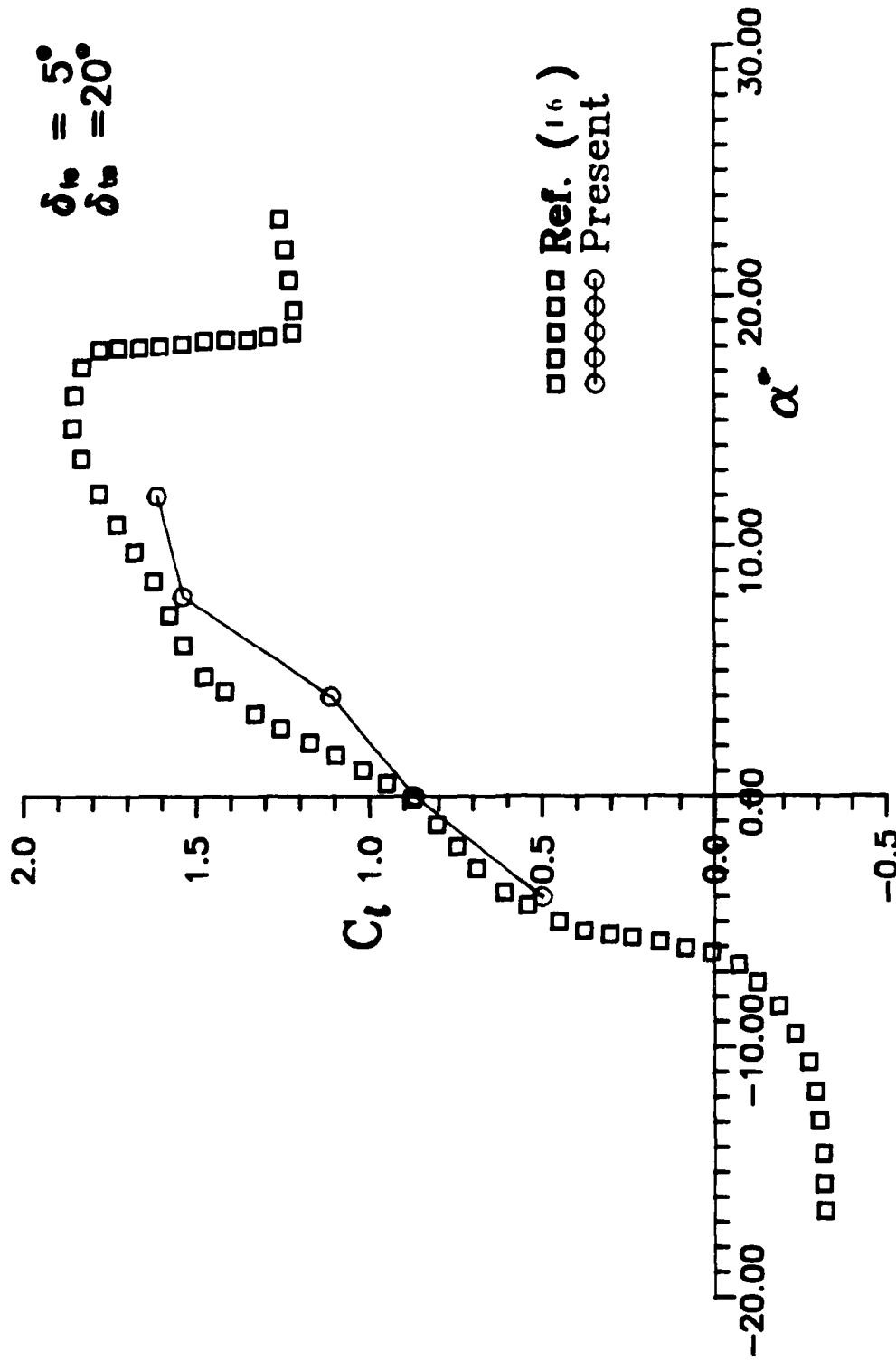


Figure 27 Comparison: Lift Coefficient vs. Angle of Attack
Wortman Airfoil, $\delta_{tr} = 20^\circ$, $\delta_{tr} = 5^\circ$

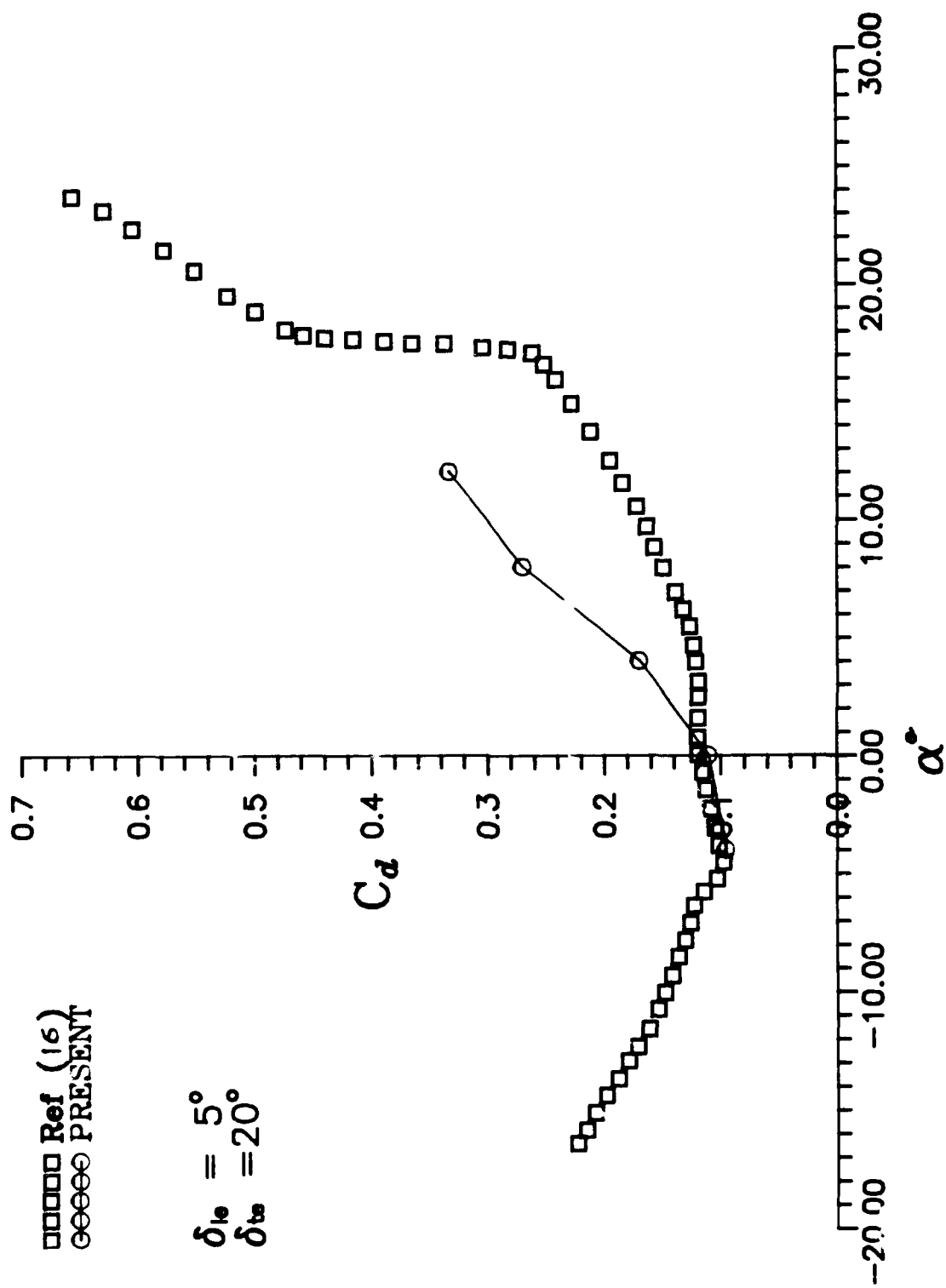


Figure 28 Comparison: Drag Coefficient vs. Angle of Attack
Wortman Airfoil, $\delta_{tr} = 20^\circ$, $\delta_{le} = 5^\circ$

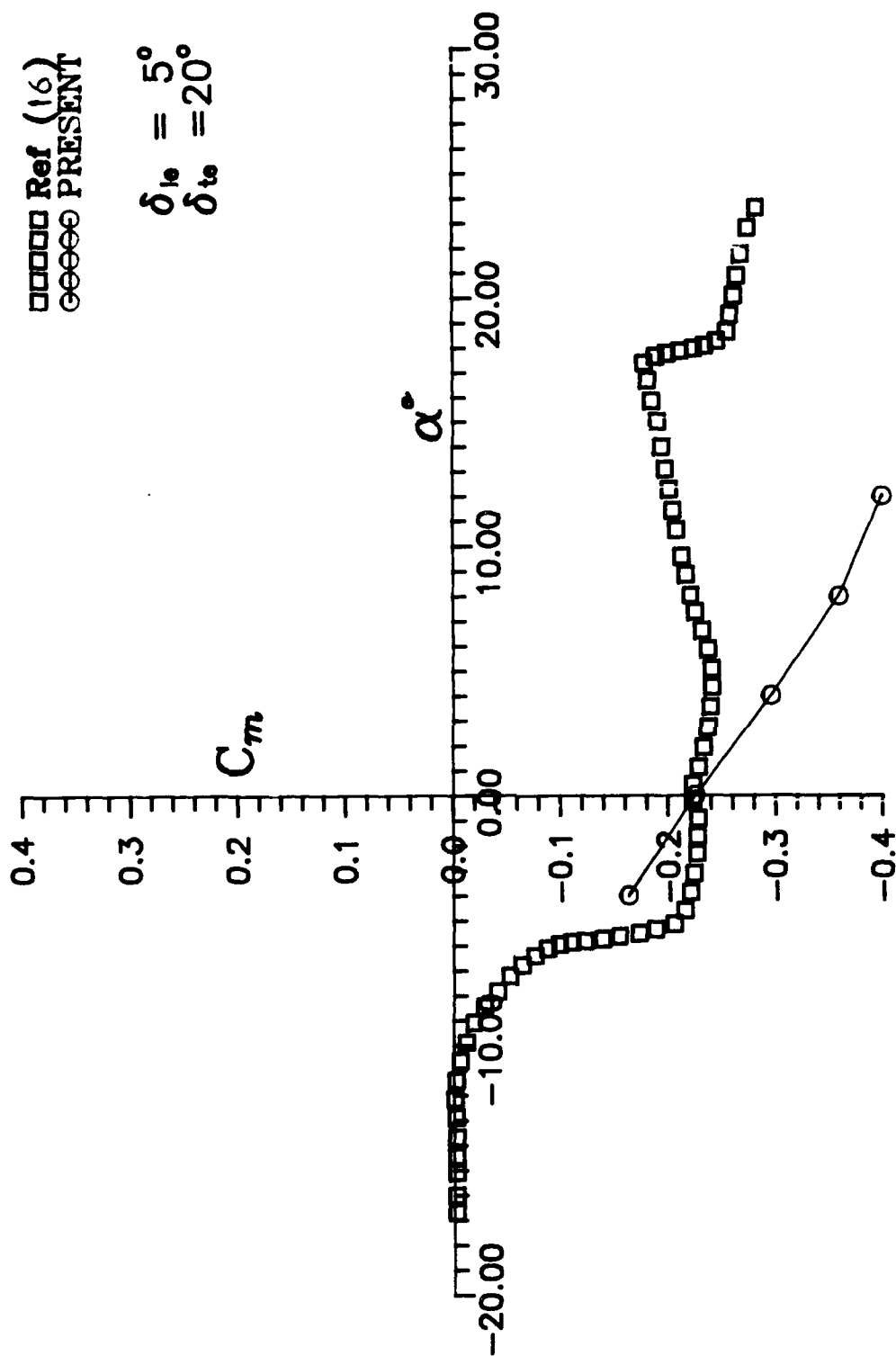


Figure 29 Comparison: Moment Coefficient vs. Angle of Attack
Wortman Airfoil, $\delta_{te} = 20^\circ$, $\delta_{le} = 5^\circ$

of attack the disparity is larger and is more than the acceptable limits. Figure 21 also compares the present data with data reported by Williams [28] for the no deflections case and various Reynolds numbers. It can be seen that this data is also significantly different from Ref [16]. For Ref. [28] the lift curve slope is greater, however in the present case, the lift curve slope is lower than Perry [16]. Another point to note is that airfoil stalls at quite different values of α for Ref. [16] and Ref [28] (The present results reflect the uncertain data scattering of experimental measurements, at low Reynolds conditions).

On Drag Coefficient. The drag coefficient has been plotted as a function of angle of attack in Figures 22, 25 and 28, The drag distribution is not linear, but is closer to parabolic. Because of the limited α range considered the variation of C_d beyond the tested values cannot be predicted. In comparison to the other cases, the data set corresponding to leading edge deflection of 5° is the closest to the data reported by Perry. For all cases the variance between present and Perry is greatest at higher angles of attack, in comparison to values of α close to zero, where the agreement is very good. Figure 22 also compares C_d variation with Ref. [28] the values reported are an order of magnitude lower than those reported by Perry. In fact the magnitude difference in measurements between [16] and [28] is similar to the disparity between present calculations and data of Ref.[16].

On Moment Coefficient. Positive pitching moment is defined in this study as one, which causes a nose down motion of the airfoil. In all the cases considered the variation of moment coefficient with α is almost linear. This can be clearly seen in Figures 23, 26 and 29, along with the fact that agreement with experimental data is pretty good within the $\alpha = \pm 4$ degree range. For higher values of angle of attack, that is 8 and 12 degrees, no agreement between data and calculations is reached. Similar to the the drag and lift coefficients, the case with leading edge deflected of 5 degrees is closest to experimental data, in comparison with the other two cases. The attention should also be focused on the fact that the data from Ref. [28] is quite different than Ref. [16]. The significant discrepancy in experimental measurements and between numerical simulation suggest a continuous research effort in this area are still required.

On Pressure Peak. Close examination of the C_p plots Figures 52 through 67 shows that at smaller angles of attack, it is very hard to pick out the location at which minimum pressure occurs as the C_p variation is quite flat. However, as the angle of attack is increased the point of min. pressure becomes more and more distinct and moves upstream, towards the leading edge.

Table 2 Comparison of separation and reattachment points

Wortman FX 63-137 airfoil, $\delta_{te} = \delta_{le} = 0^\circ$

(a) Lower surface

α°	Present	Bastedo $Re=2 \times 10^5$ Ref. [5]	Williams $Re=7 \times 10^5$ Ref. [28]
-4	0.75 \rightarrow x	----	0.63 \rightarrow 0.78
0	0.60 \rightarrow x	0.59 \rightarrow 0.82	0.52 \rightarrow 0.70
4	0.65 \rightarrow 0.72 0.95 \rightarrow x	0.48 \rightarrow 0.72	0.47 \rightarrow 0.64
8	0.49 \rightarrow x	0.31 \rightarrow 0.60	0.40 \rightarrow x
12	0.43 \rightarrow 0.51 0.60 \rightarrow x	----	0.11 \rightarrow 0.16 0.75 \rightarrow x
16	0.17 \rightarrow 0.36 0.38 \rightarrow 0.47 0.48 \rightarrow x	----	0.05 \rightarrow 0.12 0.50 \rightarrow x

(b) Lower surface

α°	Present	Bastedo $Re=2 \times 10^5$ Ref. [5]	Williams $Re=7 \times 10^5$ Ref. [28]
-4	0.46 \rightarrow 0.68 0.82 \rightarrow 0.91	0.05 \rightarrow 0.08	0.05 \rightarrow 0.08
0	0.32 \rightarrow 0.81	0.38 \rightarrow 0.52	0.40 \rightarrow 0.49
4	0.66 \rightarrow 0.67 0.95 \rightarrow 0.99	0.48 \rightarrow 0.68	0.48 \rightarrow 0.52
8	0.53 \rightarrow 0.76	0.60 \rightarrow 0.78	0.62 \rightarrow 0.68
12	NIL	NIL	NIL
16	NIL	NIL	NIL

The same deductions can be arrived at by observing the constant velocity contour plots, given in Figures 36 through 51, where it can be seen that as the angle of attack is increased, the point of minimum pressure, which is also the point of maximum velocity moves towards the leading edge.

A point to note in Figures 59 through 67 is that the pressure coefficient shows a small spike of same magnitude and is located at the same place ($x/c = 0.13$) for all cases, with slat deflection. This spike has been generated due the slat deflection, and can be removed by smoothing the metric discontinuity at this point on the airfoil.

On Laminar Separation. The point of laminar flow separation is defined by the location of the vanishing skin friction coefficient. The relation of the point of separation with angle of attack can be observed from the stream line plots given in Figures 36 through 51. The exact location of the separation point can be found from the skin friction distribution, which is plotted as a function of chord in Figures 52 through 67. Note that at the point of separation the values of the stream function as well as the vorticity are zero.

From the stream function contours it can be very easily observed that as angle of attack is increased, the point of separation on the upper surface moves upstream towards the leading edge and the separation bubble becomes bigger in length and height. On the lower surface however, the point

of separation moves downstream and the separation bubble becomes smaller and smaller in length till it completely vanishes. The fore mentioned phenomenon can be explained by the fact that on the upper surface the adverse pressure gradient becomes stronger as α is increased, which triggers earlier separation. On the lower surface, the opposite takes place as flow on this side has greater momentum which helps to overcome the adverse gradient causing the point of separation to move downstream. This trend is most evident from the data presented in Tables 2 through 4. These tables compare the values of separation and reattachment for the present study, with flow visualization results of previous experiments, wherever available (a x identifies no reattachment).

Table 3 Comparison of separation and reattachment points
Wortman FX 63-137 airfoil $\delta_{1e}=5^\circ$, $\delta_{te}=0^\circ$

α°	Present		Perry Re=1x10 Ref. [16]
	Lower surf.	Upper surf.	Upper surf.
-4	0.24 \rightarrow 0.38	0.75 \rightarrow 0.79	-----
0	0.40 \rightarrow 0.59	0.58 \rightarrow 0.99	-----
4	0.53 \rightarrow 0.71	0.64 \rightarrow 0.71	0.55 \rightarrow 0.75
8	0.49 \rightarrow x	0.43 \rightarrow 0.71	0.40 \rightarrow 0.60
12	0.43 \rightarrow 0.71	0.35 \rightarrow 0.54	0.20 \rightarrow 0.30 0.85 \rightarrow x

Table 4 Comparison of separation and reattachment points

Wortman FX 63-137 airfoil $\delta_{1e}=5^\circ$, $\delta_{2e}=20^\circ$

α°	Present		Perry Re=1x10 Ref. [16]
	Lower surf.	Upper surf.	Upper surf.
-4	0.01 \rightarrow 0.10	0.53 \rightarrow 0.91	-----
0	0.37 \rightarrow 0.75 0.21 \rightarrow 0.73	0.57 \rightarrow 0.90	-----
4	0.36 \rightarrow 0.74	0.49 \rightarrow 0.84	0.60 \rightarrow 0.70
8	0.36 \rightarrow 0.82	0.27 \rightarrow 0.51 0.66 \rightarrow 0.96	0.35 \rightarrow 0.60 0.75 \rightarrow x
12	0.44 \rightarrow 0.77	0.41 \rightarrow 0.78 0.83 \rightarrow 0.91	0.20 \rightarrow 0.30 0.75 \rightarrow x

Effect of Slat Deflection

The slat constitutes 13% of the chord and in this case has been deflected by an angle of 5 degrees. Downward deflection of slat is defined positive.

On lift coefficient. The effect can be best evaluated by observing Figure 30, which is the comparison of lift curve slopes for the three different cases. Comparing the case of no slat deflection with the case of 5 degree deflection, it can be seen that at small angles of attack lift coefficient for the Wortman Airfoil with slat deflection is slightly less than compared to the no deflection case. However, at higher angles of attack, the opposite is true.

The above observations have also been reported by Perry [16], who points out that at deflection of slats increases the value of the critical angle (angle at which an abrupt change of parameters takes place; stall).

These observations can be best explained by the following; at lower angles of attack and slat deflection, the effective angle of attack seen by the airfoil leading edge decreases, causing reduction of the pressure peak and it's movement downstream. The net results is a reduction in lift. At higher angles of attack, however, downstream movement of the point of minimum pressure delays laminar separation and hence stall, this improves airfoil performance and increases the critical angle.

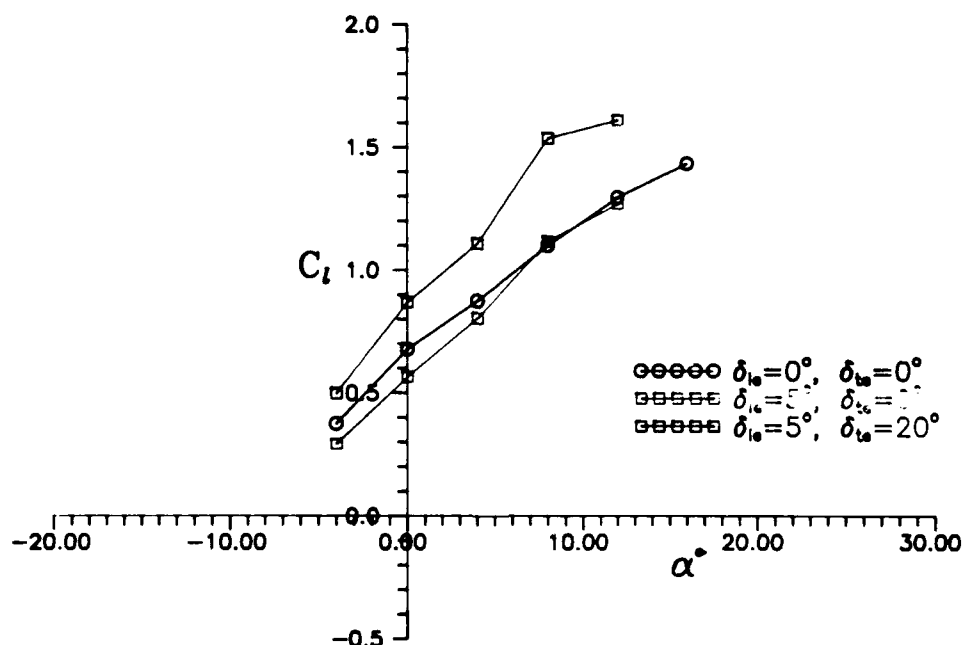


Figure 30 Effect of slat and flap deflections on lift coefficient

On Drag Coefficient. The effect of slat deflection on the drag coefficient is made obvious by comparing the case of no deflection, with the case of 5 degree slat deflection in Figure 31. Almost no change in c_d occurs due to the slat deflection. Perry [16] also reports a similar finding, for the angle of attack range considered. The effect of slat deflections of 10 degrees and greater is felt only when the angle of attack is greater than 16 degrees and less than -8 degrees.

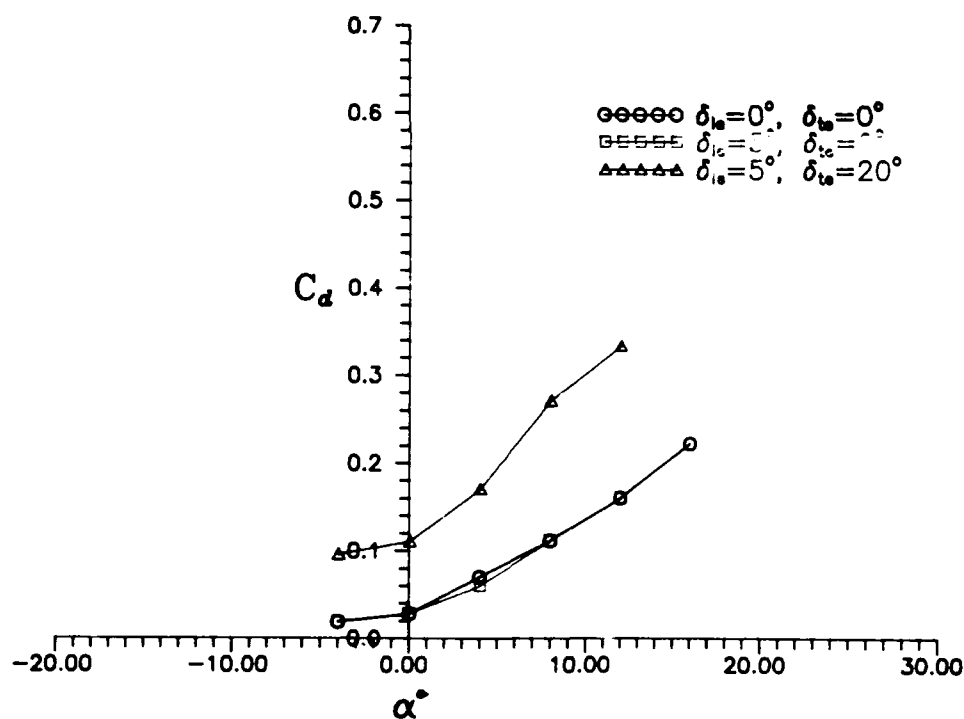


Figure 31 Effect of slat and flap deflections on drag coefficient

On Moment Coefficient. For the leading edge deflection of 5 degrees, the effect on moment coefficient is negligible. This can be observed from Figure 32, where the moment coefficient for the deflected case is compared to the un-deflected case. Perry [16] also reports a similar finding for the deflection angle and angle of attack range, being considered here.

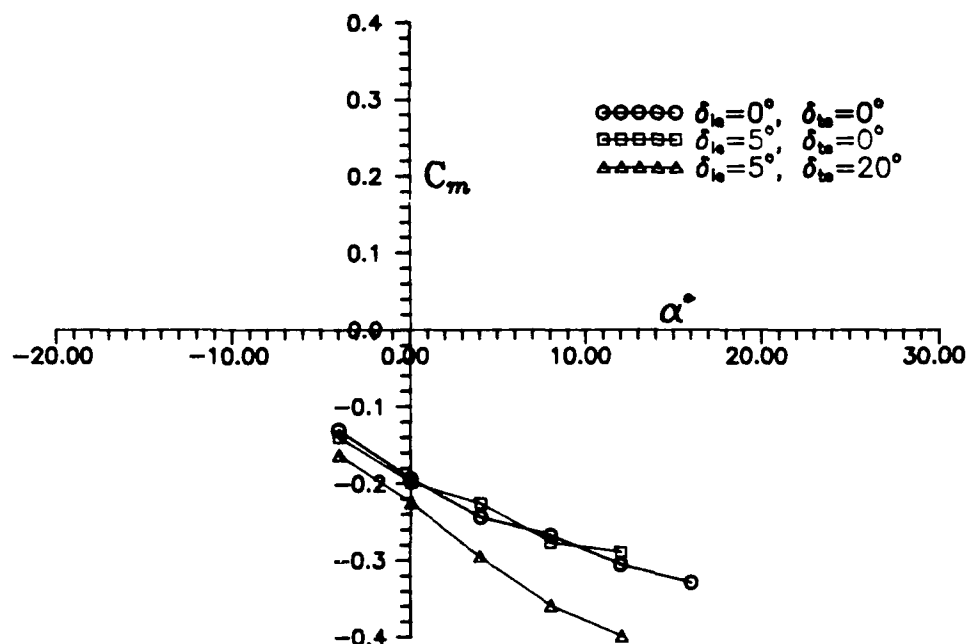


Figure 32 Effect of slat and flap deflections on moment coefficient

On Pressure Peak. Comparison of the pressure coefficient plots for the undeflected case in Figures 52 through 54 with the slat deflected case in Figures 55 through

57 shows very small localized changes in the leading edge zone. The observation is anticipated, that is, slat deflection causes the point of minimum pressure to move downstream and reduces the pressure peak. For all the cases with slat deflection, a spike in C_p distribution to appears at the slat rotation point. This anomaly is induced by the metric discontinuity at that point on the upper surface. This minor discrepancy can be eliminated by smoothing the upper surface at that point.

On Separation Point. Effect of the slat deflection on the separation points can be evaluated by comparing the separation points given in Table 3 for slat deflection with separation point data given in Table 2 for the un-deflected case. There is negligible change in the location of the separation point. This, however, would not be true for large slat deflections.

Effect of Flap Deflection

The Flap constitutes 25% of the chord and in this case has been deflected by an angle of 20 degrees. The downward deflection of the flap has been defined positive.

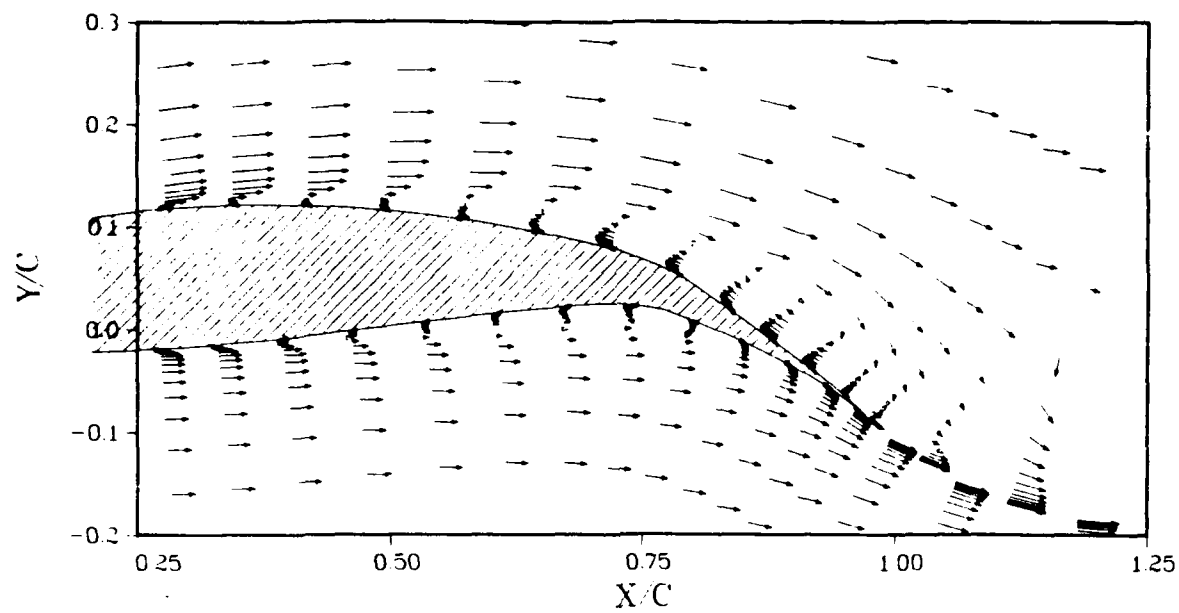
On Lift Coefficient. There is a significant increase in the lift coefficient due to flap deflection, depicted in Figure 30. The complete lift curve slope has been shifted upwards, this is the usual characteristic of flap deflection. Due to non-linearity and viscous effects, there

has been a very slight change in the lift curve slope also. The flap deflection has increased the slope by a very small value. It can be predicted that further increase in flap deflection angle will cause more shift of the curve in the same direction.

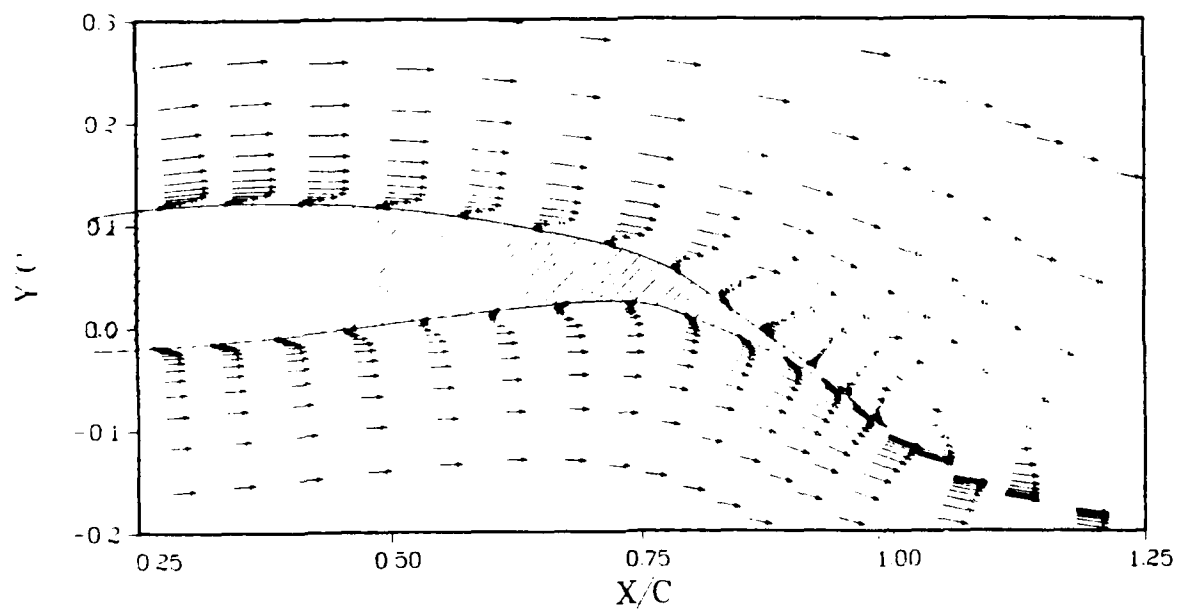
This increase in the lift coefficient can be explained by the constant stream function, vorticity contour plots (Figure 47 - 51) and the coefficient of pressure graphs (Figure 63 - 76). Due to flap deflection, the pressure distribution has been drastically changed. In the flap region a large suction exists on the upper surface, on the lower surface positive pressure has been also increased. This combined effect has been created due to the counter rotating flow occupying the void left by the deflected flap. This counter rotating flow can be observed in Figure 33, which shows the velocity vector plots for two of the flap deflected cases. This counter rotating vorticity strengthens the circulation around the airfoil, which increases the airfoil lift.

On Drag Coefficient. The change in drag coefficient due to flap deflection is presented in Figure 31. The complete curve has been shifted up by a certain constant value. The viscous effects and the non-linearities associated with this flow field have caused a slight change in the drag distribution.

Most of the increase in drag is due to the pressure



(a) $\alpha = 8^\circ$



(b) $\alpha = 12^\circ$

Figure 33 Velocity vector plots, Wortman airfoil
 $\delta_{1.0} = 5^\circ$, $\delta_{2.0} = 20^\circ$

differential (explained above), acting on the flap surface, with flap deflected, the wetted area (effective crosssectional area seen by the free stream) has also increased, which also contributes to an increase in drag.

On Moment Coefficient. The same phenomenon occurs for the moment coefficient as has been observed for the above two cases. Figure 32 shows that the moment coefficient curve has been shifted by a certain factor, with a small change in slope.

The increase of moment coefficient can be explained again as being the result of the large pressure differential acting on the airfoil surface, specifically in the flap region (the complete pressure distribution around the airfoil changes, to accommodate the increase in circulation). Due to the long moment arm, even a small change in the pressure distribution in the trailing edge zone result in significant changes in the moment coefficient.

On pressure peak. Comparing the pressure distributions of the flap deflected (Figures 64 - 67), with the un-deflected case (Figures 58 - 63) for all angles of attack, the trend is moving the point of minimum pressure towards the leading edge. A considerable increase in adverse pressure gradient on the upper surface and corresponding pressure rise on the lower surface are also detected.

On Separation Point. Due to the forward movement of the point of minimum pressure and the increase in adverse

pressure gradient acting on the upper surface, the point of separation occurs much closer to the leading edge. This can be observed from the constant stream function contours (Figures 47 - 51) and comparison of separation data given in Table 4 with separation data given in Tables 2 and 3. From the stream function and vorticity contours, note that as the angle of attack increases with flap deflection, the region of separated flow becomes larger with point of separation further upstream. As flap deflection or angle of attack is increased, the separation will become larger and will subsequently cause stall of the airfoil.

V Conclusions And Recommendations

The results obtained using the ANS code developed in this study compared favorably with experimental data for small angles of attack. For larger angles, the agreement needs improvement. However based on the codes performance, it can be said that the solutions obtained are still good approximation of the physical problem. It has also been observed that experimental data also varies from source to source and the discrepancies are comparable in magnitude, in comparison with numerical results obtained using the ANS equations.

The results indicate that deflection of the flaps causes earlier separation of the boundary layer and slat deflection tends to negate this effect. Because only a limited number of cases were computed, no optimization studies could be carried out.

Convergence characteristics of the solution is reasonable for the Reynolds number considered here, however, the code does have a Reynolds number limitation. No studies were carried out to find that limiting value, as it would vary from problem to problem. The code also exhibited some sensitivity to the initial conditions, improper initialization of the flow field causes delayed convergence in limit cases. This is because of the fact that the stream

function and vorticity equations are being solved in a coupled manner. The problem can be eliminated if the stream function equation is solved using direct methods at each time or iteration level. The recommended procedure may alleviate the sensitivity to initial conditions for convergence. It is also recommended that the ADI scheme may be used in conjunction with artificial damping, which will ultimately allow reduction in the Reynolds Number limitation and will also improve rate of convergence. It is also recommended that Baldwin-Lomax model be evaluated together with the Cebeci Smith model for turbulence for the investigated cases. It is felt that the large disparity at higher angles of attack is induced by the turbulence model to effectively handle the massive separations encountered in this study.

Finally it can be concluded that the ANS code holds good promise and refinements in the designated areas will allow its development into a good design tool.

APPENDIX A : Derivation of stream function and vorticity
transport equations

The non-dimensionalized Navier Stokes equations are

$$\frac{\partial u}{\partial x} + \frac{\partial v}{\partial y} = 0 \quad (30)$$

$$\frac{\partial u}{\partial t} + u \frac{\partial u}{\partial x} + v \frac{\partial u}{\partial y} = \frac{\partial P}{\partial x} + \frac{1}{Re} \frac{\partial}{\partial x} \left(\mu \frac{\partial u}{\partial x} \right) + \frac{\partial}{\partial y} \left(\mu \frac{\partial u}{\partial y} \right) \quad (31)$$

$$\frac{\partial v}{\partial t} + u \frac{\partial v}{\partial x} + v \frac{\partial v}{\partial y} = \frac{\partial P}{\partial y} + \frac{1}{Re} \frac{\partial}{\partial x} \left(\mu \frac{\partial v}{\partial x} \right) + \frac{\partial}{\partial y} \left(\mu \frac{\partial v}{\partial y} \right) \quad (32)$$

Differentiating equation (31) with respect to y and subtracting equation (32) differentiated with respect to x from the first eliminates the pressure term and the resulting equation reduces to the following.

$$\frac{\partial}{\partial y}(\text{Eqn. 32}) - \frac{\partial}{\partial x}(\text{Eqn. 31}) :$$

$$\begin{aligned} & + \frac{\partial}{\partial t} \left(\frac{\partial v}{\partial x} - \frac{\partial u}{\partial y} \right) + u \frac{\partial}{\partial x} \left(\frac{\partial v}{\partial x} - \frac{\partial u}{\partial y} \right) + v \frac{\partial}{\partial y} \left(\frac{\partial v}{\partial x} - \frac{\partial u}{\partial y} \right) \\ & = \frac{1}{Re} \left\{ \frac{\partial^2}{\partial x^2} \left(\mu \frac{\partial v}{\partial y} \right) - \frac{\partial^2}{\partial y \partial x} \left(\mu \frac{\partial u}{\partial x} \right) + \frac{\partial^2}{\partial y \partial x} \left(\mu \frac{\partial v}{\partial y} \right) - \frac{\partial^2}{\partial y^2} \left(\mu \frac{\partial u}{\partial y} \right) \right\} \quad (33) \end{aligned}$$

applying the defination of vorticity and stream function to the left hand side (LHS) of above equation results in the following form;

$$\rightarrow \text{LHS} = \frac{\partial \omega}{\partial t} + \frac{\partial \psi}{\partial y} \frac{\partial \omega}{\partial x} - \frac{\partial \psi}{\partial x} \frac{\partial \omega}{\partial y} \quad (34)$$

$$\text{where } \omega = \frac{\partial v}{\partial x} - \frac{\partial u}{\partial y} \quad (35)$$

$$\text{and } u = \frac{\partial \psi}{\partial y} \quad v = - \frac{\partial \psi}{\partial x} \quad (36)$$

the right hand side can be expanded term by term as follows

$$\frac{\partial^2}{\partial x^2} \left(\mu \frac{\partial v}{\partial x} \right) = \mu v_{xxx} + \mu_x v_{xx} + \mu_{xx} v_x + \mu_x v_{xx}$$

$$\frac{\partial^2}{\partial y \partial x} \left(\mu \frac{\partial u}{\partial x} \right) = \mu u_{xxy} + \mu_x u_{xy} + \mu_{xy} u_x + \mu_y u_{xx}$$

$$\frac{\partial^2}{\partial y \partial x} \left(\mu \frac{\partial v}{\partial y} \right) = \mu v_{yyx} + \mu_x v_{yy} + \mu_{xy} v_y + \mu_y v_{xy}$$

$$\frac{\partial^2}{\partial y^2} \left(\mu \frac{\partial u}{\partial y} \right) = \mu u_{yyy} + \mu_y u_{yy} + \mu_{yy} u_y + \mu_y u_{yy}$$

substituting the above expansions into RHS of equation (33) results in the following simplified form

$$\begin{aligned} \text{RHS} = -\frac{1}{Re} & \left(\mu \omega_{xx} + \mu \omega_{yy} + \mu_x \omega_x + \mu_y \omega_y + \mu_x v_{xx} + \mu_{xx} v_x - \mu_y u_{xx} \right. \\ & \left. + \mu_x v_{yy} - \mu_y u_{yy} - \mu_{yy} u_y - \mu_{xy} u_x + \mu_{xy} v_y \right) \end{aligned}$$

making use of the definitions of continuity (30) and vorticity (35) the above expression can be recast as follows.

$$\begin{aligned} \text{RHS} = \mu \omega_{xx} + 2 \mu_x \omega_x + \mu_{xx} \omega + \mu \omega_{yy} + 2 \mu_y \omega_y + \mu_{yy} \omega \\ + 2 \mu_{xy} v_{yy} + \mu_{xx} u_y - \mu_{yy} v_x \end{aligned}$$

it can be seen that the above expression is the expanded form of the following relation

$$\begin{aligned} \text{RHS} = & \frac{\partial}{\partial x} \left[\frac{\partial}{\partial x} (\mu \omega) \right] + \frac{\partial}{\partial y} \left[\frac{\partial}{\partial y} (\mu \omega) \right] - 2 \frac{\partial^2 \mu}{\partial x \partial y} \frac{\partial^2 \psi}{\partial x \partial y} \\ & + \frac{\partial^2 \mu}{\partial x \partial x} \frac{\partial^2 \psi}{\partial y \partial y} + \frac{\partial^2 \mu}{\partial y \partial y} \frac{\partial^2 \psi}{\partial x \partial x} \end{aligned}$$

Thus the vorticity transport equation is:

$$\begin{aligned} \frac{\partial \omega}{\partial t} + \frac{\partial \psi}{\partial y} \frac{\partial \omega}{\partial x} - \frac{\partial \psi}{\partial x} \frac{\partial \omega}{\partial y} = & \frac{1}{Re} \left\{ \frac{\partial}{\partial x} \left[\frac{\partial}{\partial x} (\mu \omega) \right] + \frac{\partial}{\partial y} \left[\frac{\partial}{\partial y} (\mu \omega) \right] \right. \\ & \left. - 2 \frac{\partial^2 \mu}{\partial x \partial y} \frac{\partial^2 \psi}{\partial x \partial y} + \frac{\partial^2 \mu}{\partial x \partial x} \frac{\partial^2 \psi}{\partial y \partial y} + \frac{\partial^2 \mu}{\partial y \partial y} \frac{\partial^2 \psi}{\partial x \partial x} \right\} \quad (37) \end{aligned}$$

Substituting the definition of stream function into the continuity equation causes it to vanish, therefore the stream function equation is obtained by substituting (36) into (35), which results in the following form.

$$\frac{\partial^2 \psi}{\partial x \partial x} + \frac{\partial^2 \psi}{\partial y \partial y} = \omega \quad (38)$$

Summarizing

Vorticity transport equation

$$\begin{aligned} \frac{\partial \omega}{\partial t} + \frac{\partial \psi}{\partial y} \frac{\partial \omega}{\partial x} - \frac{\partial \psi}{\partial x} \frac{\partial \omega}{\partial y} = & \frac{1}{Re} \left\{ \frac{\partial}{\partial x} \left[\frac{\partial}{\partial x} (\mu \omega) \right] + \frac{\partial}{\partial y} \left[\frac{\partial}{\partial y} (\mu \omega) \right] \right. \\ & \left. - 2 \frac{\partial^2 \mu}{\partial x \partial y} \frac{\partial^2 \psi}{\partial x \partial y} + \frac{\partial^2 \mu}{\partial x \partial x} \frac{\partial^2 \psi}{\partial y \partial y} + \frac{\partial^2 \mu}{\partial y \partial y} \frac{\partial^2 \psi}{\partial x \partial x} \right\} \quad (39) \end{aligned}$$

Stream function equation

$$\frac{\partial^2 \psi}{\partial x \partial x} + \frac{\partial^2 \psi}{\partial y \partial y} = \omega$$

APPENDIX B : Co-ordinate Transformation Relations

$$f_x = \frac{1}{J} \left[\left(y_{\eta} f \right)_{\xi} - \left(y_{\xi} f \right)_{\eta} \right] = \frac{1}{J} \left(y_{\eta} f_{\xi} - y_{\xi} f_{\eta} \right)$$

$$f_y = \frac{1}{J} \left[- \left(x_{\eta} f \right)_{\xi} + \left(x_{\xi} f \right)_{\eta} \right] = \frac{1}{J} \left(-x_{\eta} f_{\xi} + x_{\xi} f_{\eta} \right)$$

$$f_{xx} + f_{yy} = \frac{1}{J} \left\{ \left(\frac{\alpha}{J} f \right)_{\xi} - \left(\frac{\beta}{J} f \right)_{\eta} \right\}_{\xi} + \left(\frac{\gamma}{J} f \right)_{\eta} - \left(\frac{\beta}{J} f \right)_{\xi} \right\}$$

$$f_{xx} - f_{yy} = \frac{1}{J} \left\{ \left(\frac{\alpha'}{J} f \right)_{\xi} - \left(\frac{\beta'}{J} f \right)_{\eta} \right\}_{\xi} + \left(\frac{\gamma'}{J} f \right)_{\eta} - \left(\frac{\beta'}{J} f \right)_{\xi} \right\}$$

$$\xi_x = y_{\eta} J \quad \xi_y = -x_{\eta} J \quad \eta_x = -y_{\xi} J \quad \eta_y = x_{\xi} J$$

where f is any arbitrary function
and

$$J = x_{\xi} y_{\eta} - x_{\eta} y_{\xi}$$

$$\alpha = y_{\eta}^2 + x_{\eta}^2$$

$$\beta = y_{\eta} y_{\xi} + x_{\eta} x_{\xi}$$

$$\gamma = y_{\xi}^2 + x_{\xi}^2$$

$$\alpha' = y_{\eta}^2 - x_{\eta}^2$$

$$\beta' = y_{\eta} y_{\xi} - x_{\eta} x_{\xi}$$

$$\gamma' = y_{\xi}^2 - x_{\xi}^2$$

where subscripts denote differentiation w.r.t. variable

APENDIX C : Fortan listing of program "AIRFOIL"

```
PROGRAM AIRFOIL
C-----PROGRAM TO DEFLECT THE COORDINATES OF THE
C AIRFOIL'S LEADING AND TRAILING EDGE, AND SMOOTH THE DATA
C
  DIMENSION X(301),Y(301),XU(200),YU(200),XL(200),YL(200)
  CHARACTER*15 INPUT
C
  WRITE(*,*)' NAME OF FILE CONTAINING AIRFOIL DATA'
  READ(*,1)INPUT
1  FORMAT(A)
  OPEN(1,FILE=INPUT)
C-----READ AIRFOIL CONFIGURATION DATA
  WRITE(*,*)' SLAT LENGTH (CHORD RATIO)'
  READ(*,*)SLAT
  WRITE(*,*)' FLAP LENGTH (CHORD RATIO)'
  READ(*,*)FLAP
  WRITE(*,*)' SLAT DEFLECTION (DEGREES)'
  READ(*,*)SDA
  WRITE(*,*)' FLAP DEFLECTION (DEGREES)'
  READ(*,*)FDA
  PI=3.141592654
  SDA=SDA*PI/180.
  FDA=FDA*PI/180.
  AF = 1.0-FLAP
C-----READ AIRFOIL SURFACE
  KOUNT=0
5  CONTINUE
  READ(1,*,END=10)X(KOUNT+1),Y(KOUNT+1)
  KOUNT=KOUNT+1
  GOTO 5
10 CONTINUE
  CLOSE(1)
```

```

        NBODY=KOUNT
        WRITE(*,*)' NO OF POINTS READ IN, NBODY=',NBODY
C-----SET LEADING EDGE POINTER
        XMIN=1000
        DO 20 I = 1,NBODY
            IF(X(I) .LT. XMIN)THEN
                XMIN = X(I)
                JLE = I
            END IF
20      CONTINUE
C-----LOWER SURFACE POINTER
        KL=0
        DO 30 I = JLE,1,-1
            XL(KL+1)=X(I)
            YL(KL+1)=Y(I)
            KL=KL+1
30      CONTINUE
C-----UPPER SURFACE POINTER
        KU=0
        DO 40 I = JLE,NBODY
            XU(KU+1)=X(I)
            YU(KU+1)=Y(I)
            KU=KU+1
40      CONTINUE
C
C=====SLAT=====
C
C-----SET SLAT POINTERS-----
C----- (UPPER SURFACE)
        IF((SLAT .EQ. 0.0) .OR. (SDA .EQ. 0.0))GOTO 5000
        DO 50 I = 1,KU
            IF( XU(I) .EQ. SLAT) TSU = 1.0
            IF( XU(I) .LT. SLAT) THEN
                JSU=I
            END IF

```

```

50    CONTINUE
C------(LOWER SURFACE)
      DO 60 I = 1,KL
        IF( XL(I) .EQ. SLAT) TSL = 1.0
        IF( XL(I) .LT. SLAT) THEN
          JSL=I
        END IF
60    CONTINUE
C-----GENERATE POINTS CORRESPONDING TO SLAT
      YUSLAT=YU(JSU)+(YU(JSU+1)-YU(JSU))*(SLAT-XU(JSU))
1      /(XU(JSU+1)-XU(JSU))
      YLSLAT=YL(JSL)+(YL(JSL+1)-YL(JSL))*(SLAT-XL(JSL))
1      /(XL(JSL+1)-XL(JSL))
C------(UPPER SURFACE)
C-----CREATE CAVITY IN ARRAYS
      IF( TSU .EQ. 1.0) THEN
        JSU=JSU+1
      ELSE
        DO 70 I = KU,JSU+1,-1
          YU(I+1)=YU(I)
          XU(I+1)=XU(I)
70    CONTINUE
C-----INSERT INTO ARRAY
        YU(JSU+1)=YUSLAT
        XU(JSU+1)=SLAT
C-----RESET POINTERS
        KU=KU+1
        JSU=JSU+1
      END IF
C------(LOWER SURFACE)
C-----CREATE CAVITY IN ARRAYS
      IF( TSL .EQ. 1.0) THEN
        JSL=JSL+1
      ELSE
        DO 80 I = KL,JSL+1,-1

```

```

                YL(I+1)=YL(I)
                XL(I+1)=XL(I)
80      CONTINUE
C-----INSERT INTO ARRAY
                YL(JSL+1)=YLSLAT
                XL(JSL+1)=SLAT
C-----RESET POINTERS
                KL=KL+1
                JSL=JSL+1
      END IF

C
C-----ROTATE SLAT ACCORDING TO DEFLECTION ANGLE
C      APPLY COORDINATE TRANSFORMATION
C-----UPPER SURFACE
                XS=SLAT
                YS=YLSLAT+(YUSLAT-YLSLAT)/2.0
                SHYP=SQRT(XS*XS+YS*YS)
                SANG=ATAN2(YS,XS)
                DO 130 I = 1,JSU
                  CALL SROTAT(XS,YS,SHYP,SANG,SDA,XU(I),YU(I),XX,YY)
                  XU(I)=XX
                  YU(I)=YY
130     CONTINUE
C-----LOWER SURFACE
                DO 140 I = 1,JSL
                  CALL SROTAT(XS,YS,SHYP,SANG,SDA,XL(I),YL(I),XX,YY)
                  XL(I)=XX
                  YL(I)=YY
140     CONTINUE
                IF(SDA .GT. 0.0) THEN
C-----POSITIVE SLAT DEFLECTION
C-----REMOVE OVERLAPPING POINTS FROM LOWER
C      SURFACE
C-----FIND HOW MANY POINTS OVERLAP
                IFO=0

```

```

      DO 110 I = 1,JSL
        IF(XL(I) .GT. SLAT) THEN
          IFO=IFO+1
        END IF
110    CONTINUE
C-----REMOVE IFO NUMBER OF POINTS FROM LOWER
C          SURFACE
      JTEMP=JSL-IFO+1
      DO 120 I = JTEMP,KL-IFO
        XL(I)=XL(I+IFO)
        YL(I)=YL(I+IFO)
120    CONTINUE
C-----RESET POINTERS
      KL=KL-IFO
      JSL=JSL-IFO
C-----REMOVE POINTS FROM UPPER SURFACE FOR
C          CURVATURE CONTINUITY
      IF (ABS(SDA) .GT. 5*PI/180.0) THEN
        DO 181 I = JSU-1,KU-1
          XU(I)=XU(I+1)
          YU(I)=YU(I+1)
181    CONTINUE
        KU=KU-1
      END IF
    ELSE
C-----NEGATIVE SLAT DEFLECTION
C-----REMOVE OVERLAPPING POINTS FROM UPPER
C          SURFACE
C-----FIND HOW MANY POINTS OVERLAP
      IFO=0
      DO 111 I = 1,JSU
        IF(XU(I) .GT. SLAT) THEN
          IFO=IFO+1
        END IF
111    CONTINUE

```

```

C-----REMOVE IFO NUMBER OF POINTS FROM UPPER
C          SURFACE
      JTEMP=JSL-IFO+1
      DO 121 I = JTEMP,KU-IFO
        XU(I)=XU(I+IFO)
        YU(I)=YU(I+IFO)
121      CONTINUE
C-----RESET POINTERS
      KU=KU-IFO
      JSU=JSU-IFO
C-----REMOVE POINTS FROM LOWER SURFACE FOR
C          CURVATURE CONTINUITY
      IF (ABS(SDA) .GT. 5*PI/180.0) THEN
        DO 182 I = JSL-1,KL-1
          XL(I)=XL(I+1)
          YL(I)=YL(I+1)
182      CONTINUE
          KL=KL-1
        END IF
      END IF
5000 CONTINUE
C
C=====FLAP=====
C
C-----SET FLAP POINTERS-----
C------(LOWER SURFACE)
      IF(( FLAP .EQ. 0.0) .OR. (FDA .EQ. 0.0))GOTO 6000
      DO 51 I = 1,KL
        IF( XL(I) .EQ. AF) TFL = 1.0
        IF( XL(I) .LT. AF) THEN
          JFL=I
        END IF
51      CONTINUE
C------(UPPER SURFACE)
      DO 61 I = 1,KU

```

```

        IF( XU(1) .EQ. AF) TFU = 1.0
        IF( XU(1) .LT. AF) THEN
            JFU=1
        END IF
61    CONTINUE
C-----GENERATE POINT CORRESPONDING TO FLAPS
        YUFLAP=YU(JFU)+(YU(JFU+1)-YU(JFU))*(AF-XU(JFU))
        1 /(XU(JFU+1)-XU(JFU))
        YLFLAP=YL(JFL)+(YL(JFL+1)-YL(JFL))*(AF-XL(JFL))
        1 /(XL(JFL+1)-XL(JFL))
C-----CREATE CAVITY IN ARRAYS
C------(UPPER SURFACE)
        IF( TFU .EQ. 1.0) THEN
            JFU=JFU+1
        ELSE
            DO 90 I = KU,JFU+1,-1
                YU(I+1)=YU(I)
                XU(I+1)=XU(I)
90    CONTINUE
C-----RESET POINTERS
        KU=KU+1
        JFU=JFU+1
C-----INSERT INTO ARRAY
        YU(JFU)=YUFLAP
        XU(JFU)=AF
        END IF
C------(LOWER SURFACE)
        IF( TFL .EQ. 1.0) THEN
            JFL=JFL+1
        ELSE
            DO 100 I = KL,JFL+1,-1
                YL(I+1)=YL(I)
                XL(I+1)=XL(I)
100   CONTINUE
C-----RESET POINTERS

```

```

        KL=KL+1
        JFL=JFL+1
C-----INSERT INTO ARRAY
        YL(JFL)=YLFLAP
        XL(JFL)=AF
    END IF

C
C-----ROTATE FLAP ACCORDING TO DEFLECTION ANGLE
C          APPLY COORDINATE TRANSFORMATION
C-----UPPER SURFACE
        XF=AF
        YF=YLFLAP+(YUFLAP-YLFLAP)/2.0
        FHYP=SQRT(XF*XF+YF*YF)
        FANG=ATAN2(YF,XF)
        DO 170 I = JFU,KU
            CALL FROTAT(XF,YF,FHYP,FANG,FDA,XU(I),YU(I),XX,YY)
            XU(I)=XX
            YU(I)=YY
170    CONTINUE
C-----LOWER SURFACE
        DO 180 I = JFL,KL
            CALL FROTAT(XF,YF,FHYP,FANG,FDA,XL(I),YL(I),XX,YY)
            XL(I)=XX
            YL(I)=YY
180    CONTINUE
        IF(FDA .GT. 0.0)THEN
C-----POSITIVE FLAP DEFLECTION
C-----FIND HOW MANY POINTS OVERLAP ON LOWER
C          SURFACE
            IFO=0
            DO 150 I = JFL,KL
                IF(XL(I) .LT. AF) THEN
                    IFO=IFO+1
                END IF
150        CONTINUE

```



```

C-----REMOVE IFO NUMBER OF OVERLAPPING POINTS FROM
C          LOWER SURFACE
      DO 160 I = JFL,KL-IFO
        XL(I)=XL(I+IFO)
        YL(I)=YL(I+IFO)
160      CONTINUE
C-----RESET POINTERS
      KL=KL-IFO
C-----REMOVE POINTS FROM UPPER SURFACE FOR
C          CURVATURE CONTINUITY
      IF (TFU .EQ. 1.0) THEN
        NOPR=1
      ELSE
        NOPR=2
      END IF
      IF (ABS(FDA) .GT. 5*PI/180.) THEN
        DO 183 I = JFU,KU-NOPR
          XU(I)=XU(I+NOPR)
          YU(I)=YU(I+NOPR)
183      CONTINUE
          KU=KU-NOPR
        END IF
      ELSE
C-----NEGATIVE FLAP DEFLECTION
C-----FIND HOW MANY POINTS OVERLAP ON UPPER
C          SURFACE
        IFO=0
        DO 151 I = JFU,KU
          IF(XU(I) .LT. AF) THEN
            IFO=IFO+1
          END IF
151      CONTINUE
C-----REMOVE IFO NUMBER OF OVERLAPPING POINTS
C          FROM UPPER SURFACE
        DO 161 I = JFU,KU-IFO

```

```

        XU(1)=XU(1+IFO)
        YU(1)=YU(1+IFO)
161      CONTINUE
C-----RESET POINTERS
        KU=KU-IFO
C-----REMOVE POINTS FROM LOWER SURFACE FOR
C          CURVATURE CONTINUITY
        IF (TFL .EQ. 1.0) THEN
            NOPR=1
        ELSE
            NOPR=2
        END IF
        IF (ABS(FDA) .GT. 5*PI/180.) THEN
            DO 184 I = JFL,KL-NOPR
                XL(1)=XL(1+NOPR)
                YL(1)=YL(1+NOPR)
184      CONTINUE
            KL=KL-NOPR
        END IF
        END IF
6000     CONTINUE
C-----STORE BACK INTO ORIGINAL X, Y ARRAYS
        NBODY=0
        DO 200 I = KL,1,-1
            X(NBODY+1)=XL(1)
            Y(NBODY+1)=YL(1)
            NBODY=NBODY+1
200      CONTINUE
        DO 190 I = 2,KU
            X(NBODY+1)=XU(1)
            Y(NBODY+1)=YU(1)
            NBODY=NBODY+1
190      CONTINUE
        OPEN(2,FILE='OUT1.DAT')
        DO 210 I = 1,NBODY

```

```
WRITE(2,*)X(1),Y(1)
write(*,*)i,x(i),y(i)
210 CONTINUE
CLOSE(2)
END
```

C

```
SUBROUTINE SROTAT(XS,YS,SHYP,SANG,SDA,XP,YP,XX,YY)
XX= XS - SHYP*COS(SANG+SDA) + XP*COS(SDA) - YP*SIN(SDA)
YY= YS - SHYP*SIN(SANG+SDA) + XP*SIN(SDA) + YP*COS(SDA)
RETURN
END
```

C

```
SUBROUTINE FROTAT(XF,YF,FHYP,FANG,FDA,XP,YP,XX,YY)
XX= XF - FHYP*COS(-FANG+FDA) + XP*COS(FDA) + YP*SIN(FDA)
YY= YF + FHYP*SIN(-FANG+FDA) - XP*SIN(FDA) + YP*COS(FDA)
RETURN
END
```



Table 6 Upper surface co-ordinates Wortman FX63-137 airfoil

[illegible]

APPENDIX E : Linearization of vorticity and stream
function equations

The vorticity stream function equations in general coordinates are.

(stream function)

$$\frac{\partial}{\partial \xi} \left(\frac{\alpha}{J} \frac{\partial \psi}{\partial \xi} - \frac{\beta}{J} \frac{\partial \psi}{\partial \eta} \right) + \frac{\partial}{\partial \eta} \left(-\frac{\gamma}{J} \frac{\partial \psi}{\partial \eta} - \frac{\beta}{J} \frac{\partial \psi}{\partial \xi} \right) + J\omega = 0 \quad (40)$$

(vorticity transport)

$$J \frac{\partial \omega}{\partial t} + \frac{\partial \psi}{\partial \eta} \frac{\partial \omega}{\partial \xi} - \frac{\partial \psi}{\partial \xi} \frac{\partial \omega}{\partial \eta} = \frac{1}{Re} \left[\frac{\partial}{\partial \eta} \left(-\frac{\gamma}{J} \frac{\partial \mu \omega}{\partial \eta} \right) \right] \quad (41)$$

$$\text{let } \omega^{n+1} = \omega^n + \delta \omega^n \quad \text{and} \quad \psi^{n+1} = \psi^n + \delta \psi^n \quad (42)$$

where n and $n+1$ are successive time or iteration level

substituting equations (42) into the vorticity equation (41)

$$\begin{aligned} \rightarrow J(\omega^n + \delta \omega^n)_t + (\psi^n + \delta \psi^n)_\eta (\omega^n + \delta \omega^n)_\xi - (\psi^n + \delta \psi^n)_\xi (\omega^n + \delta \omega^n)_\eta \\ = \frac{1}{Re} \left(-\frac{\gamma}{J} \left(\mu (\omega^n + \delta \omega^n) \right)_\eta \right)_\eta \end{aligned}$$

expanding and neglecting terms $O(\delta)^2$

$$\begin{aligned} \rightarrow J \frac{\delta \omega^n}{\Delta t} + \omega_\xi^n \delta \psi_\eta^n + \psi_\eta^n \delta \omega_\xi^n - \omega_\eta^n \delta \psi_\xi^n - \psi_\xi^n \delta \omega_\eta^n - \frac{1}{Re} \left(-\frac{\gamma}{J} \left(\mu \delta \omega^n \right)_\eta \right)_\eta \\ = -\omega_\xi^n \psi_\eta^n + \psi_\eta^n \omega_\xi^n + \frac{1}{Re} \left(-\frac{\gamma}{J} \left(\mu \omega^n \right)_\eta \right)_\eta \end{aligned} \quad (43)$$

Same procedure can be applied to the stream function equation to transform it into the δ (delta) form, equation (40) thus

becomes.

$$\begin{aligned} & \left(\frac{\alpha}{J} \delta \psi_{\xi}^n - \frac{\beta}{J} \delta \psi_{\eta}^n \right)_{\xi} + \left(\frac{\gamma}{J} \delta \psi_{\eta}^n - \frac{\beta}{J} \delta \psi_{\xi}^n \right)_{\eta} + J \delta \omega^n \\ & = - \left(\frac{\alpha}{J} \psi_{\xi}^n - \frac{\beta}{J} \psi_{\eta}^n \right)_{\xi} - \left(\frac{\gamma}{J} \psi_{\eta}^n - \frac{\beta}{J} \psi_{\xi}^n \right)_{\eta} - J \omega^n \end{aligned} \quad (44)$$

it should be noted that all terms appearing as changes (delta's - δ) between successive levels are unknown, other exact variables are assumed known from the previous iteration level. Thus dropping the superscript the above derived relations take the final form.

$$\begin{aligned} J \frac{\delta \omega}{\Delta t} + \omega_{\xi} \delta \psi_{\eta} + \psi_{\eta} \delta \omega_{\xi} - \omega_{\eta} \delta \psi_{\xi} - \psi_{\xi} \delta \omega_{\eta} - \frac{1}{Re} \left(\frac{\gamma}{J} (\mu \delta \omega)_{\eta} \right)_{\eta} \\ = - \omega_{\xi} \psi_{\eta} + \psi_{\eta} \omega_{\xi} + \frac{1}{Re} \left(\frac{\gamma}{J} (\mu \omega)_{\eta} \right)_{\eta} \end{aligned} \quad (45)$$

$$\begin{aligned} & \left(\frac{\alpha}{J} \delta \psi_{\xi} - \frac{\beta}{J} \delta \psi_{\eta} \right)_{\xi} + \left(\frac{\gamma}{J} \delta \psi_{\eta} - \frac{\beta}{J} \delta \psi_{\xi} \right)_{\eta} + J \delta \omega \\ & = - \left(\frac{\alpha}{J} \psi_{\xi} - \frac{\beta}{J} \psi_{\eta} \right)_{\xi} - \left(\frac{\gamma}{J} \psi_{\eta} - \frac{\beta}{J} \psi_{\xi} \right)_{\eta} - J \omega \end{aligned} \quad (46)$$

APPENDIX F : Derivation of the pressure Poisson equation

The non-dimensionalized Navier Stokes equations are

$$\frac{\partial u}{\partial x} + \frac{\partial v}{\partial y} = 0 \quad (47)$$

$$\frac{\partial u}{\partial t} + u \frac{\partial u}{\partial x} + v \frac{\partial u}{\partial y} = \frac{\partial P}{\partial x} + \frac{1}{Re} \frac{\partial}{\partial x} \left(\mu \frac{\partial u}{\partial x} \right) + \frac{\partial}{\partial y} \left(\mu \frac{\partial u}{\partial y} \right) \quad (48)$$

$$\frac{\partial v}{\partial t} + u \frac{\partial v}{\partial x} + v \frac{\partial v}{\partial y} = \frac{\partial P}{\partial y} + \frac{1}{Re} \frac{\partial}{\partial x} \left(\mu \frac{\partial v}{\partial x} \right) + \frac{\partial}{\partial y} \left(\mu \frac{\partial v}{\partial y} \right) \quad (49)$$

Differentiating equation (48) with respect to x and adding to equation (49) differentiated with respect to y results in the following.

$$\begin{aligned} & \frac{\partial}{\partial x}(\text{Eqn. F.2}) + \frac{\partial}{\partial y}(\text{Eqn. F.3}) : \\ \rightarrow & \left(\frac{\partial u}{\partial x} \right)^2 + \left(\frac{\partial v}{\partial y} \right)^2 + 2 \frac{\partial u}{\partial y} \frac{\partial v}{\partial x} + \left(\frac{\partial^2 P}{\partial y^2} + \frac{\partial^2 P}{\partial x^2} \right) \\ & = \frac{1}{Re} \left\{ \frac{\partial^2}{\partial x^2} \left(\mu \frac{\partial u}{\partial x} \right) - \frac{\partial^2}{\partial y \partial x} \left(\mu \frac{\partial v}{\partial x} \right) + \frac{\partial^2}{\partial y \partial x} \left(\mu \frac{\partial u}{\partial y} \right) - \frac{\partial^2}{\partial y^2} \left(\mu \frac{\partial v}{\partial y} \right) \right\} \quad (50) \end{aligned}$$

the above expression has been simplified using continuity (47). Terms on the right hand side (RHS) can be expanded as follows

$$\frac{\partial^2}{\partial x^2} \left(\mu \frac{\partial u}{\partial x} \right) = \mu u_{xxx} + \mu_x u_{xx} + \mu_{xx} u_x + \mu_x u_{xx}$$

$$\frac{\partial^2}{\partial y \partial x} \left(\mu \frac{\partial v}{\partial x} \right) = \mu v_{xxy} + \mu_x v_{xy} + \mu_{xy} v_x + \mu_y v_{xx}$$

$$\frac{\partial^2}{\partial y \partial x} \left(\mu \frac{\partial u}{\partial y} \right) = \mu u_{yyx} + \mu_x u_{yy} + \mu_{xy} u_y + \mu_y u_{xy}$$

$$\frac{\partial^2}{\partial y^2} \left(\mu \frac{\partial v}{\partial y} \right) = \mu v_{yyy} + \mu_y v_{yy} + \mu_{yy} v_y + \mu_y v_{yy}$$

grouping and rearranging the above expanded terms results in the following simplified RHS for equation (50)

$$\begin{aligned} \text{RHS} = \frac{1}{Re} & \left\{ \mu_y (v_{xx} + v_{yy}) + \mu_x (u_{xx} u_{yy}) \right. \\ & \left. + u_x (\mu_{xx} + \mu_{yy}) + \mu_{xy} (\omega + u_y) \right\} \end{aligned}$$

substituting the above expression back into equation (50) leads to the following Poisson equation for pressure.

$$\begin{aligned} \nabla^2 P = & \left(\frac{\partial u}{\partial x} \right)^2 + \left(\frac{\partial v}{\partial y} \right)^2 + 2 \frac{\partial u}{\partial y} \frac{\partial v}{\partial x} + \frac{1}{Re} \left\{ \mu_y \nabla^2 v \right. \\ & \left. + \mu_x \nabla^2 u + u_x \nabla^2 \mu + \mu_{xy} (\omega + 2 u_y) \right\} \end{aligned} \quad (51)$$

$$\text{where } \nabla^2 = \frac{\partial^2}{\partial y^2} + \frac{\partial^2}{\partial x^2} \quad \& \quad \nabla'^2 = \frac{\partial^2}{\partial y^2} + \frac{\partial^2}{\partial x^2}$$

using the transformation relations given in Appendix B the Poisson equation for pressure in general coordinates is obtained, which is:

$$\begin{aligned}
& \left(\frac{\alpha}{J} p_{\xi} - \frac{\beta}{J} p_{\eta} \right)_{\xi} + \left(\frac{\gamma}{J} p_{\eta} - \frac{\beta}{J} p_{\xi} \right)_{\eta} = 2(u_{\xi} v_{\eta} - u_{\eta} v_{\xi}) \\
& + (x_{\xi} \mu_{\eta} - x_{\eta} \mu_{\xi}) \left\{ \left(\frac{\alpha}{J} v_{\xi} - \frac{\beta}{J} v_{\eta} \right)_{\xi} + \left(\frac{\gamma}{J} v_{\eta} - \frac{\beta}{J} v_{\xi} \right)_{\eta} \right\} \\
& + (y_{\eta} \mu_{\xi} - y_{\xi} \mu_{\eta}) \left\{ \left(\frac{\alpha}{J} u_{\xi} - \frac{\beta}{J} u_{\eta} \right)_{\xi} + \left(\frac{\gamma}{J} u_{\eta} - \frac{\beta}{J} u_{\xi} \right)_{\eta} \right\} \\
& + (y_{\eta} u_{\xi} - y_{\xi} u_{\eta}) \left\{ \left(\frac{\alpha}{J} \mu_{\xi} - \frac{\beta}{J} \mu_{\eta} \right)_{\xi} + \left(\frac{\gamma}{J} \mu_{\eta} - \frac{\beta}{J} \mu_{\xi} \right)_{\eta} \right\} \\
& + \left(\omega + 2(x_{\xi} u_{\eta} - x_{\eta} u_{\xi}) \right) \left\{ \left[\frac{\gamma}{J} (x_{\xi} \mu_{\eta} - x_{\eta} \mu_{\xi}) \right]_{\xi} \right. \\
& \quad \left. - \left[\frac{\gamma}{J} (x_{\xi} \mu_{\eta} - x_{\eta} \mu_{\xi}) \right]_{\eta} \right\} \quad (52)
\end{aligned}$$

The above relation is the Poisson equation for pressure in general coordinates and primitive variables, where 'ω' represents vorticity and 'u', 'v' the velocity components as defined in the physical domain, the metrics have been defined in Appendix B. Note that all terms on the right hand side are assumed known and the equations is solved for the only unknown variable 'P' pressure.

APPENDIX G : Derivation of force and moment coefficients

$$C_l \quad C_d \quad C_{m_{c/4}}$$

The forces acting on a body are basically the body forces (gravity) the shear forces (skin friction) and the pressure forces. For our analysis we will consider only the pressure and viscous forces (shear), the body forces are assumed negligible in comparison to the other forces.

Consider the dominant forces (pressure and shear) acting on the differential element shown in the following figure

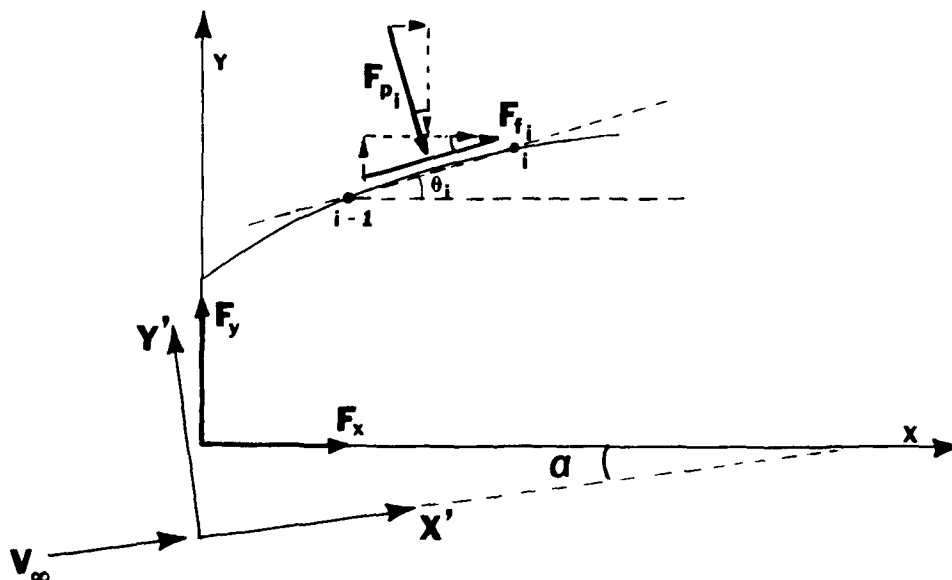


Figure 34 Forces acting on airfoil element

In the above figure x - y are the body axis (fixed to the chord of the airfoil) and x' - y' are the wind axis (alligned

and fixed with the freestream). The aerodynamic forces are usually measured with respect to the wind axis, the same has been followed through in this analysis.

F_{P_i} represents the force due to pressure acting on element 'i' and is defined as

$$F_{P_i} = P_i \rho_\infty u_\infty \Delta s_i \quad (53)$$

where P_i is non-dimensionalized pressure, $\rho_\infty u_\infty$ are the free stream properties and Δs_i is the element area

F_{ℓ_i} represents the force due to shear acting on element 'i' and is defined as

$$F_{\ell_i} = C_{\ell_i} \frac{1}{2} \rho_\infty u_\infty \Delta s_i \quad (54)$$

where C_{ℓ_i} is the skin friction coefficient defined as

$$C_{\ell_i} = \mu_i \left(\frac{\partial u}{\partial y} + \frac{\partial v}{\partial x} \right) \Big|_{i, y=0} = - \frac{2}{Re} \omega \Big|_{i, \eta=1} \quad (55)$$

Using principles of vector analysis the forces can be decomposed into the body axis system

$$\begin{aligned} F_{x_i} &= F_{\ell_i} \cos \theta_i + F_{P_i} \sin \theta_i \\ F_{y_i} &= F_{\ell_i} \sin \theta_i + F_{P_i} \cos \theta_i \end{aligned} \quad (56)$$

where F_x and F_y are the forces along the body axis system, subscript i indicates element dependence and θ_i is the local slope, given by

$$\theta_i = \tan^{-1} \left(\frac{\partial x}{\partial y} \right)_i \quad (57)$$

Lift and Drag computation

The forces in the body axis system can now be transformed into lift and drag using the following relations reference Figure 34.

$$\begin{aligned} L_i &= F_{y_i} \cos \alpha - F_{x_i} \sin \alpha \\ D_i &= F_{y_i} \sin \alpha + F_{x_i} \cos \alpha \end{aligned} \quad (58)$$

where L_i and D_i are the lift and drag forces acting on element i respectively and α is the airfoil angle of attack. Substituting equations (56) into the relations above result in the following simplified form for equations (58).

$$\begin{aligned} L_i &= F_{\ell_i} \sin(\theta_i - \alpha) - F_{p_i} \cos(\theta_i - \alpha) \\ D_i &= F_{\ell_i} \cos(\theta_i - \alpha) + F_{p_i} \sin(\theta_i - \alpha) \end{aligned} \quad (59)$$

The total lift and drag acting on the body is simply the summation of all element contributions, thus

$$L = \sum_{i=1}^{N-1} L_i \quad \& \quad D = \sum_{i=1}^{N-1} D_i \quad (60)$$

where N is the number of nodes.

Non-dimensionalizing the above relations and writing in coefficient form equations (60) transform to

$$C_L = \frac{2}{\rho_\infty u_\infty^2 c} \sum_{i=1}^{N-1} L_i \quad C_D = \frac{2}{\rho_\infty u_\infty^2 c} \sum_{i=1}^{N-1} D_i \quad (61)$$

where C_L and C_D now represent the lift and drag coefficients respectively for the section. Substituting equations (59) into the above relations results in the following after simplification.

$$C_L = \sum_{i=1}^{N-1} \left\{ \Delta s_i \left(C_{\ell_i} \sin(\theta_i - \alpha) - C_{p_i} \cos(\theta_i - \alpha) \right) \right\} \quad (62)$$

$$C_D = \sum_{i=1}^{N-1} \left\{ \Delta s_i \left(C_{\ell_i} \cos(\theta_i - \alpha) + C_{p_i} \sin(\theta_i - \alpha) \right) \right\}$$

Where $C_{p_i} = 2 P_i$ and $C_{\ell_i} = -2 w/Re$

Moment computation

Traditionally the moment acting on an airfoil is evaluated at the quarter chord location, and is therefore usually known as the "quarter chord moment". To evaluate this quantity, lets consider the following diagram, where F_x and F_y are the forces acting on the element 'i' given by relations (56).

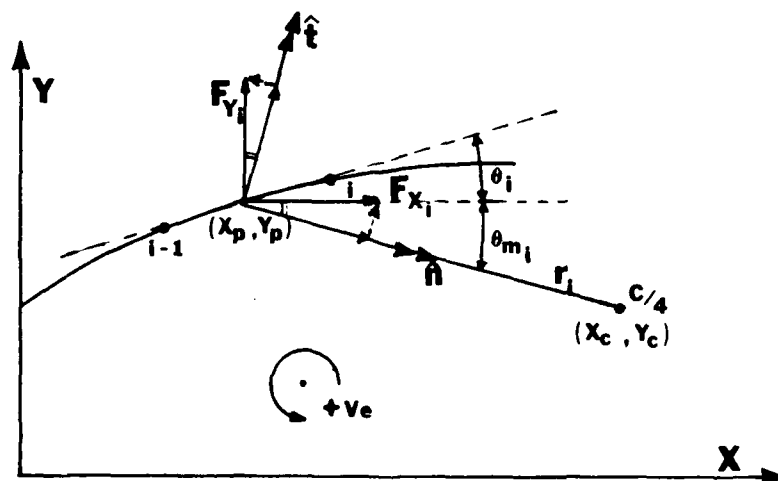


Figure 35 Moment acting on airfoil element

Then the moment about the quarter chord (x_c, y_c) due to forces acting on the element at location (x_p, y_p) is given by:

$$m_{c/4} = - r_i F_{t_i} \quad (63)$$

where r_i is the radial distance and F_{t_i} is the force acting tangent to the vector r_i (see diagram above).

Decomposing the forces F_{x_i} and F_{y_i} into the radial and tangential components results in the following expression for the tangential force.

$$F_{t_i} = F_{x_i} \sin \theta_m + F_{y_i} \cos \theta_m \quad (64)$$

substituting relations (56) above results in the following after simplification.

$$F_{t_i} = F_{\ell_i} \cos(\theta_i - \theta_m) - F_{p_i} \sin(\theta_i + \theta_m) \quad (65)$$

where θ_i is given by equation (57) and θ_m is defined below

$$\theta_m = \tan^{-1} \left(\frac{y_c - y_p}{x_c - x_p} \right) \quad (66)$$

substituting equation (65) into equation (63) and

integrating about the airfoil results in the following.

$$m_{c/4} = \sum_{i=1}^{N-1} \left\{ r_i \Delta s_i \left(F_{p_i} \cos(\theta_i + \theta_m) - F_{\ell_i} \sin(\theta_i - \theta_m) \right) \right\} \quad (67)$$

in coefficient form the above relation can be rewritten as:

$$C_{m_{c/4}} = \sum_{i=1}^{N-1} \left\{ r_i \Delta s_i \left(C_{p_i} \cos(\theta_i + \theta_m) - C_{\ell_i} \sin(\theta_i - \theta_m) \right) \right\} \quad (68)$$

where

$$r_i = \left[(x_p - x_c)^2 + (y_p - y_c)^2 \right]^{\frac{1}{2}} \quad (69)$$

Appendix H : Contour plots; Stream Function, Velocity and Vorticity

For all cases considered in this study, the contour plots have been plotted for the stream function, velocity (x-component of the total velocity) and vorticity, these are given as Figures 36 to 51.

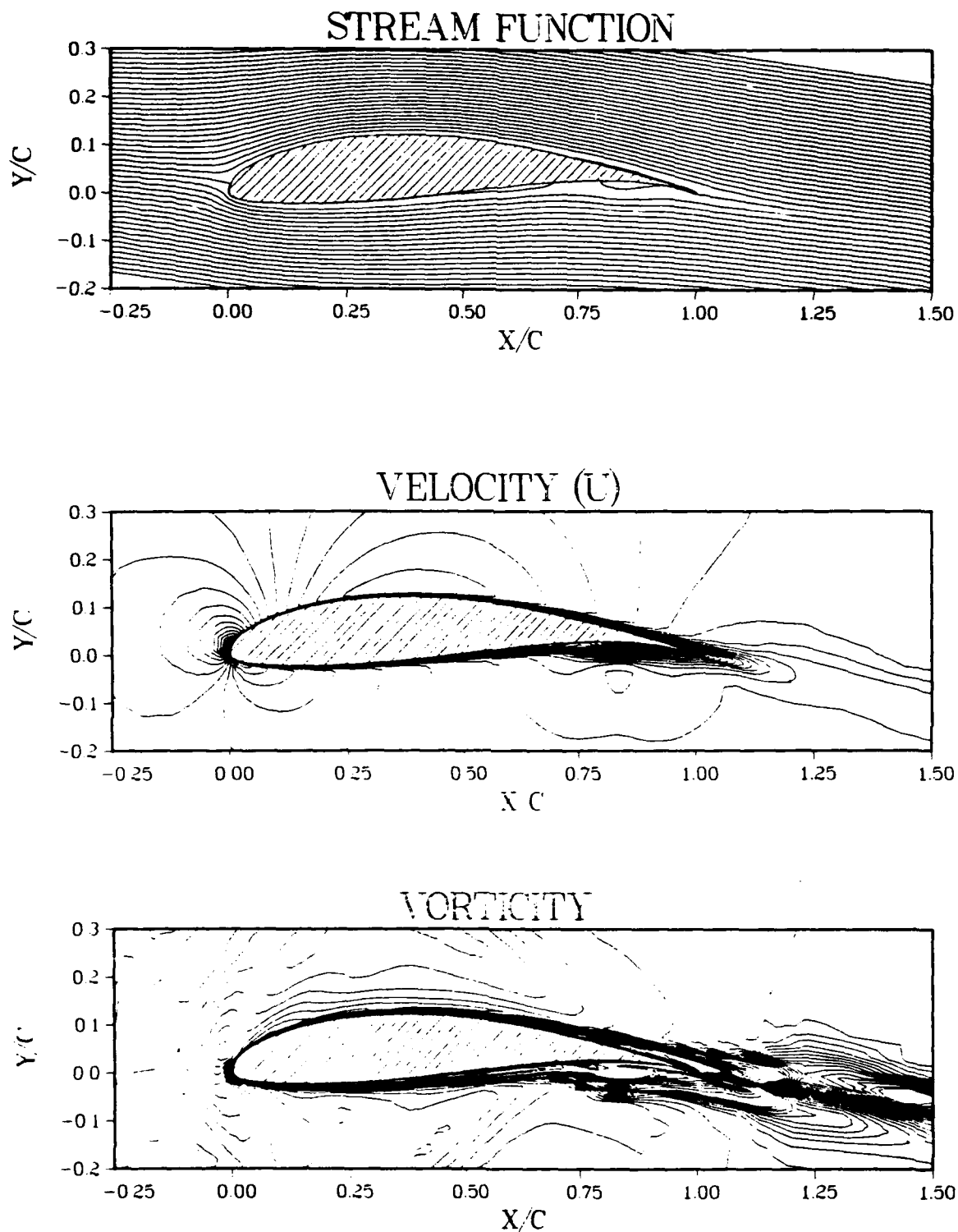


Figure 36 Constant stream function, velocity and vorticity contour plots for Wortman FX 63-137 airfoil, $\alpha = -4^\circ$, $\delta_{l,e} = 0^\circ$, $\delta_{t,e} = 0^\circ$, $Re = 1 \times 10^5$

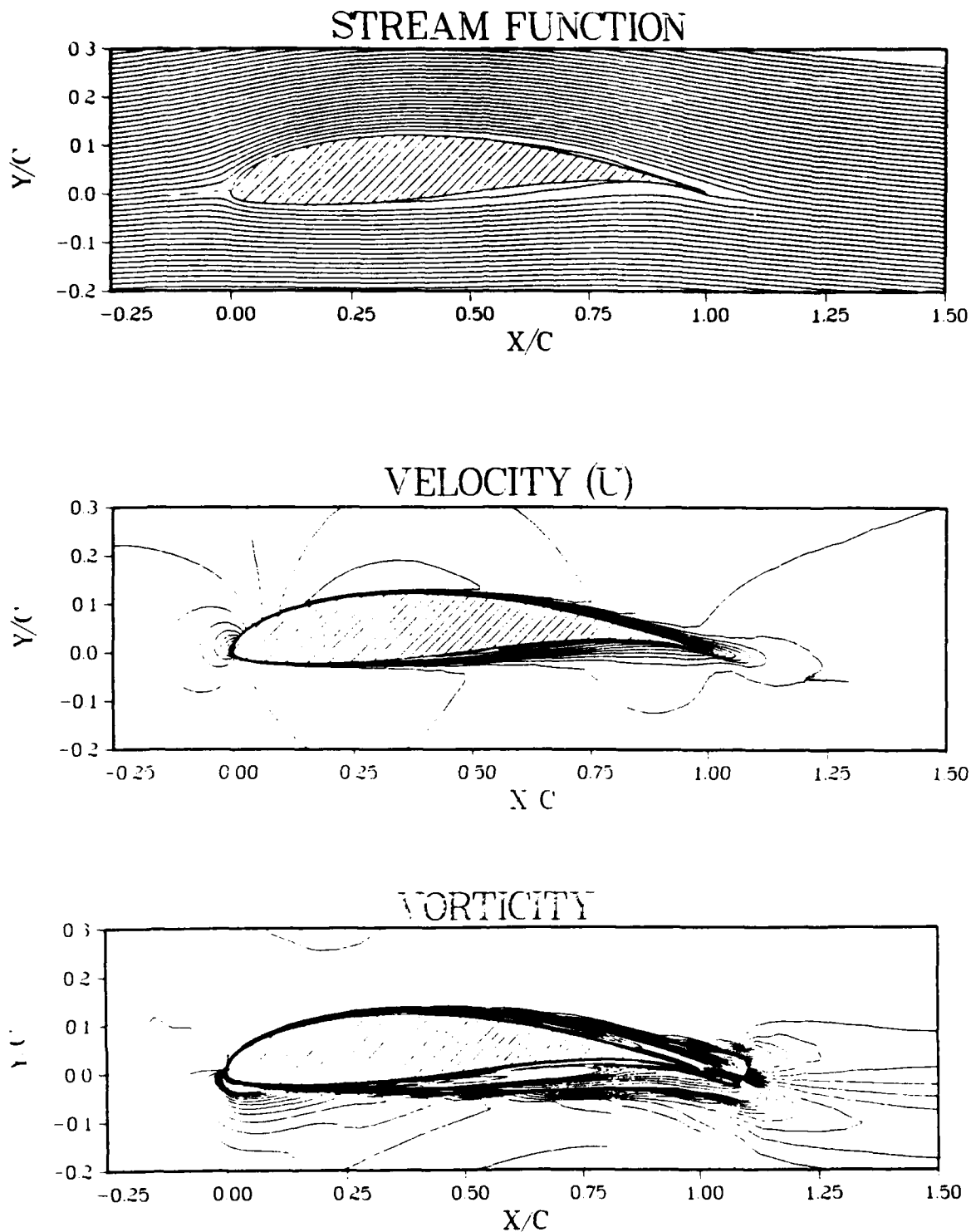


Figure 37 Constant stream function, velocity and vorticity contour plots for Wortman FX 63-137 airfoil, $\alpha = -4^\circ$, $\delta_{i,e} = 0^\circ$, $\delta_{t,e} = 0^\circ$, $Re = 1 \times 10^5$

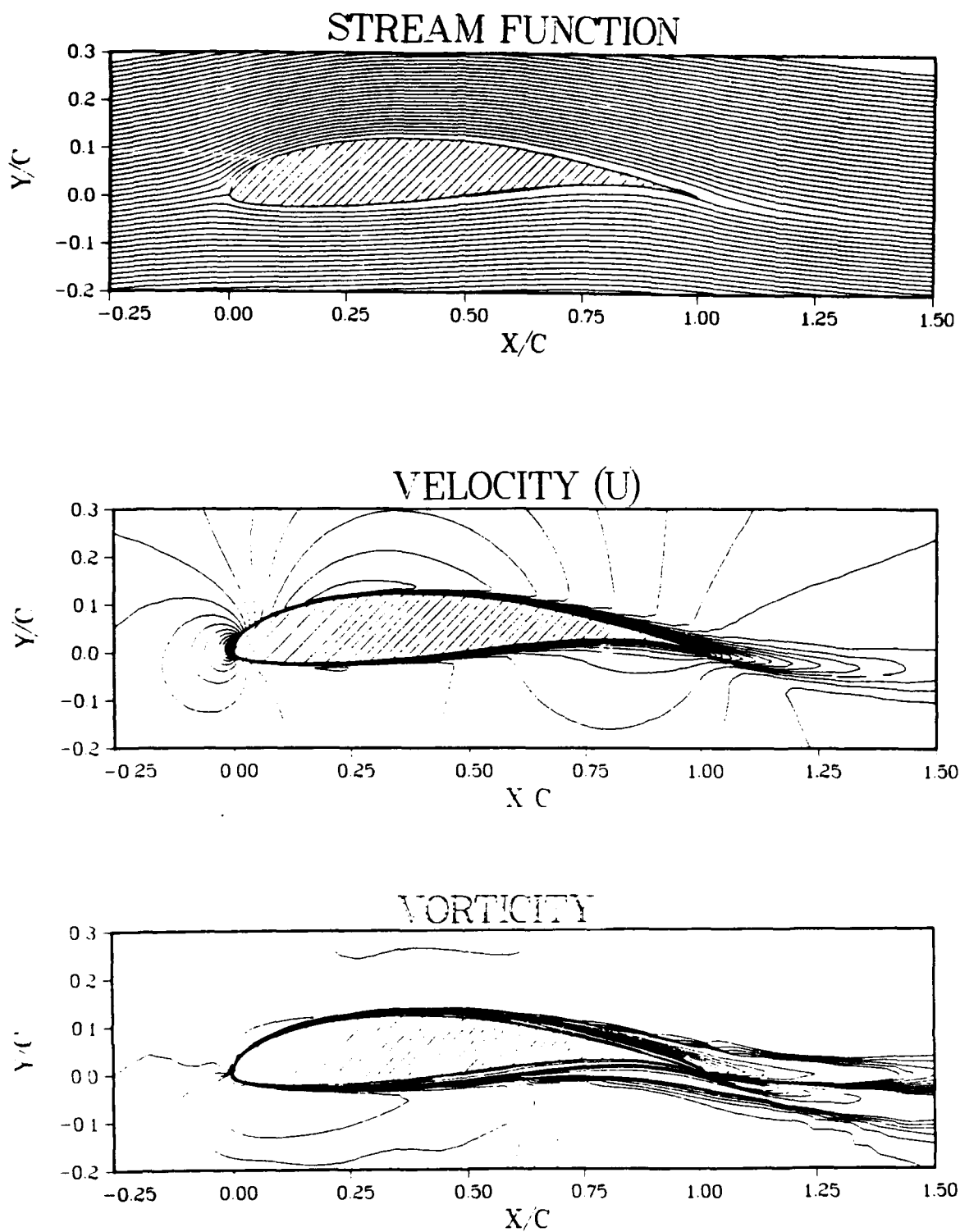


Figure 38 Constant stream function, velocity and vorticity contour plots for Wortman FX 63-137 airfoil, $\alpha = 4^\circ$, $\delta_{le} = 0^\circ$, $\delta_{te} = 0^\circ$, $Re = 1 \times 10^5$

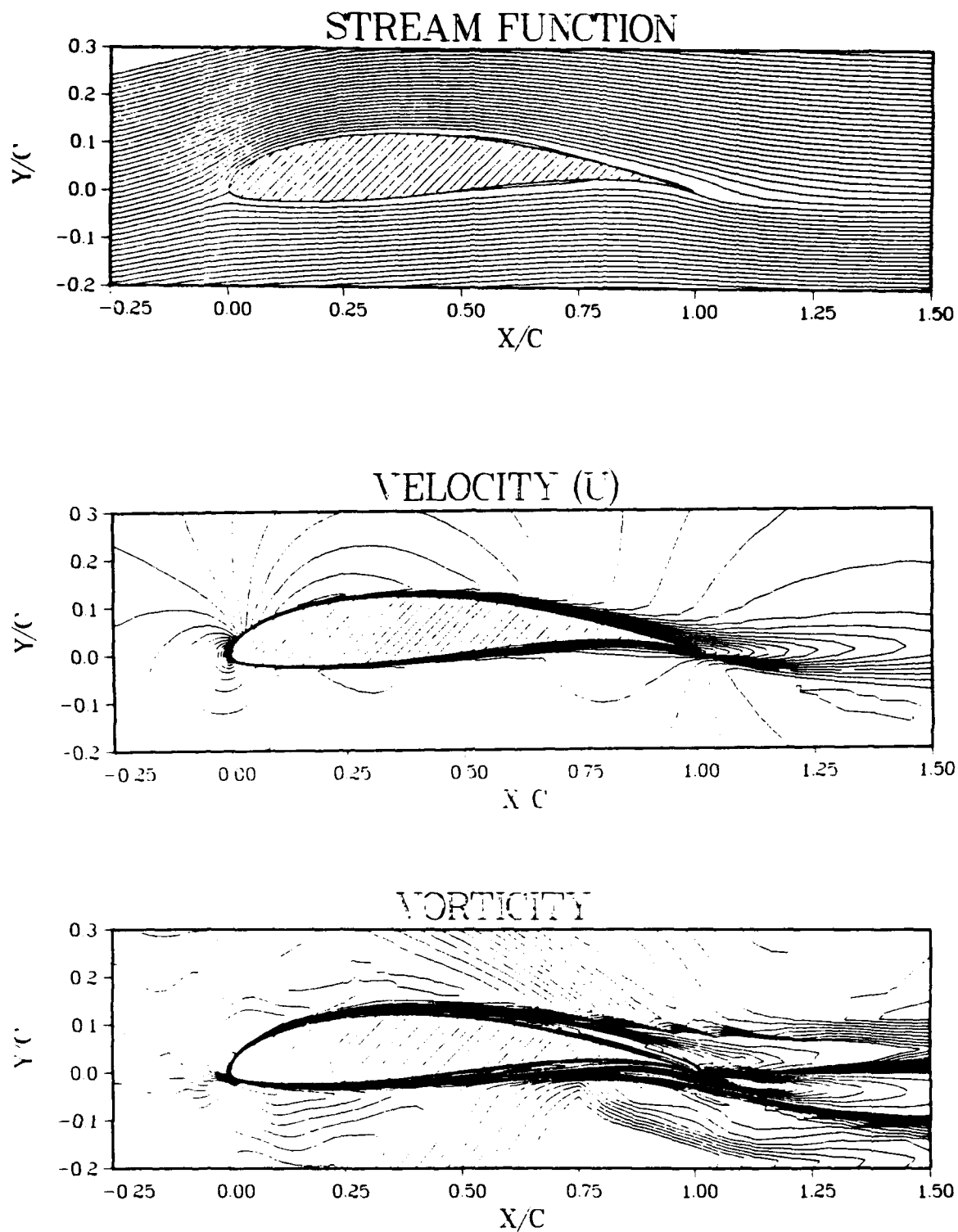


Figure 39 Constant stream function, velocity and vorticity contour plots for Wortman FX 63-137 airfoil, $\alpha = 8^\circ$, $\delta_{1e} = 0^\circ$, $\delta_{te} = 0^\circ$, $Re = 1 \times 10^5$

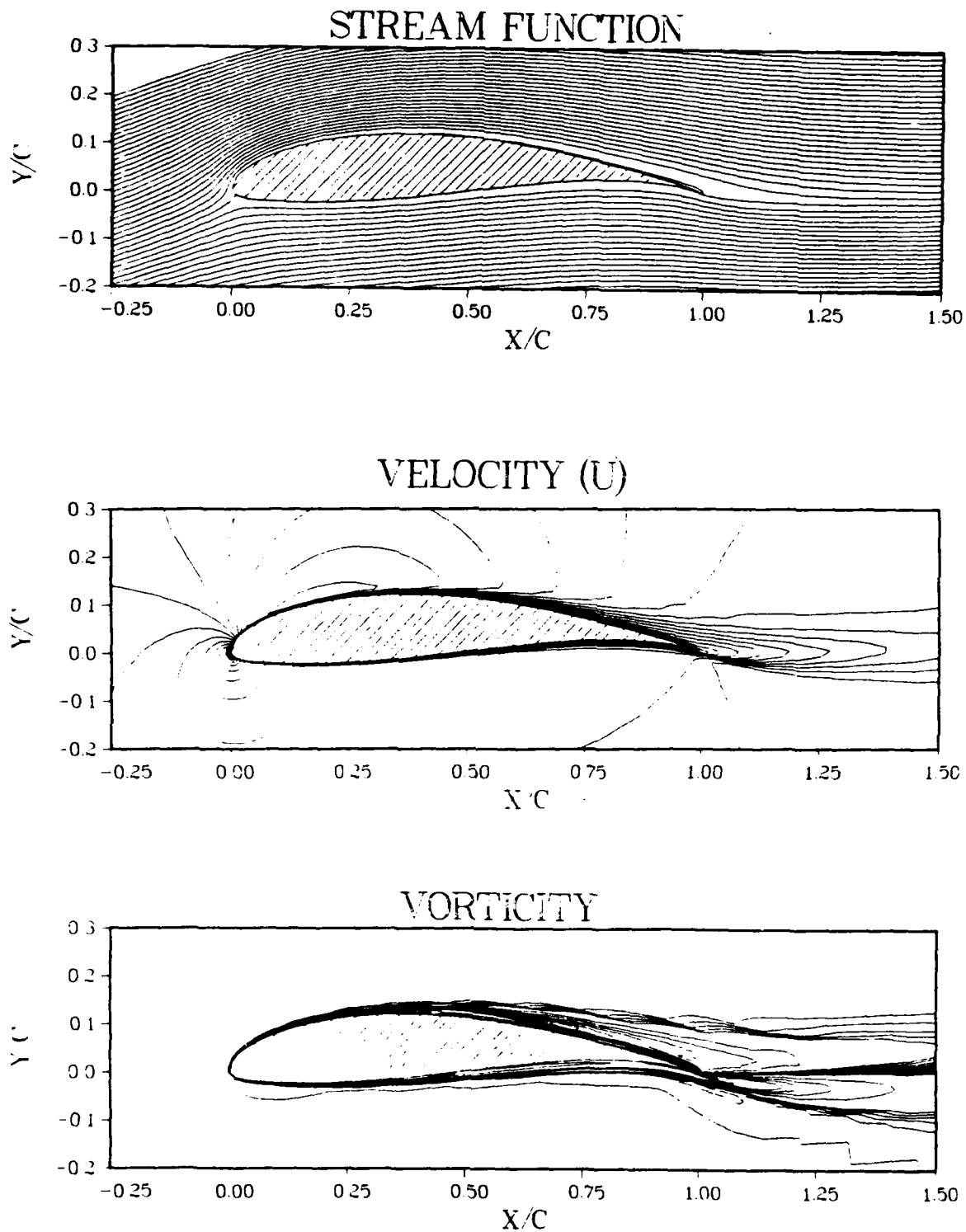


Figure 40 Constant stream function, velocity and vorticity contour plots for Wortman FX 63-137 airfoil, $\alpha = 12^\circ$, $\delta_{1e} = 0^\circ$, $\delta_{te} = 0^\circ$, $Re = 1 \times 10^5$

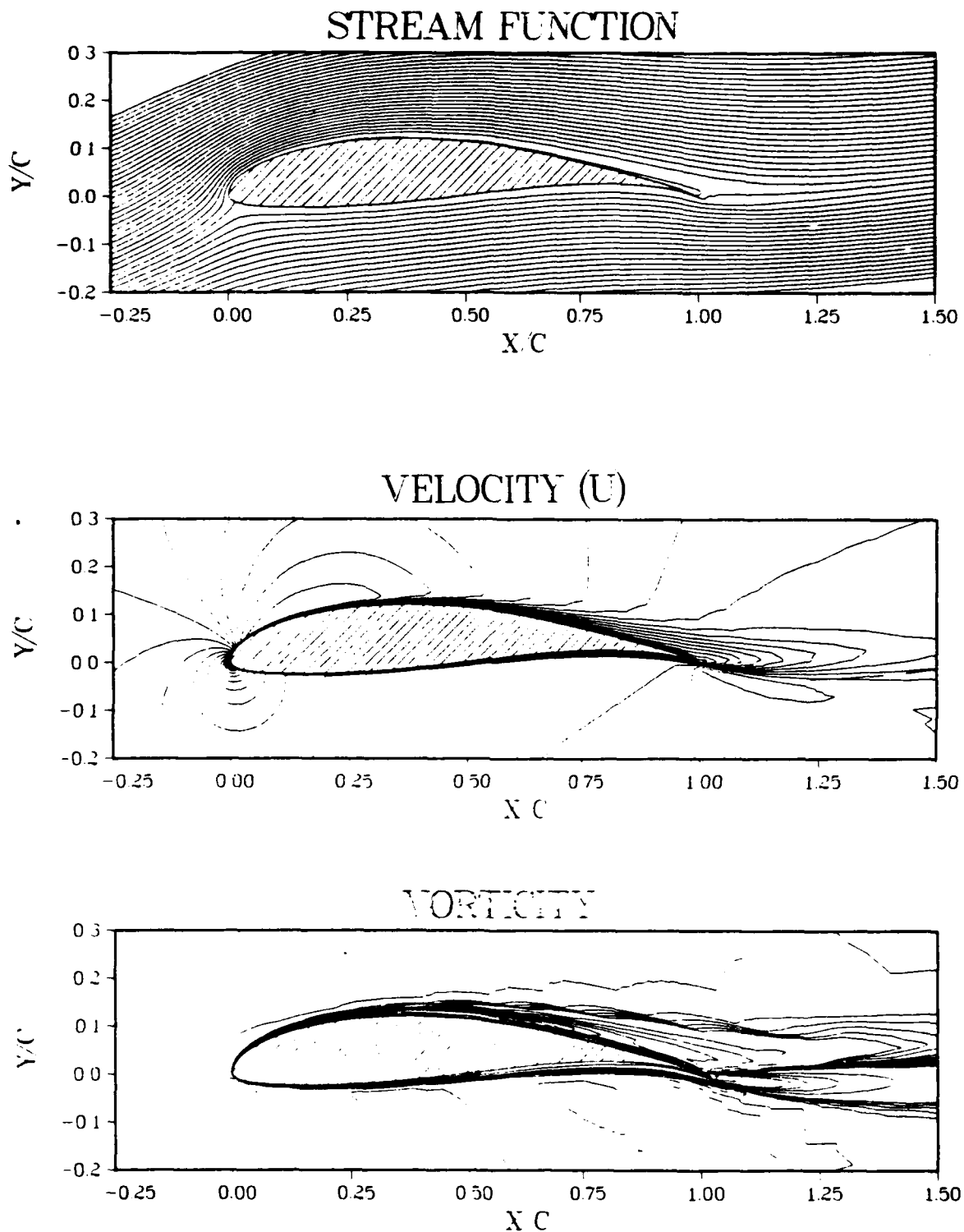


Figure 41 Constant stream function, velocity and vorticity contour plots for Wortman FX 63-137 airfoil, $\alpha = 16^\circ$, $\delta_{1e} = 0^\circ$, $\delta_{te} = 0^\circ$, $Re = 1 \times 10^5$

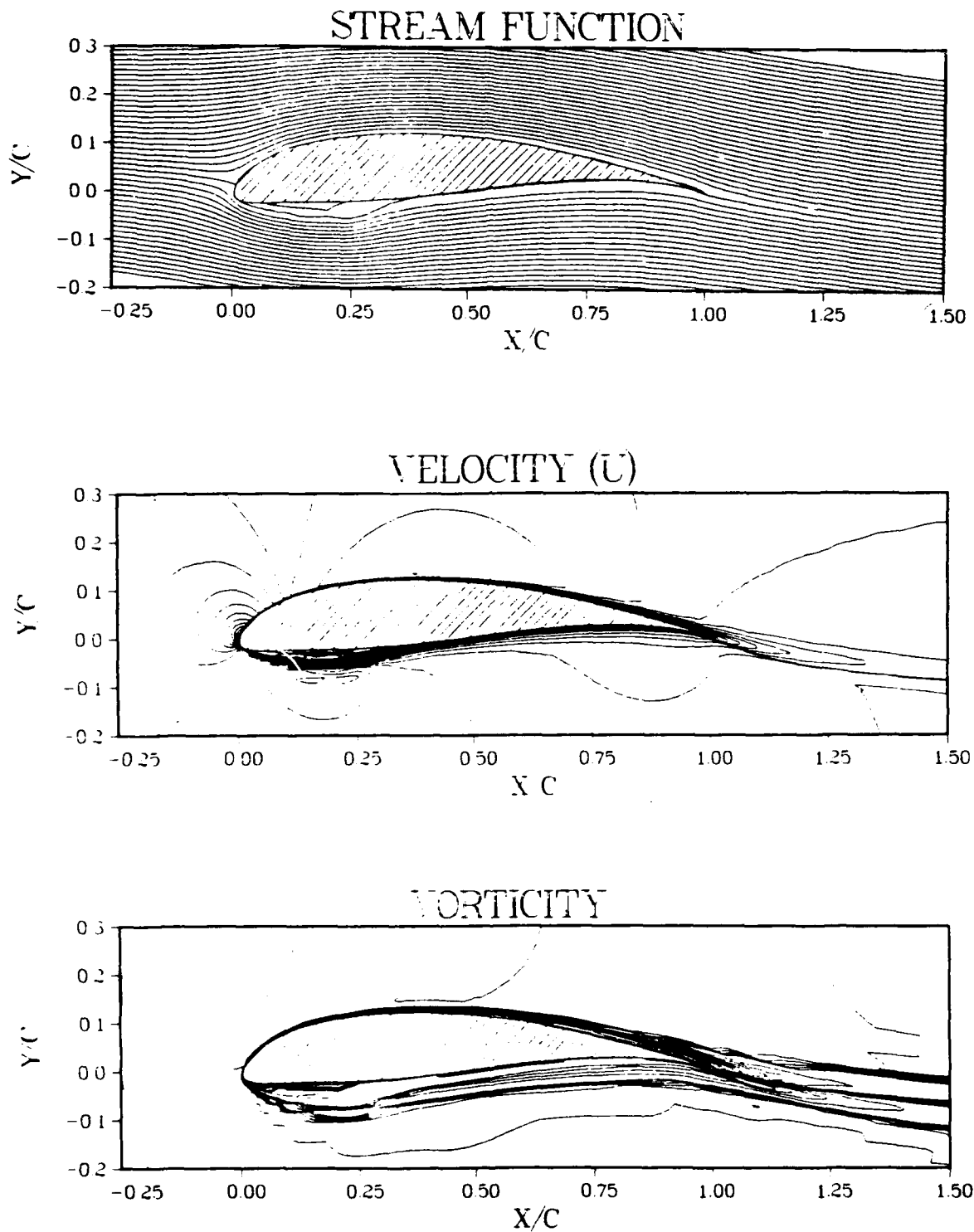


Figure 42 Constant stream function, velocity and vorticity contour plots for Wortman FX 63-137 airfoil, $\alpha = -4^\circ$, $\delta_{le} = 5^\circ$, $\delta_{te} = 0^\circ$, $Re = 1 \times 10^5$

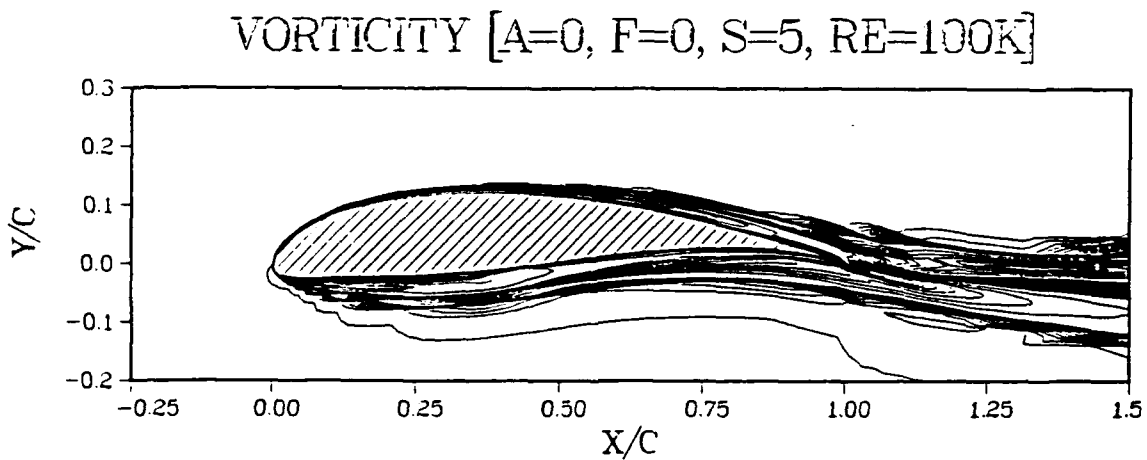
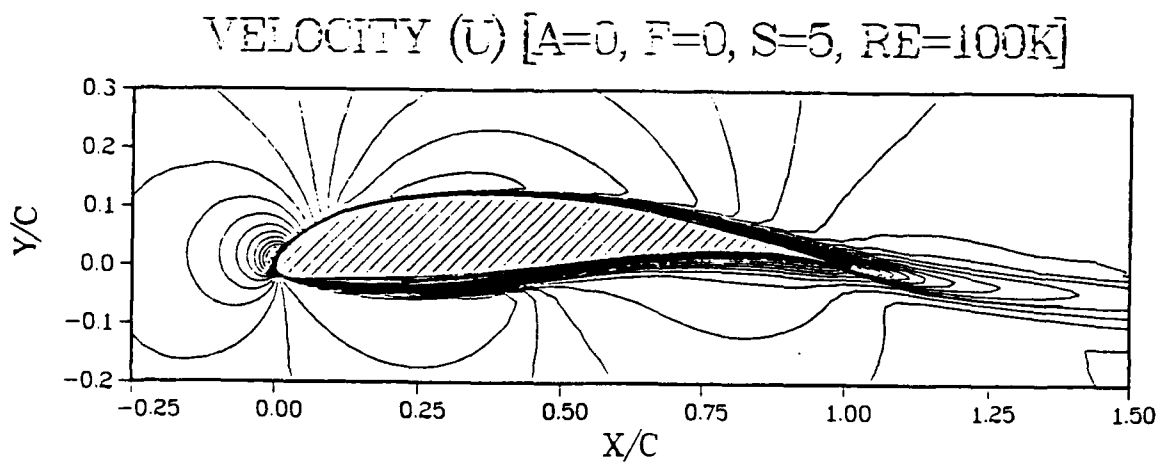
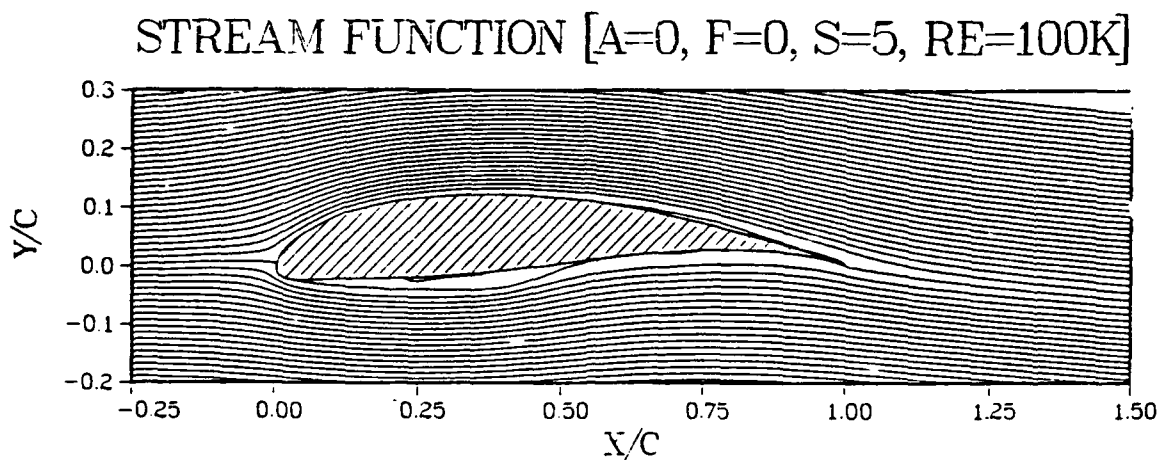


Figure 43 Constant stream function, velocity and vorticity contour plots for Wortman FX 63-137 airfoil, $\alpha = 0^\circ$, $\delta_{1e} = 5^\circ$, $\delta_{2e} = 0^\circ$, $Re = 1 \times 10^5$

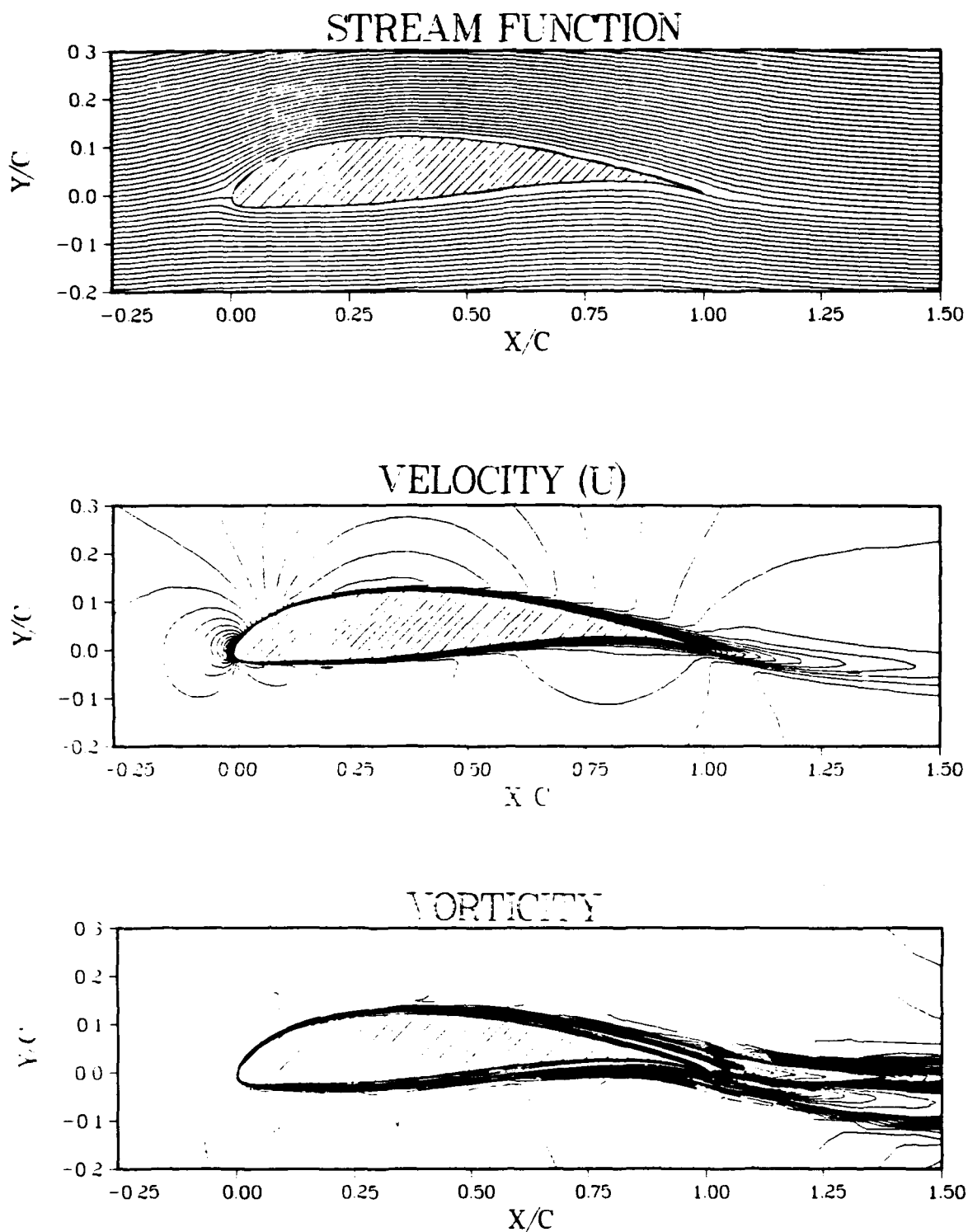


Figure 44 Constant stream function, velocity and vorticity contour plots for Wortman FX 63-137 airfoil, $\alpha = 4^\circ$, $\delta_{le} = 5^\circ$, $\delta_{te} = 0^\circ$, $Re = 1 \times 10^5$

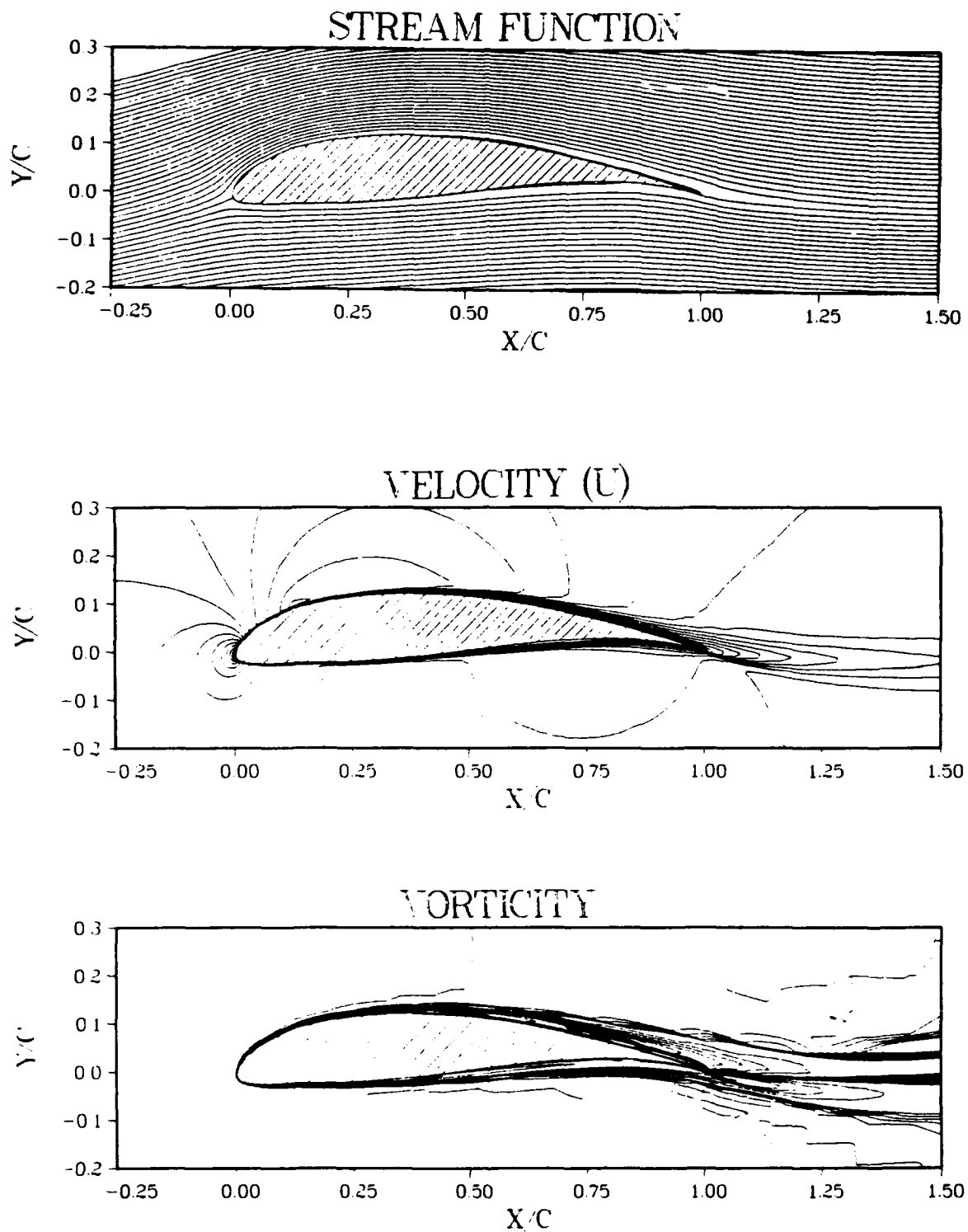


Figure 45 Constant stream function, velocity and vorticity contour plots for Wortman FX 63-137 airfoil, $\alpha = 8^\circ$, $\delta_{1e} = 5^\circ$, $\delta_{2e} = 0^\circ$, $Re = 1 \times 10^5$

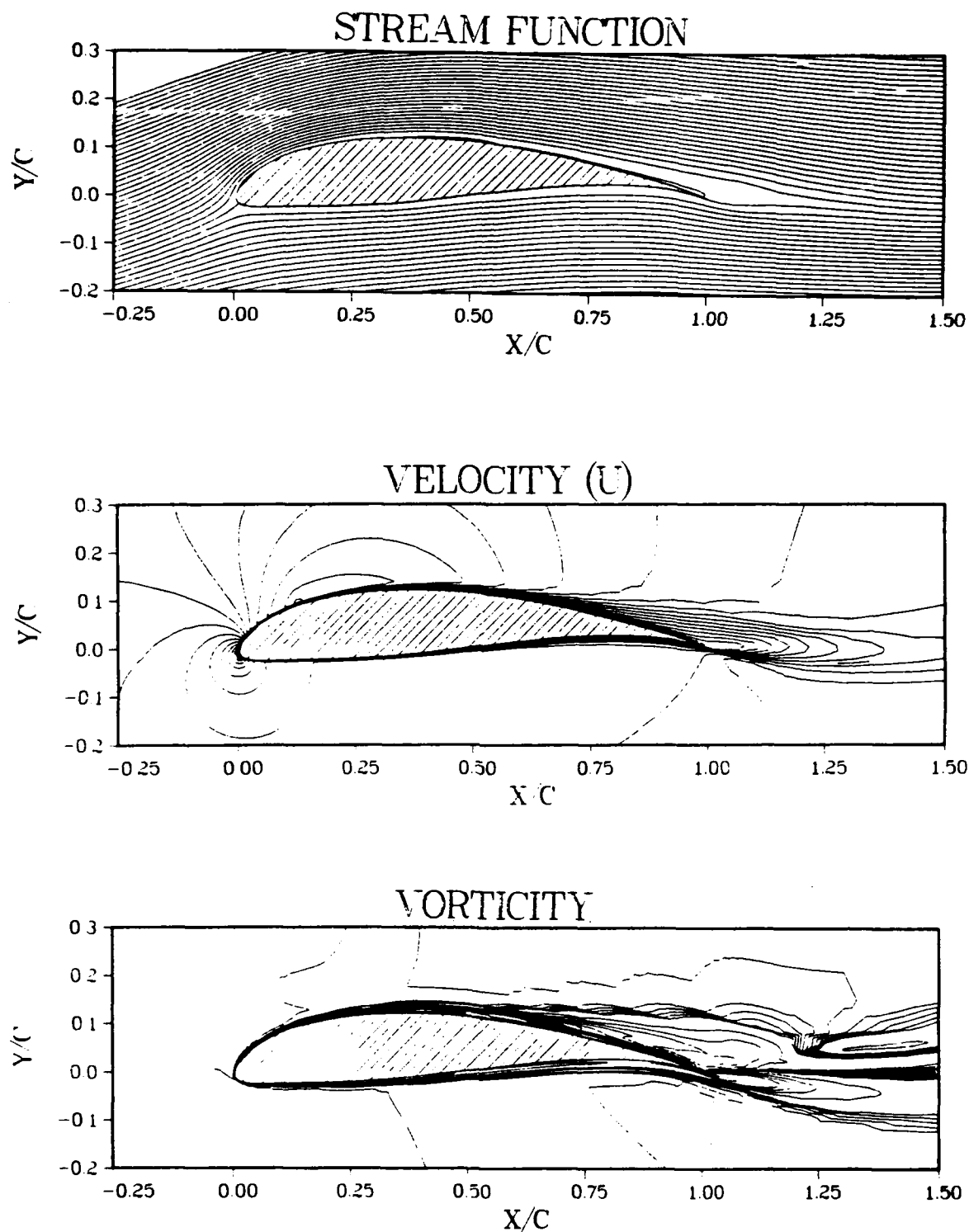


Figure 46 Constant stream function, velocity and vorticity contour plots for Wortman FX 63-137 airfoil, $\alpha = 12^\circ$, $\delta_{1e} = 5^\circ$, $\delta_{te} = 0^\circ$, $Re = 1 \times 10^5$

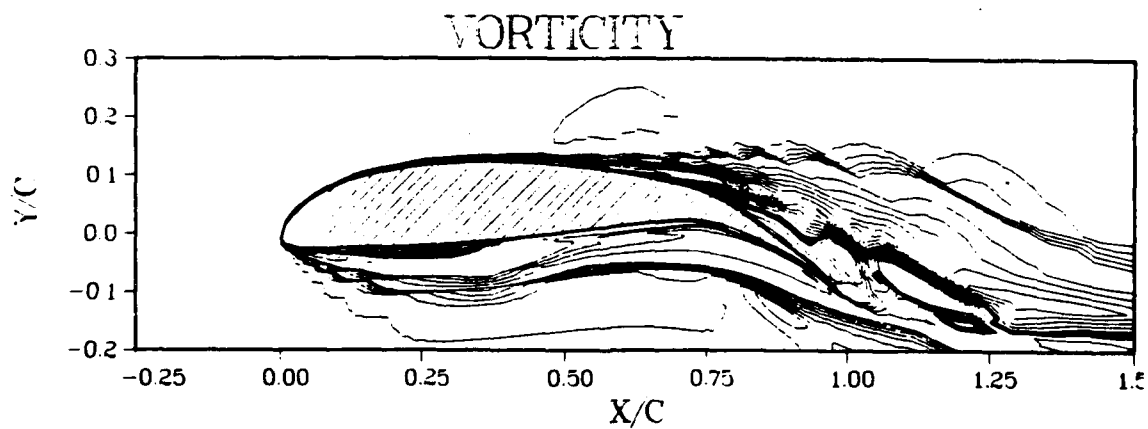
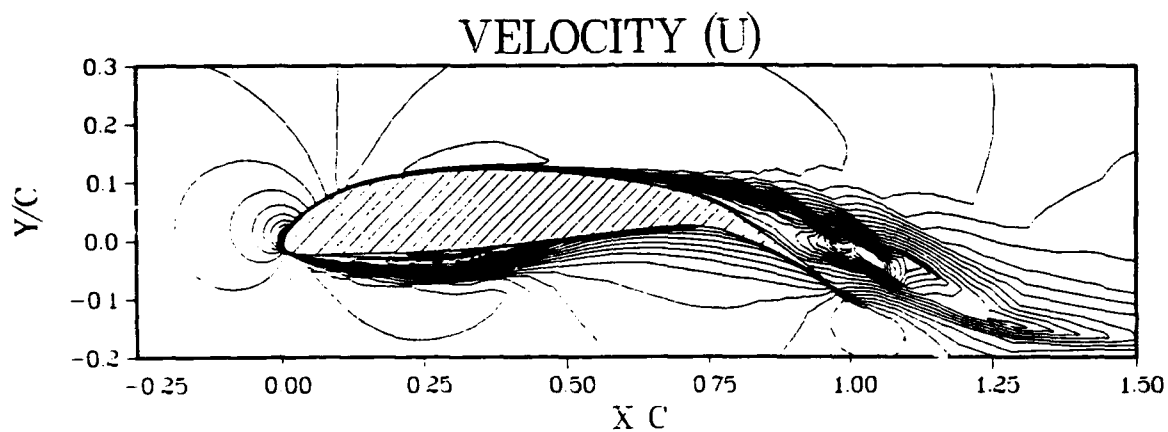
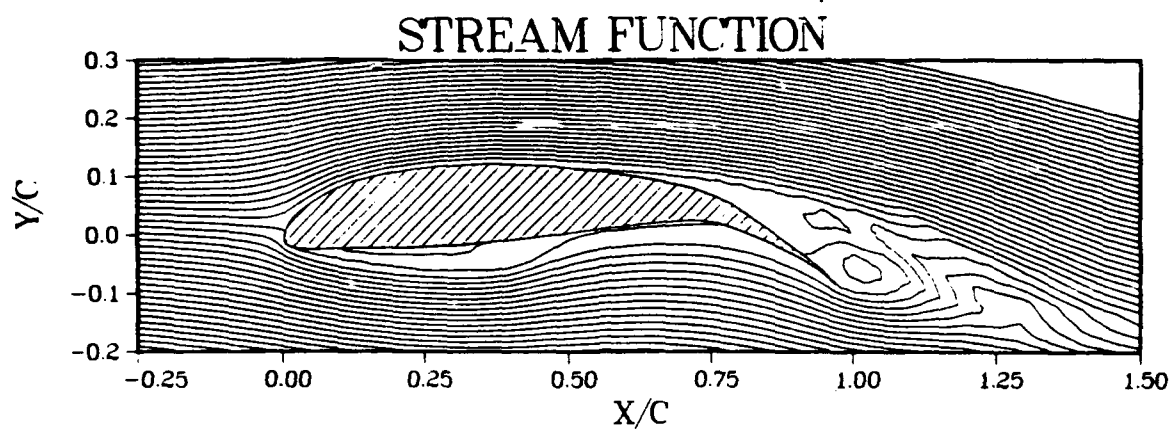


Figure 47 Constant stream function, velocity and vorticity contour plots for Wortman FX 63-137 airfoil, $\alpha = -4^\circ$, $\delta_{1e} = 5^\circ$, $\delta_{te} = 20^\circ$, $Re = 1 \times 10^5$

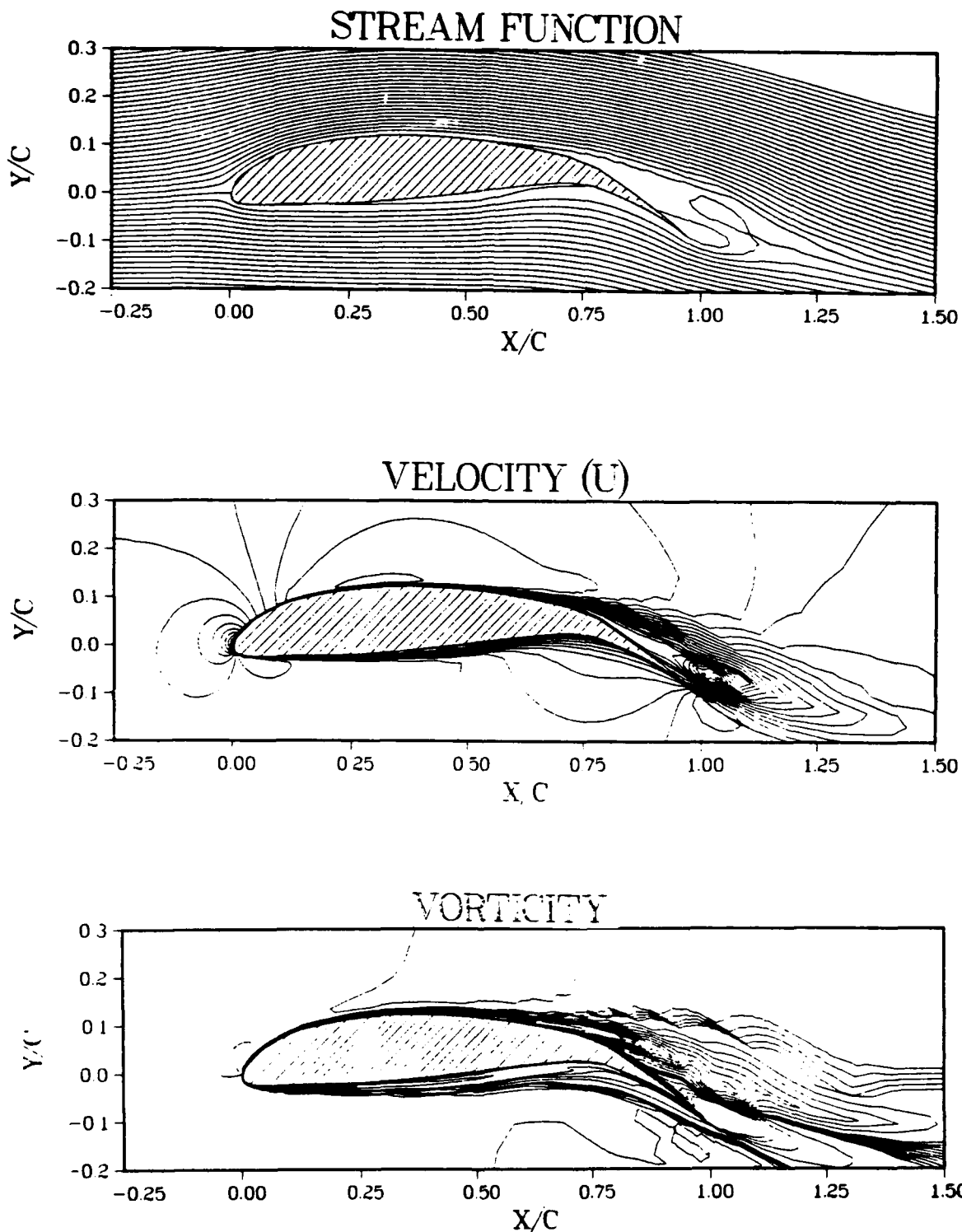


Figure 48 Constant stream function, velocity and vorticity contour plots for Wortman FX 63-137 airfoil, $\alpha = 0^\circ$, $\delta_{1e} = 5^\circ$, $\delta_{te} = 20^\circ$, $Re = 1 \times 10^5$

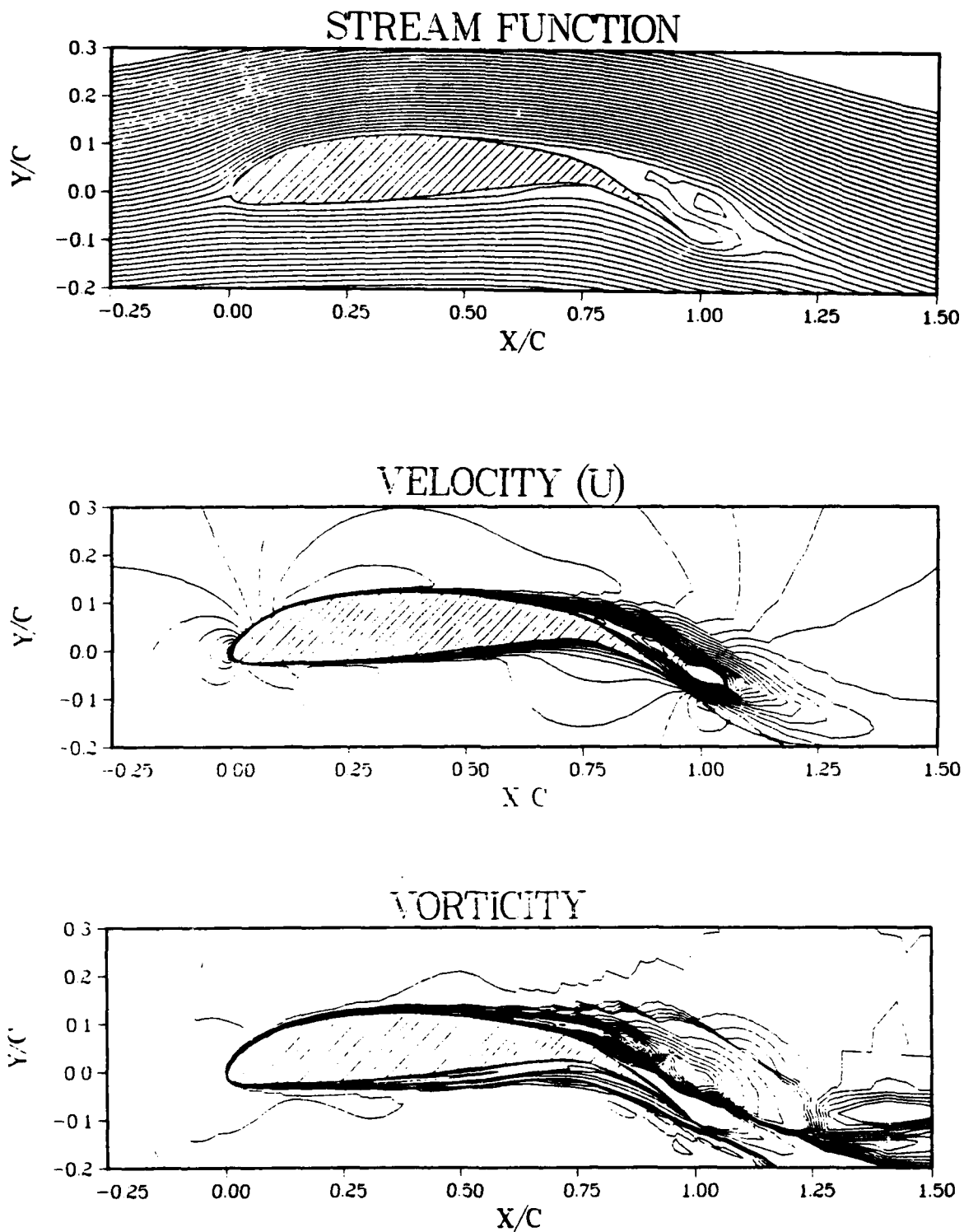


Figure 49 Constant stream function, velocity and vorticity contour plots for Wortman FX 63-137 airfoil, $\alpha = 4^\circ$, $\delta_{1e} = 5^\circ$, $\delta_{2e} = 20^\circ$, $Re = 1 \times 10^5$

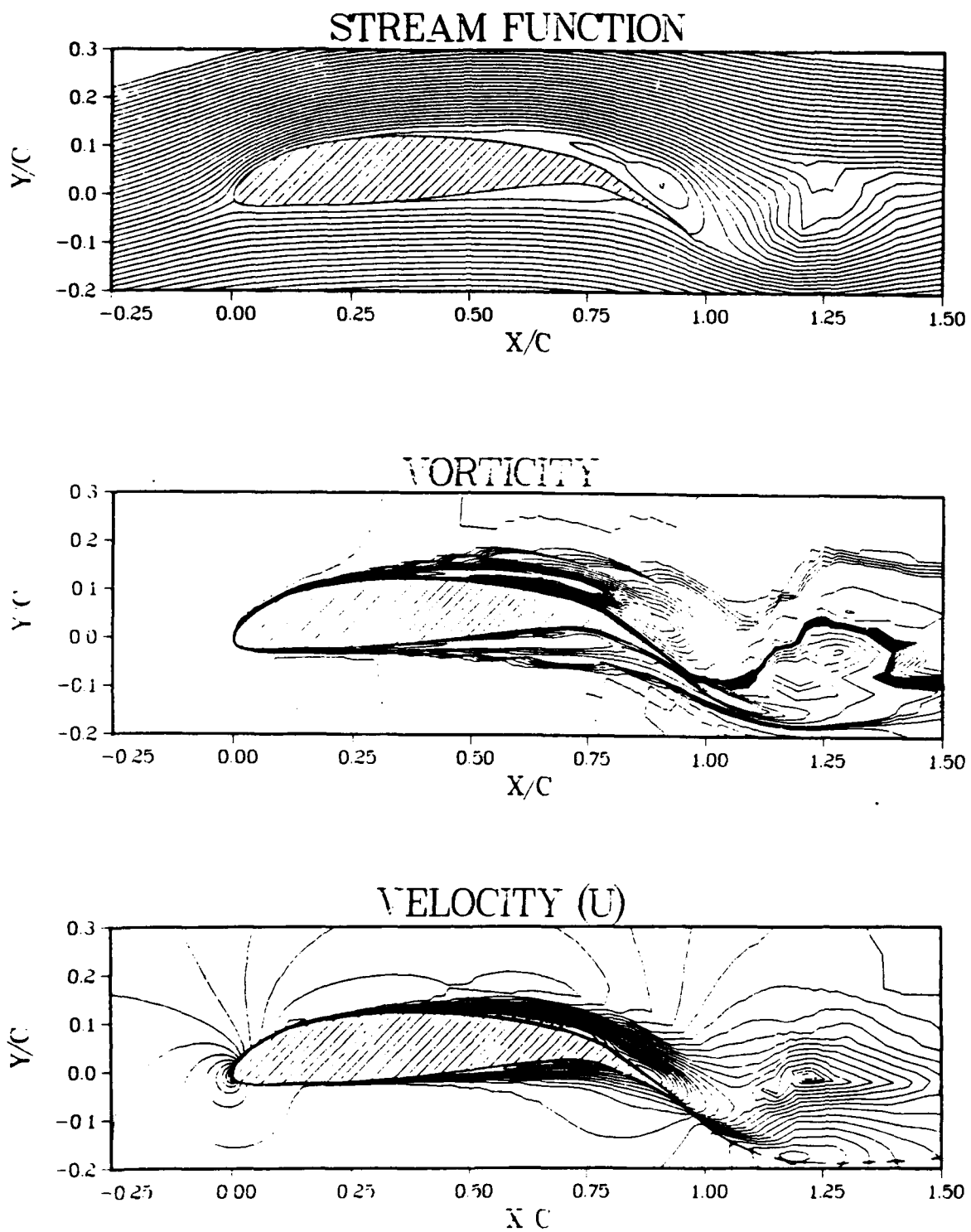


Figure 50 Constant stream function, velocity and vorticity contour plots for Wortman FX 63-137 airfoil, $\alpha = 8^\circ$, $\delta_{1e} = 5^\circ$, $\delta_{te} = 20^\circ$, $Re = 1 \times 10^5$

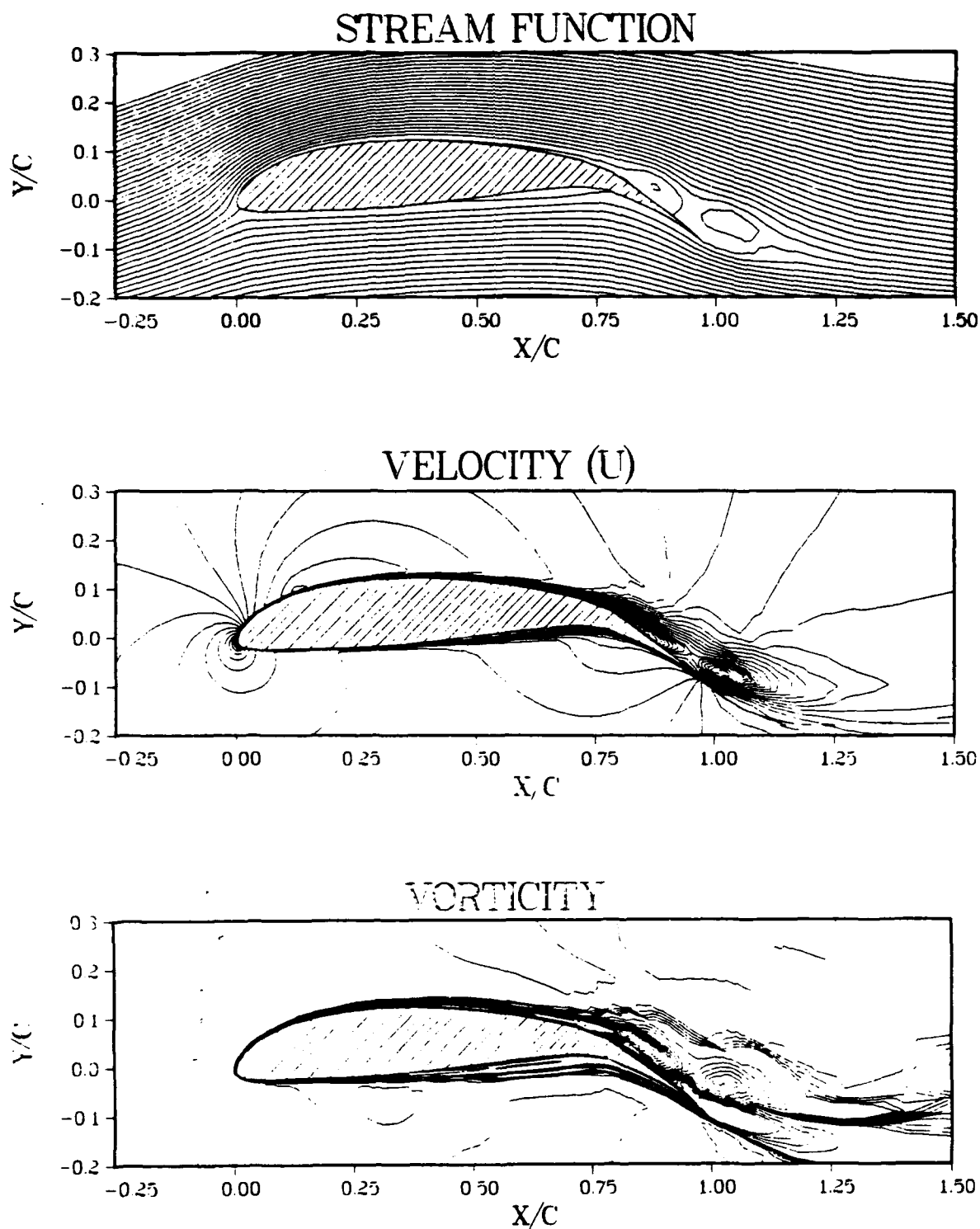


Figure 51 Constant stream function, velocity and vorticity contour plots for Wortman FX 63-137 airfoil, $\alpha = 12^\circ$, $\delta_{1e} = 5^\circ$, $\delta_{te} = 20^\circ$, $Re = 1 \times 10^5$

Appendix I: Variation of Pressure and Skin Friction

Coefficient for Wortman FX 63-137 Airfoil

For all cases considered in this study, the chordwise distribution of skin friction coefficient (C_f) and the pressure coefficient (C_p) on the surface of the Wortman FX 63-137 airfoil has been plotted vs. the chord ratio (x/c). same are attached in this Appendix as Figures 52 through 67.

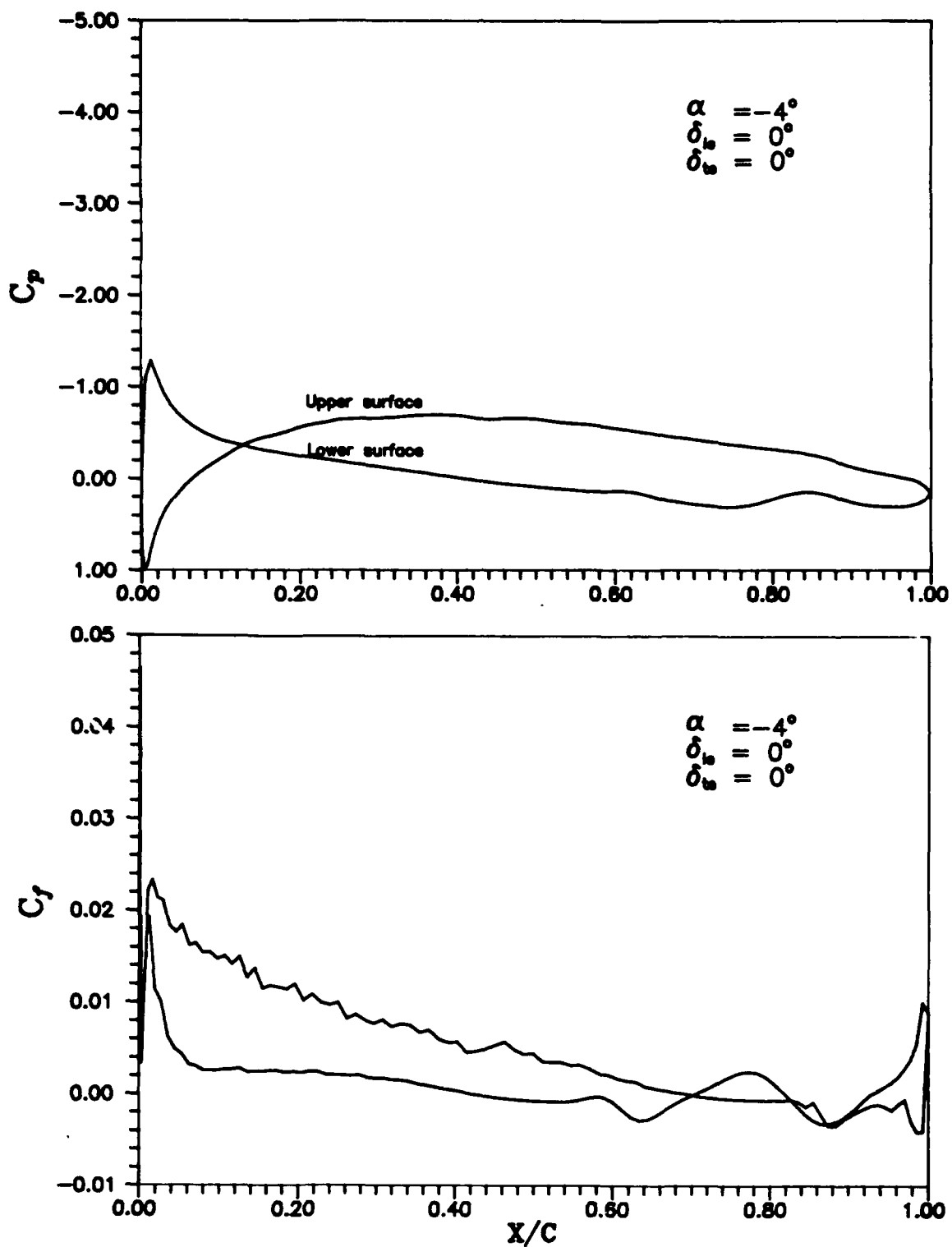


Figure 52 Pressure coefficient (C_p) and skin friction coefficient (C_f) vs. x/c

$\alpha = -4^\circ$, $\delta_{1e} = 0^\circ$, $\delta_{te} = 0^\circ$, $Re = 1 \times 10^5$

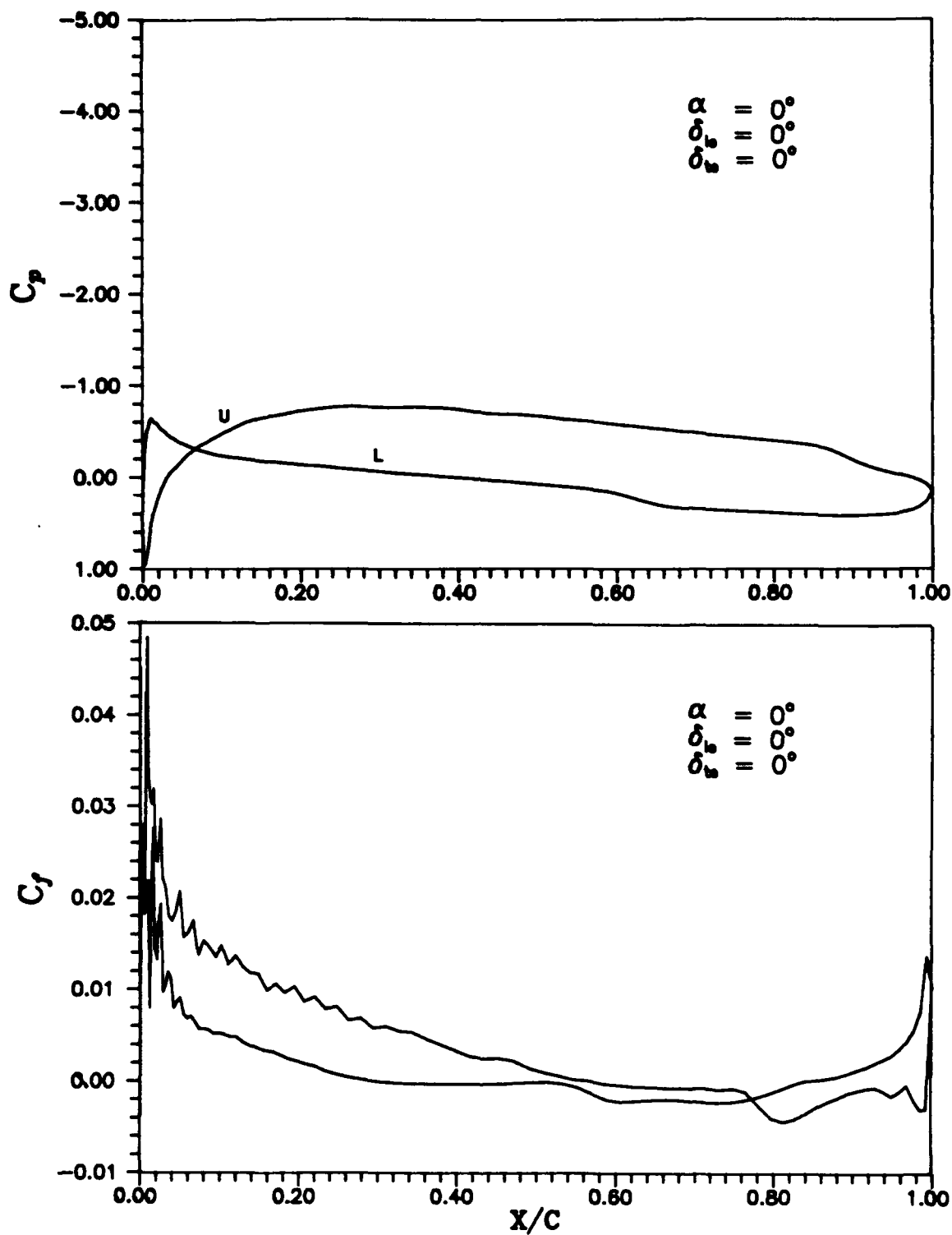


Figure 53 Pressure coefficient (C_p) and skin friction coefficient (C_f) vs. x/c
 $\alpha = 0^\circ$, $\delta_{1e} = 0^\circ$, $\delta_{te} = 0^\circ$, $Re = 1 \times 10^6$

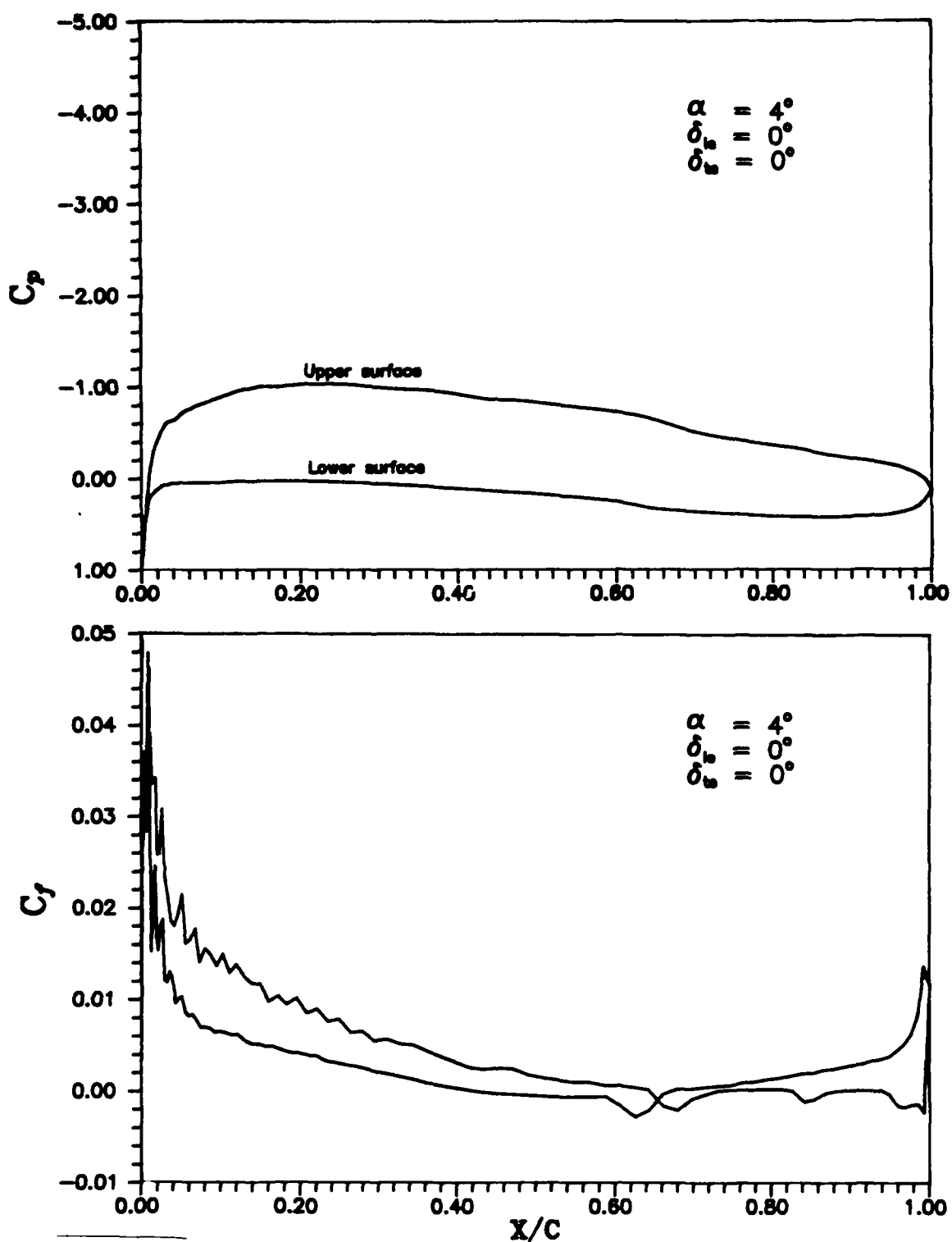


Figure 54 Pressure coefficient (C_p) and skin friction coefficient (C_f) vs. x/c
 $\alpha = 4^\circ$, $\delta_{1e} = 0^\circ$, $\delta_{te} = 0^\circ$, $Re = 1 \times 10^5$

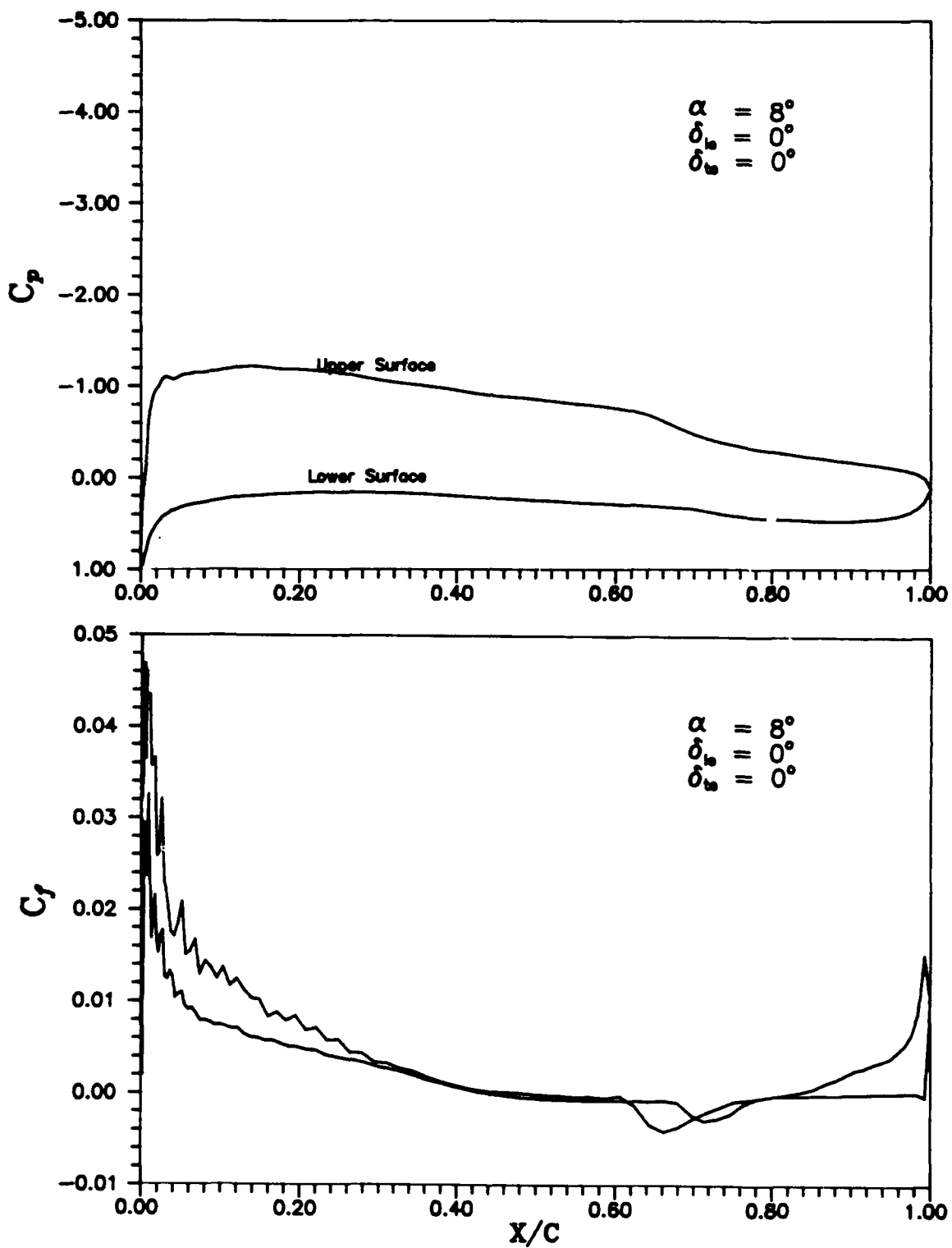


Figure 55 Pressure coefficient (C_p) and skin friction coefficient (C_f) vs. x/c
 $\alpha = 8^\circ$, $\delta_{1e} = 0^\circ$, $\delta_{te} = 0^\circ$, $Re = 1 \times 10^5$

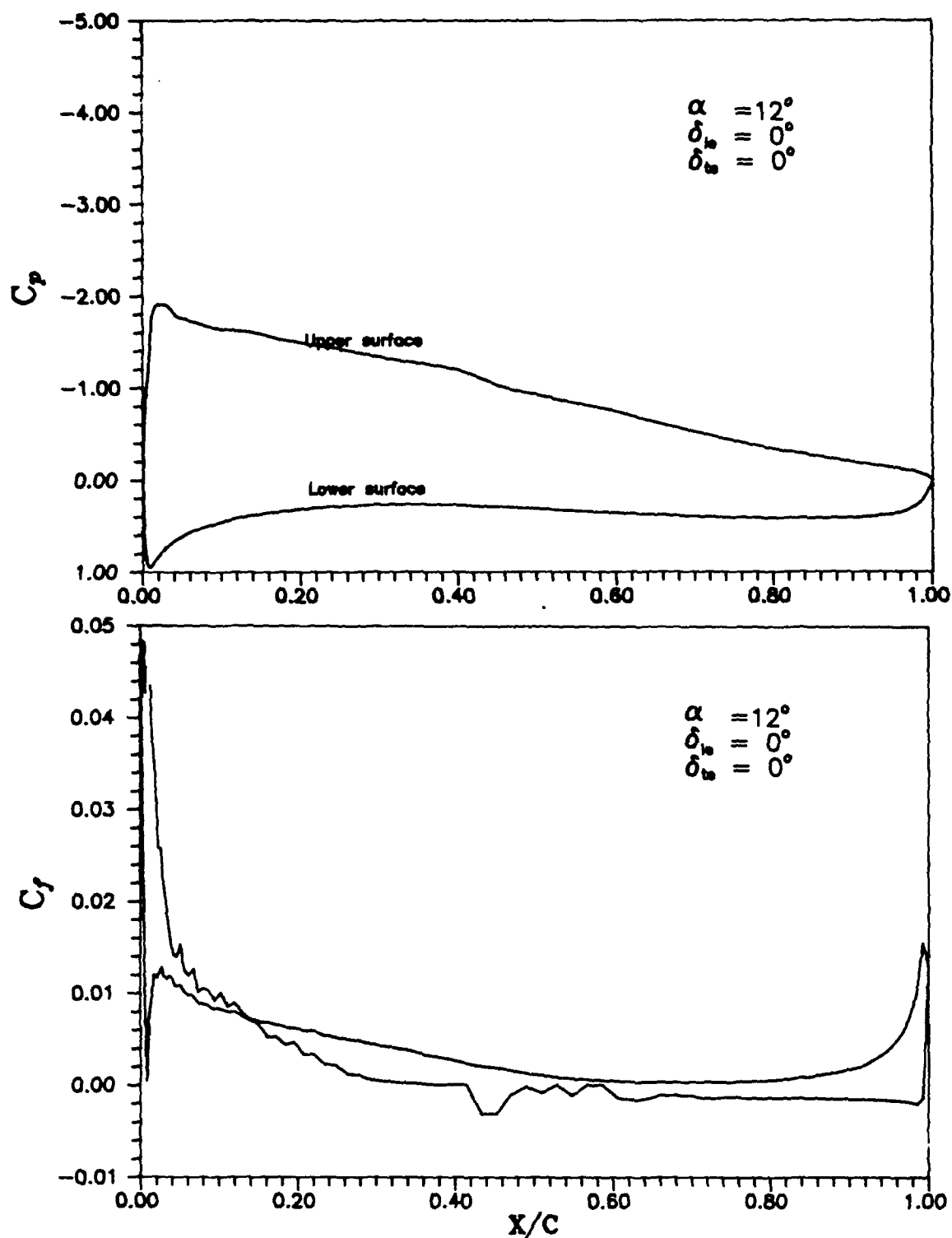


Figure 56 Pressure coefficient (C_p) and skin friction coefficient (C_f) vs. x/c
 $\alpha = 12^\circ$, $\delta_{le} = 0^\circ$, $\delta_{te} = 0^\circ$, $Re = 1 \times 10^6$

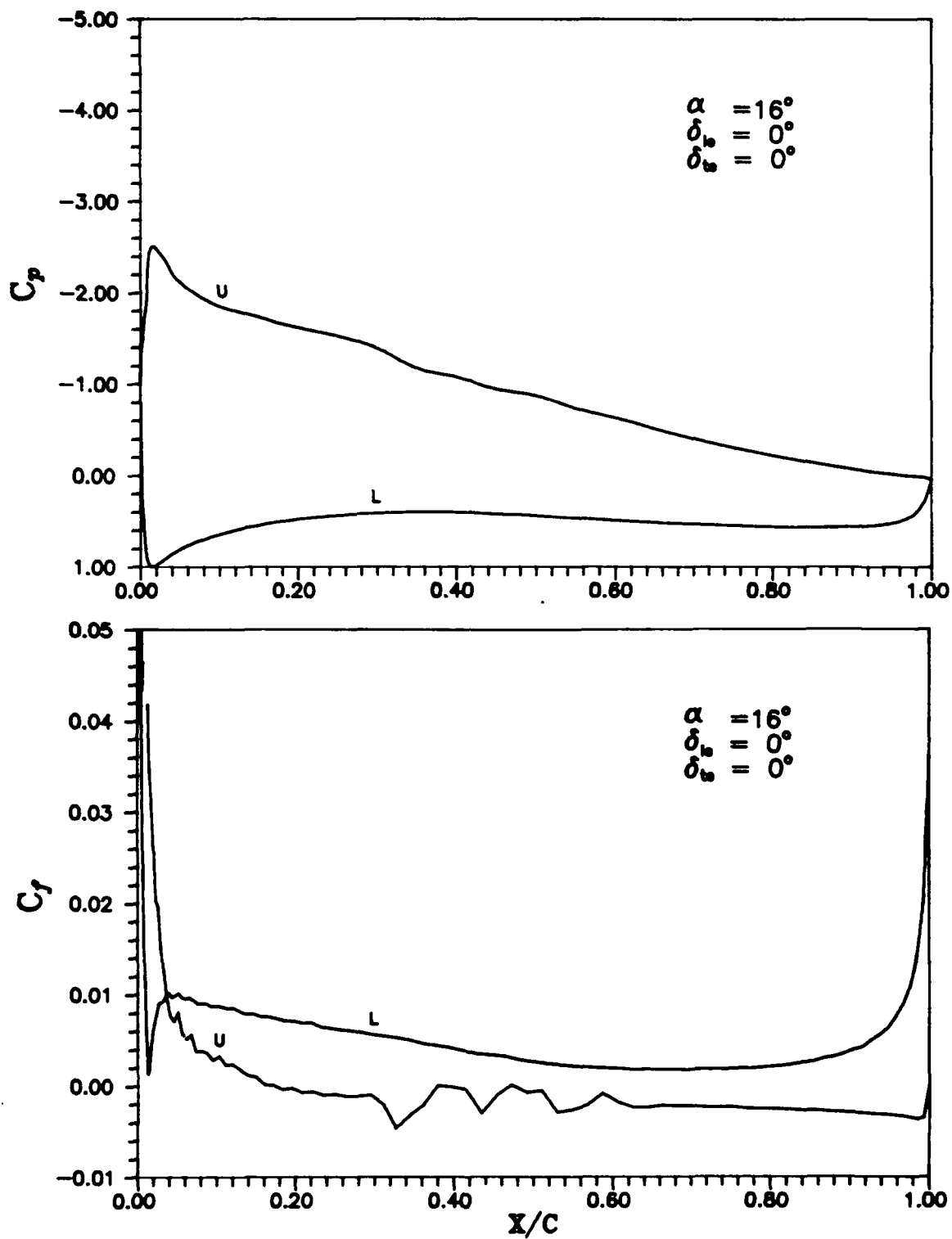


Figure 57 Pressure coefficient (C_p) and skin friction coefficient (C_f) vs. x/c

$\alpha = 16^\circ$, $\delta_{1e} = 0^\circ$, $\delta_{te} = 0^\circ$, $Re = 1 \times 10^5$

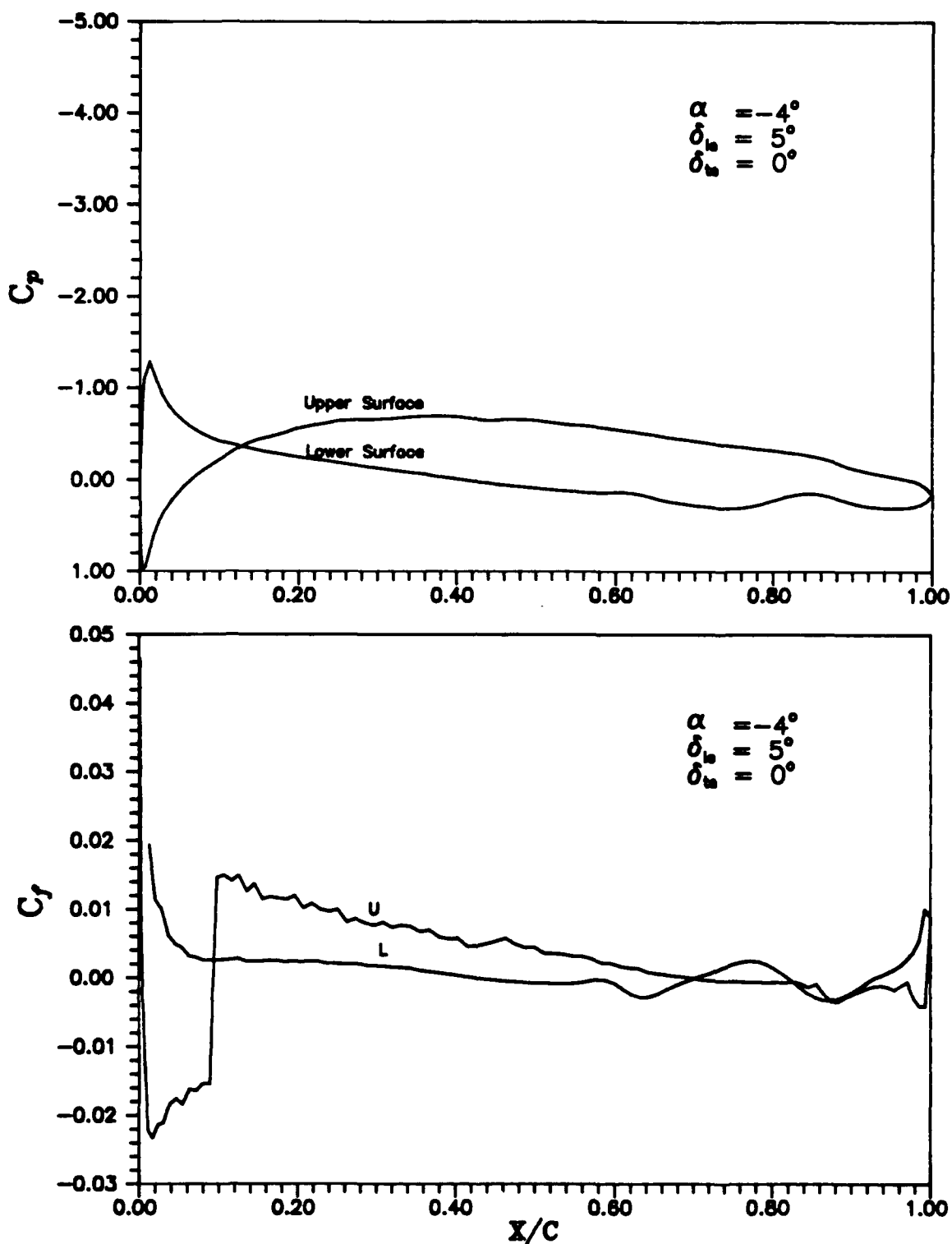


Figure 58 Pressure coefficient (C_p) and skin friction coefficient (C_f) vs. x/c
 $\alpha = -4^\circ$, $\delta_{le} = 5^\circ$, $\delta_{te} = 0^\circ$, $Re = 1 \times 10^5$

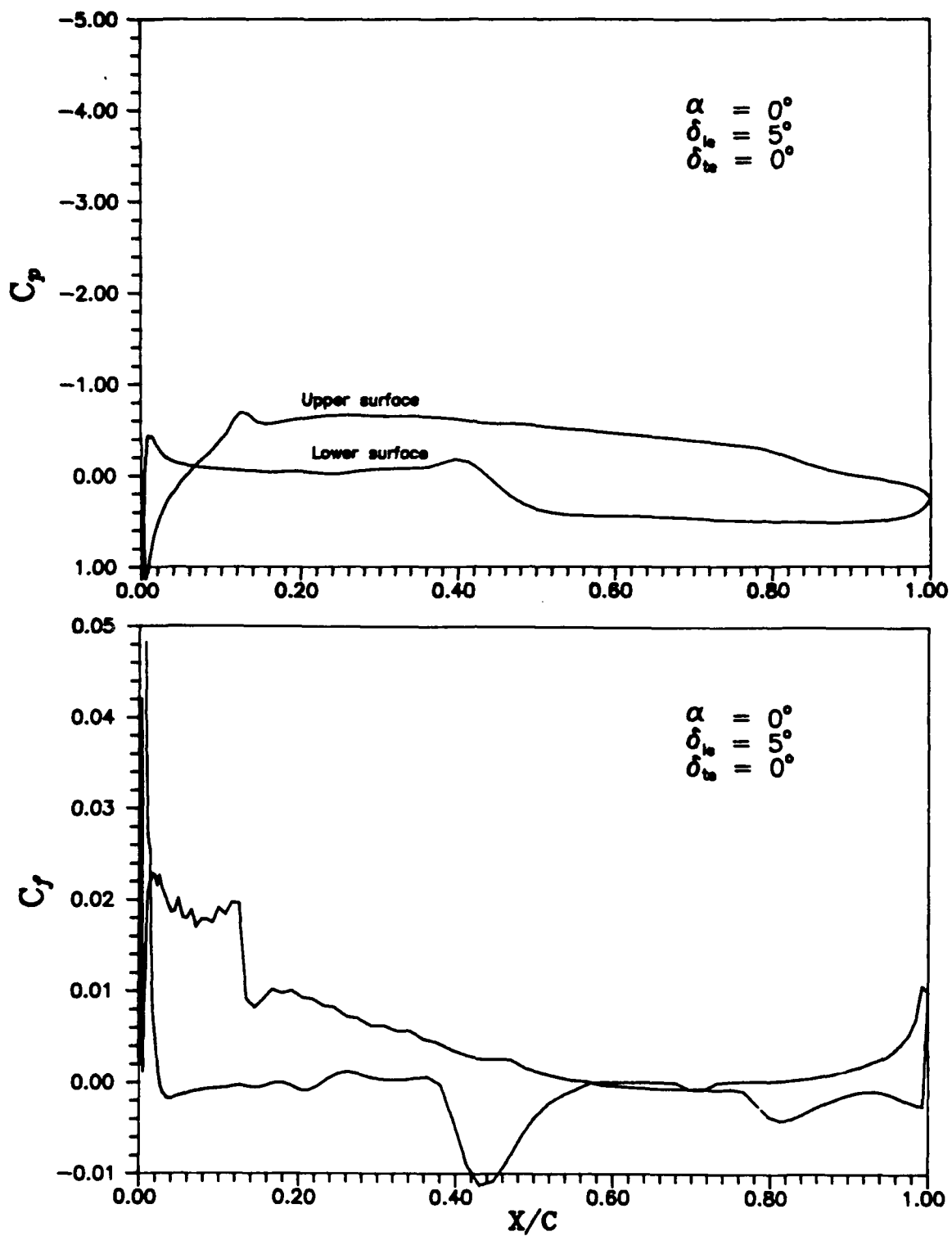


Figure 59 Pressure coefficient (C_p) and skin friction coefficient (C_f) vs. x/c
 $\alpha = 0^\circ$, $\delta_{le} = 5^\circ$, $\delta_{te} = 0^\circ$, $Re = 1 \times 10^5$

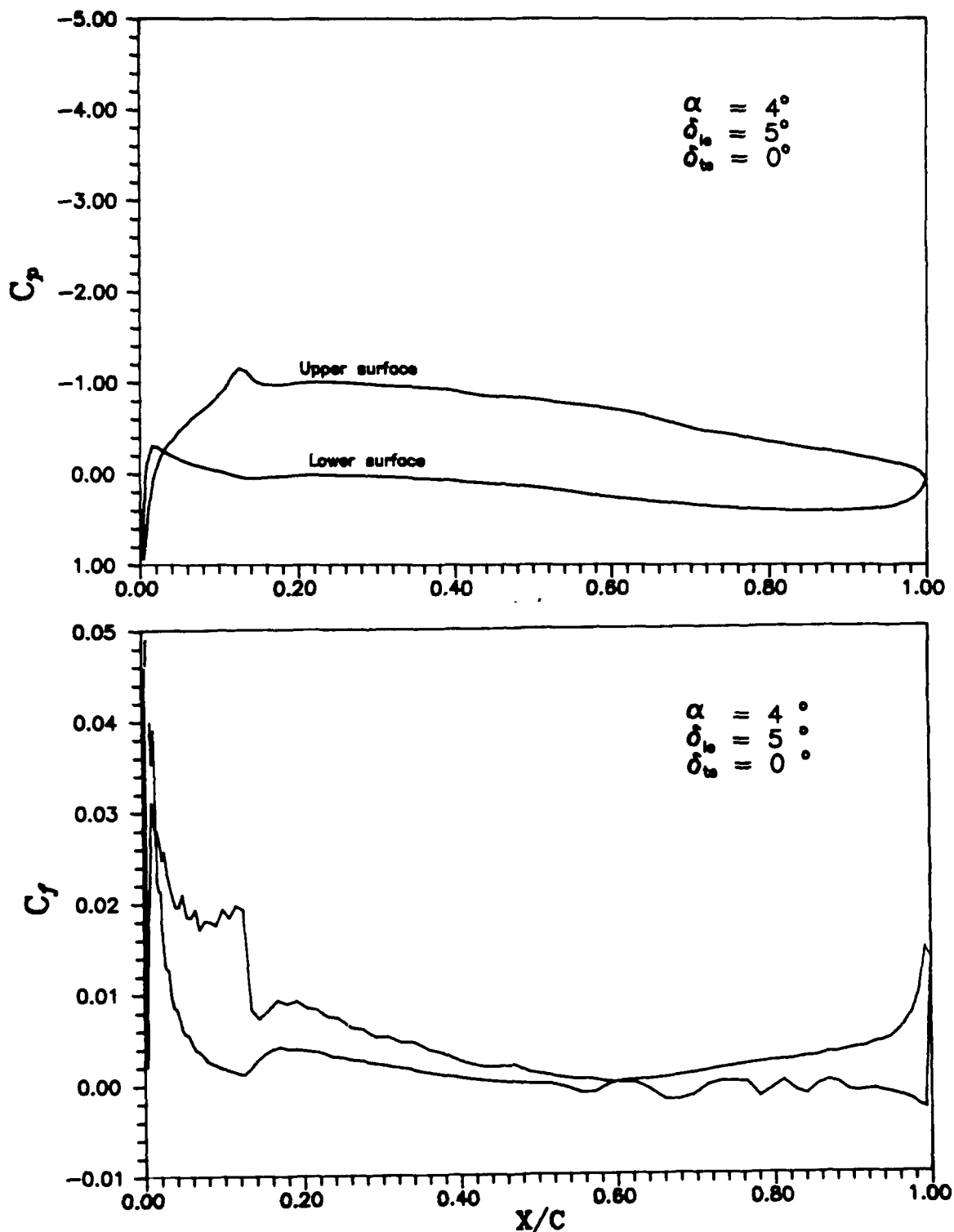


Figure 60 Pressure coefficient (C_p) and skin friction coefficient (C_f) vs. x/c
 $\alpha = 4^\circ$, $\delta_{le} = 5^\circ$, $\delta_{te} = 0^\circ$, $Re = 1 \times 10^5$

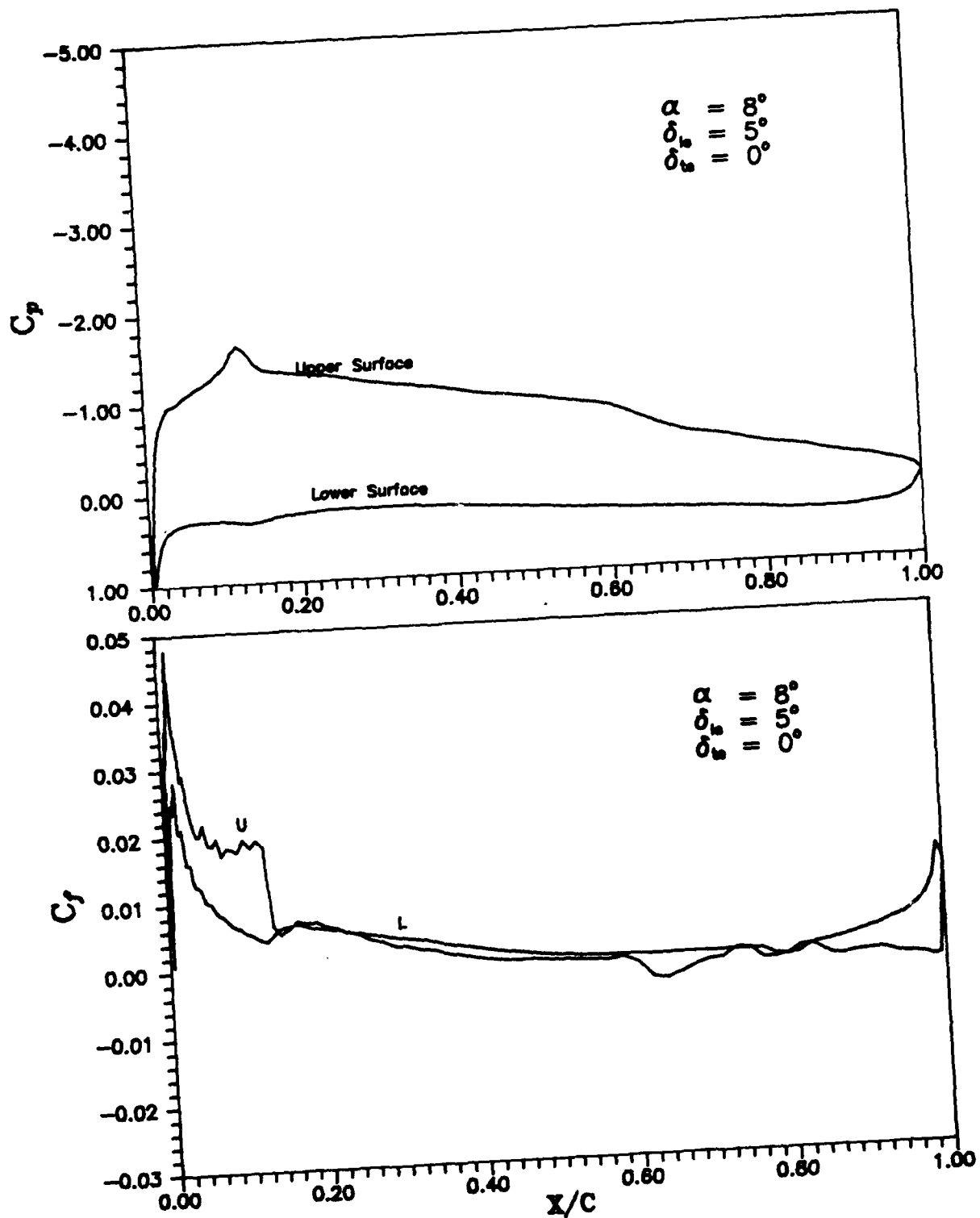


Figure 61 Pressure coefficient (C_p) and skin friction coefficient (C_f) vs. x/c
 $\alpha = 8^\circ$, $\delta_{le} = 5^\circ$, $\delta_{te} = 0^\circ$, $Re = 1 \times 10^5$

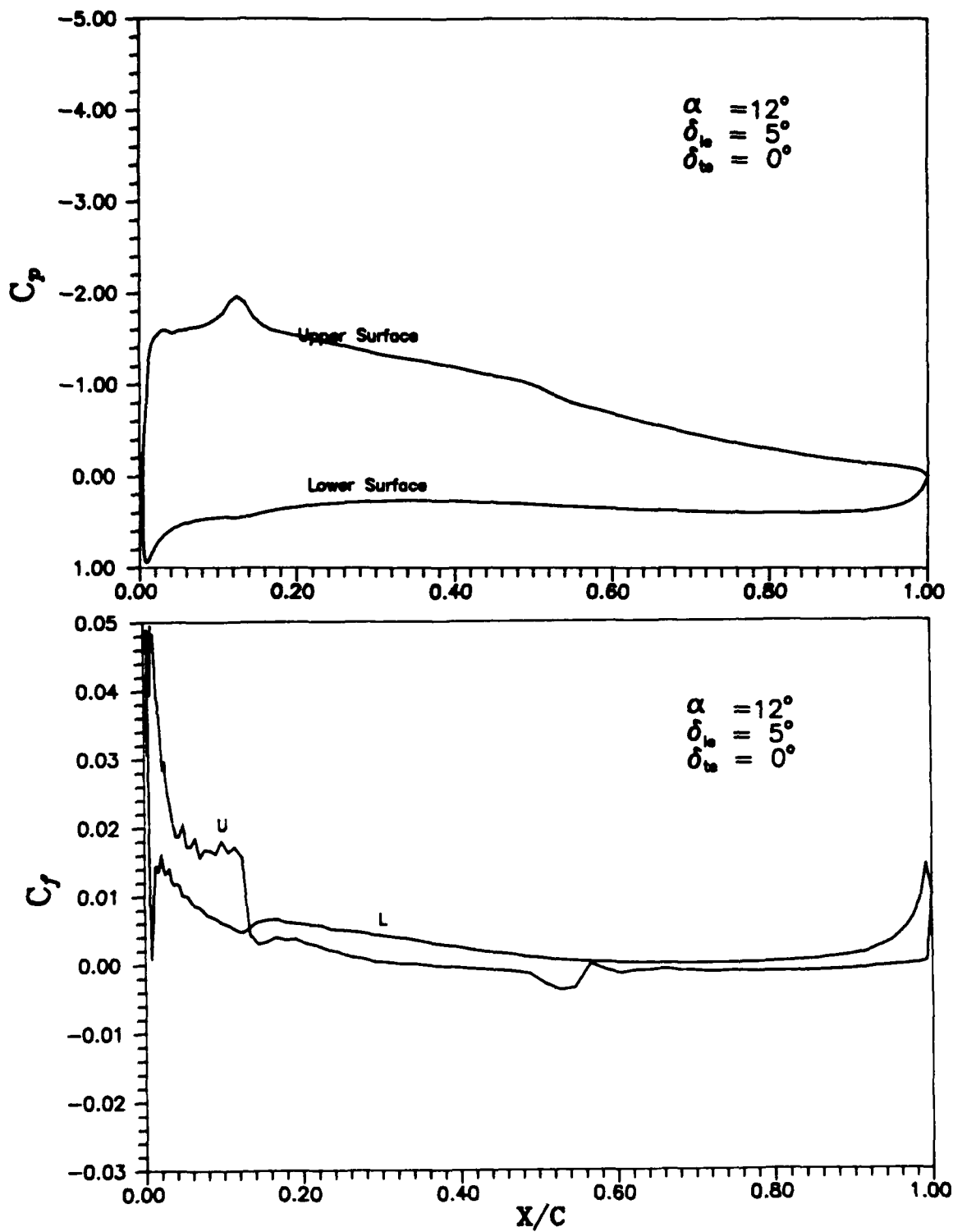


Figure 62 Pressure coefficient (C_p) and skin friction coefficient (C_f) vs. x/c
 $\alpha = 12^\circ$, $\delta_{1e} = 5^\circ$, $\delta_{te} = 0^\circ$, $Re = 1 \times 10^5$

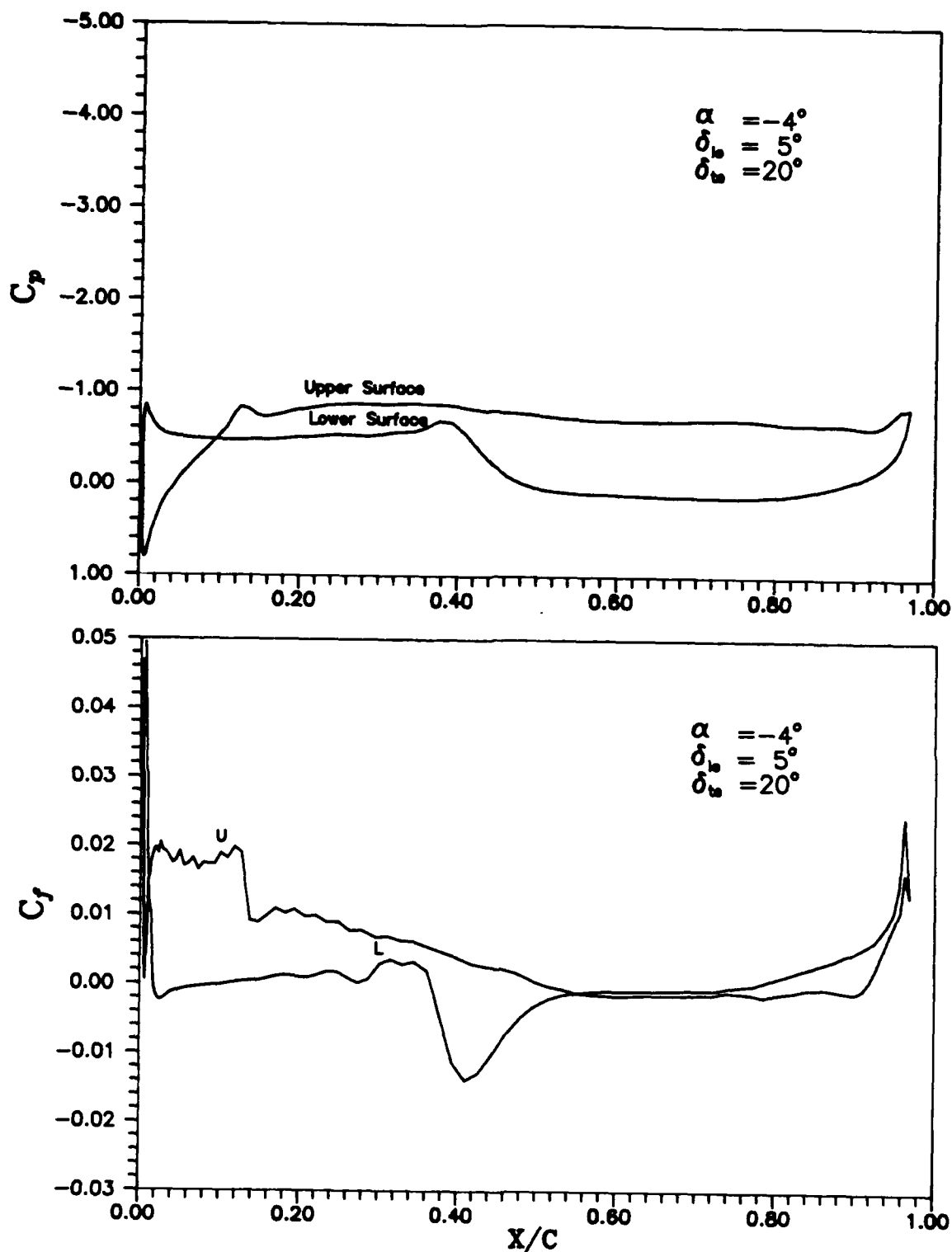


Figure 63 Pressure coefficient (C_p) and skin friction coefficient (C_f) vs. x/c
 $\alpha = -4^\circ$, $\delta_{le} = 5^\circ$, $\delta_{te} = 20^\circ$, $Re = 1 \times 10^5$

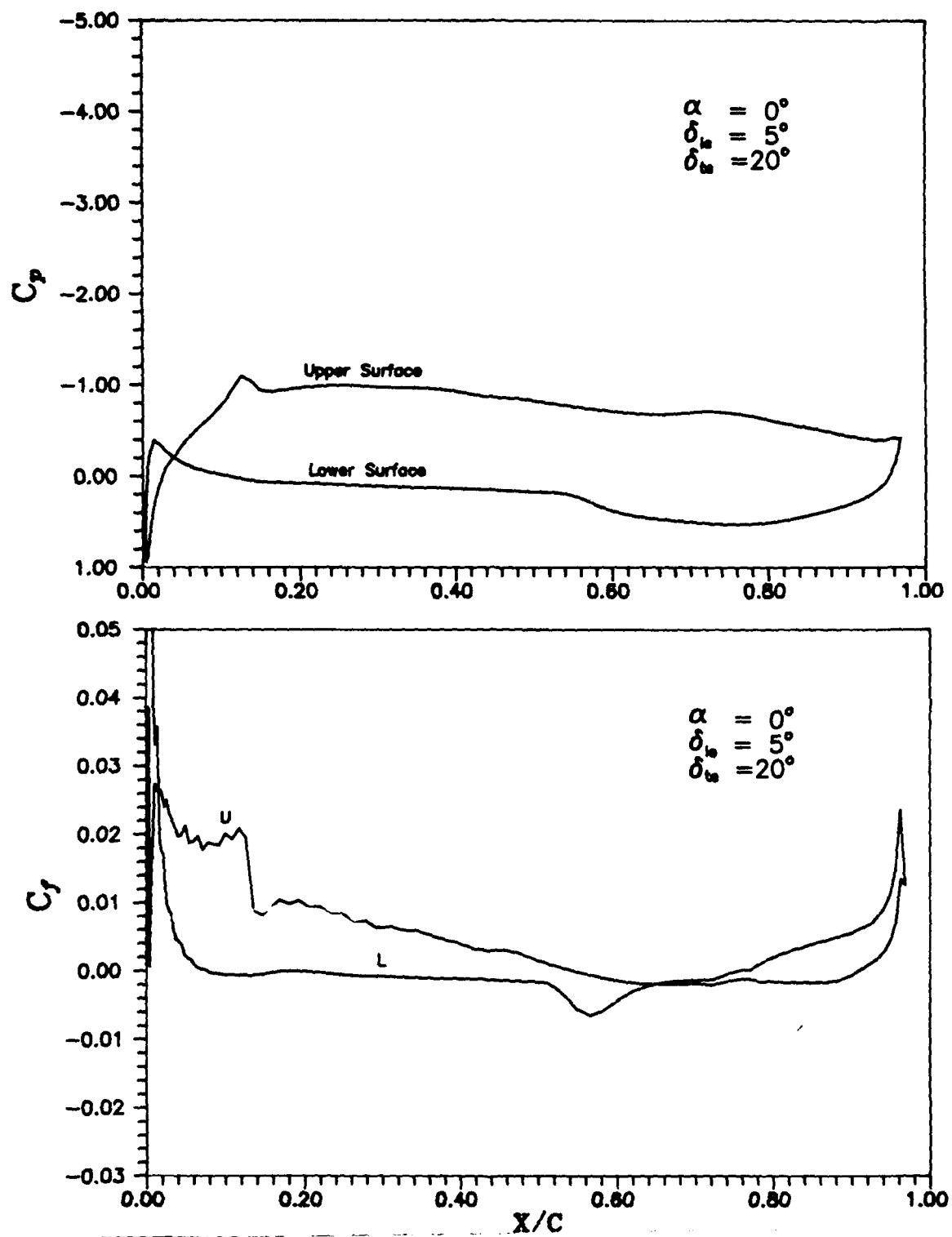


Figure 64 Pressure coefficient (C_p) and skin friction coefficient (C_f) vs. x/c
 $\alpha = 0^\circ$, $\delta_{le} = 5^\circ$, $\delta_{te} = 20^\circ$, $Re = 1 \times 10^5$

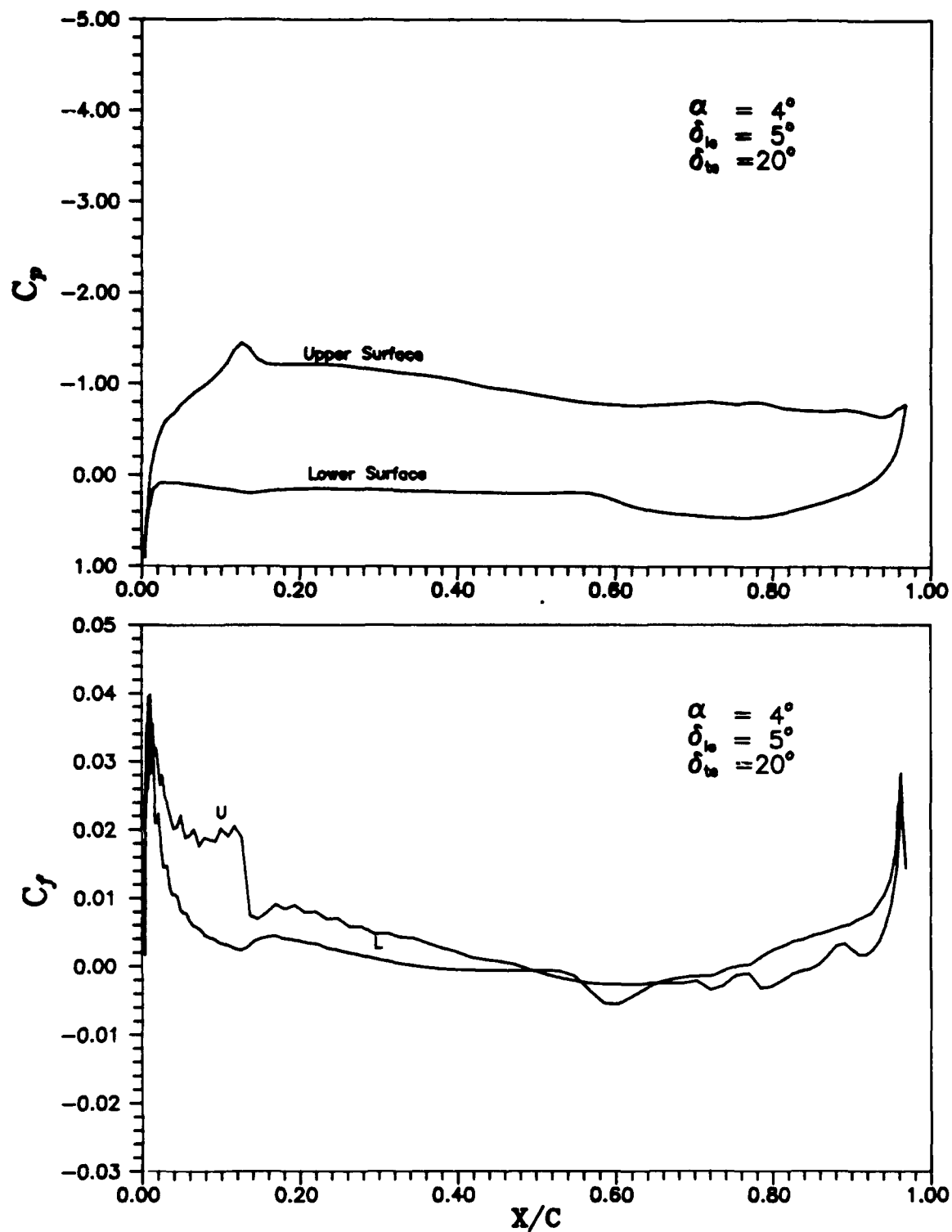


Figure 65 Pressure coefficient (C_p) and skin friction coefficient (C_f) vs. x/c
 $\alpha = 4^\circ$, $\delta_{le} = 5^\circ$, $\delta_{te} = 20^\circ$, $Re = 1 \times 10^5$

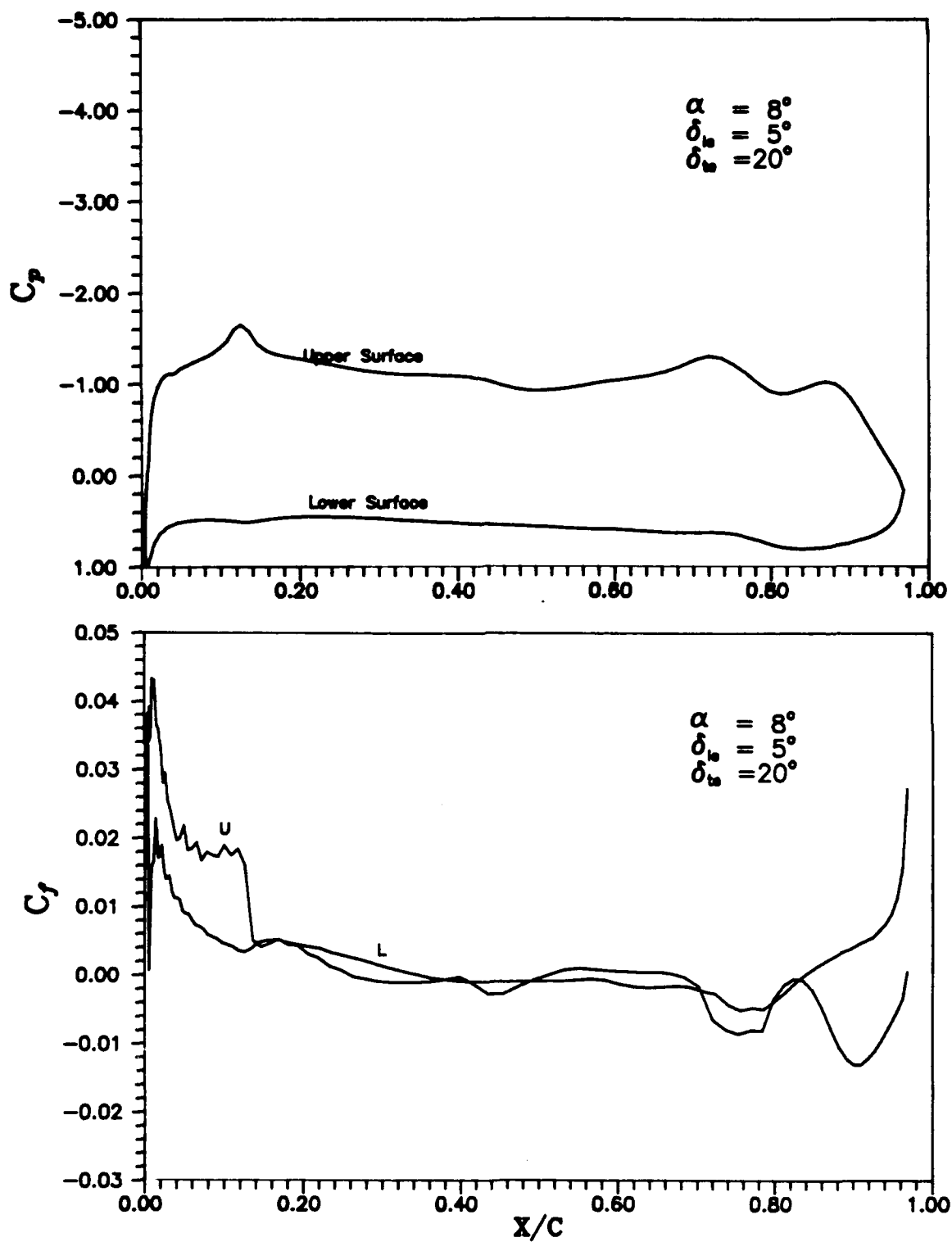


Figure 66 Pressure coefficient (C_p) and skin friction coefficient (C_f) vs. x/c
 $\alpha = 8^\circ$, $\delta_{le} = 5^\circ$, $\delta_{te} = 20^\circ$, $Re = 1 \times 10^5$

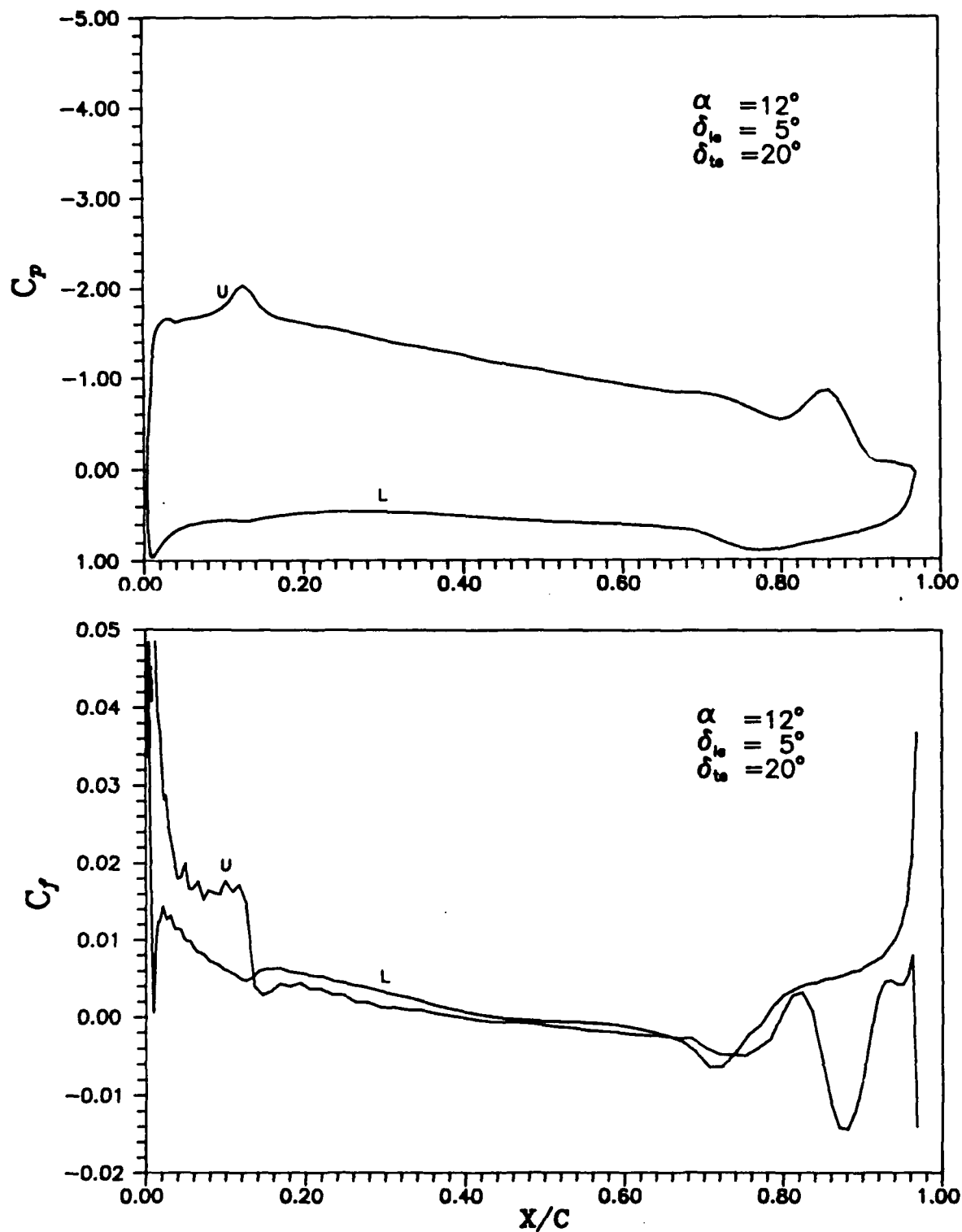


Figure 67 Pressure coefficient (C_p) and skin friction coefficient (C_f) vs. x/c
 $\alpha = 12^\circ$, $\delta_{le} = 5^\circ$, $\delta_{te} = 20^\circ$, $Re = 1 \times 10^5$

Bibliography

1. Amdahl, David, Lt., Aero Methods Group, Personal Communications, AFWAL/FIMM, WPAFB, Ohio, July-November 1988.
2. Anderson, John c. and others. Computational Fluid Mechanics and Heat Transfer. New York: Hemisphere Publishing Corp., 1984.
3. Arena, A.V. and Mueller, T.J., "On the Laminar Separation, Transition and Turbulent Reattachment of Low Reynolds Number Flows near the Leading Edge of Airfoils", AIAA Paper 79-0004, 1979.
4. Baldwin, B.S. and Lomax, H. "Thin Layer Approximation and Algebraic Model for Separated Turbulent Flows", AIAA 16th Aerospace Sciences Meeting. January 1978. AIAA 78-257.
5. Bastedo, W.G., Mueller, T.J., "Spanwise Variation of Laminar Separation Bubbles on Wings at Low Reynolds Numbers", Journal of Aircraft Vol. 23, No. 9, September 1986.
6. Boyles, Paul D., "Navier-Stokes Solution for a NACA 12 Airfoil with Mass Flux (Fan)", Masters Thesis, AFIT/GAE/AA/88D-02, Air Force Institute of Technology, WPAFB, Ohio, 1988.
7. Brendel, M. and Mueller, T.J., "Boundary-Layer Measurements on an Airfoil at Low Reynolds Numbers", Journal of Aircraft, Vol. 25, No. 7, July 1988, pages 612-617.
8. Cebeci, Tuncer, "The Calculation of Flow Iced Airfoils", AIAA 26th Aerospace Sciences Meeting, Reno, Nevada, January 1988, AIAA-88-0112.
9. Cebeci, Tuncer and Bradshaw, Peter. Physical and Computational Aspects of Convective Heat Transfer. New York: Springer-verlag Inc., 1984.
10. Cebeci, Tuncer and Smith, A.M.O., Analysis of Turbulent Boundary Layers. Orlando: Academic Press Inc., 1974.
11. Halim, A.A.M., "A Global Marching Technique for the Prediction of Separated Flows Over Arbitrary Airfoils", AIAA Journal, Vol. 25, No. 9, September 1987.

12. Karamcheti, Krishnamurti. Principles of Ideal Fluid Aerodynamics. Malabar: Robert E. Kreiger Publishing Company, Inc., 1980.
13. Kinsey, Don W. and Barth, Timothy J., "Description of a Hyperbolic Grid Generation Procedure for Arbitrary Two-Dimensional bodies", AFWAL-TM-84-FIMM. WPAFB, Ohio, July 1984.
14. McCormick, B.W., Aerodynamics, Aeronautics, and Flight Mechanics, New York: John Wiley and Sons, 1979.
15. Mehta, U., Chang, K.C. and Cebeci, T., "Relative advantages of Thin-Layer Navier Stokes and interactive Boundary-Layer Procedures", NASA Technical Memorandum-86778, NASA Ames Research Center, Moffett Field, CA-94035, Nov. 1985, NASA TM-86778.
16. Perry, M.L., "The Effects of Leading and Trailing edge Deflections on the Performance of a Wortman FX 36-137 Airfoil at Low Reynolds Numbers", Masters Thesis, University of Notre Dame, Notre Dame, Indiana, 1985.
17. Peyret, Roger and Thomas, Taylor D., Computational Methods for Fluid Flow. New York: Springer-Verlag, 1983.
18. Roach, Patrick J., Computational Fluid Dynamics, Albuquerque: Hermosa Publishers, 1985.
19. Rubin, S.G. and Reddy, D.R., "Global PNS Solutions for Laminar and Turbulent Flow", AIAA Paper No. 83-1911.
20. Schlichting, Herman. Boundary Layer Theory (Seventh edition). New York: McGraw-Hill Book Co., 1979.
21. Sorenson, R.L., "A Computer Program to generate Two-Dimensional Grids About Airfoils Other Shapes", NASA Technical Memorandum 81198.
22. Steiger, Joseph L. and Chausse, Denny S., "Generation of Body-Fitted Coordinates Using Hyperbolic Partial Differential Equations", SIAM J. Sci. Stat. Comput. Vol. 4, December 1980.
23. Swanson, R.C. and Turkel, E., "A Multi-Stage Time-Stepping Scheme for the Navier Stokes Equations", ICASE Report No. 84-62, NASA Langley Research Center, Hampton, Virginia.

24. Thames, F.C., and others, "Numerical Solutions for Viscous and Potential Flow about Arbitrary Two-Dimensional Bodies Using Body-Fitted Coordinate Systems", Journal of Computational Physics, Vol. 24, 1977, pages 245-273.
25. Thompson, J.F., Warsi, Z.U.A. and Mastin, C.W., "Numerical Grid Generation, Foundations and Applications", New York: North Holland, 1985.
26. Vinokur, M., "On One-Dimensional Stretching Functions for Finite Difference Calculations", NASA Contractor Report 3313.
27. Visbal, M. and Knight, D., "Evaluation of the Baldwin-Lomax Turbulence Model for Two-Dimensional Shock-Wave Boundary Layer Interactions", AIAA 16th Fluid and Plasma Dynamics Conference, Denver Mass. July 1983, AIAA 83-1697.
28. Williams, B.R., "Further work on Airfoils at Reynolds Numbers between 3×10^5 and 1×10^6 ", 4th Symposium on Numerical Aspects of Aerodynamic Flows, Long Beach California, January 1989.
29. York, B.J., "Evaluation of the Baldwin Lomax Turbulence Model for a Class of Boundary Layer Flows", Masters Thesis, Dept. Mech. and Aero. Eng., Rutgers-The State University, New Burnswick, N.J., October 1984.

Vita

Flight Lieutenant Faran Hafeez [REDACTED]

[REDACTED] He graduated with distinction from the Pakistan Air Force College of Aeronautical Engineering in January 1982 with the degree of Bachelor of Engineering in Aerospace. He then served as maintenance engineer for a period of three years and was then assigned to a research and development unit, after serving in this capacity for two years he was selected for higher education in the United States of America at the Air Force Institute of Technology in 1987.

[REDACTED] [REDACTED]
[REDACTED]
[REDACTED]

ADA206138

REPORT DOCUMENTATION PAGE

Form Approved
OMB No. 0704-0188

1. REPORT SECURITY CLASSIFICATION UNCLASSIFIED			1b. RESTRICTIVE MARKINGS				
2a. SECURITY CLASSIFICATION AUTHORITY			3. DISTRIBUTION / AVAILABILITY OF REPORT Approved for public release; distribution unlimited.				
2b. DECLASSIFICATION / DOWNGRADING SCHEDULE							
4. PERFORMING ORGANIZATION REPORT NUMBER(S) AFIT/GAE/AA/89M-2			5. MONITORING ORGANIZATION REPORT NUMBER(S)				
6a. NAME OF PERFORMING ORGANIZATION School of Engineering		6b. OFFICE SYMBOL (If applicable) AFIT/ENY		7a. NAME OF MONITORING ORGANIZATION			
6c. ADDRESS (City, State, and ZIP Code) Air Force Institute of Technology Wright-Patterson AFB, OHIO 45433				7b. ADDRESS (City, State, and ZIP Code)			
8a. NAME OF FUNDING / SPONSORING ORGANIZATION		8b. OFFICE SYMBOL (If applicable)		9. PROCUREMENT INSTRUMENT IDENTIFICATION NUMBER			
8c. ADDRESS (City, State, and ZIP Code)				10. SOURCE OF FUNDING NUMBERS			
				PROGRAM ELEMENT NO.		PROJECT NO.	
				WORK UNIT ACCESSION NO.			
11. TITLE (Include Security Classification) NUMERICAL STUDY OF THE INFLUENCE OF LEADING AND TRAILING EDGE FLAPS ON THE PERFORMANCE OF AIRFOILS							
PERSONAL AUTHOR(S) Faran Hafeez, Flight Lieutenant., Pakistan Air Force							
13a. TYPE OF REPORT Thesis		13b. TIME COVERED FROM _____ TO _____		14. DATE OF REPORT (Year, Month, Day) 1989 March		15. PAGE COUNT	
16. SUPPLEMENTARY NOTATION							
17. COSATI CODES			18. SUBJECT TERMS (Continue on reverse if necessary and identify by block number)				
FIELD	GROUP	SUB-GROUP					
20	04						
19. ABSTRACT (Continue on reverse if necessary and identify by block number) Thesis Chairman: Ahmad Halim Associate Professor of Aerospace Engineering (See reverse side)							
20. DISTRIBUTION / AVAILABILITY OF ABSTRACT <input checked="" type="checkbox"/> UNCLASSIFIED/UNLIMITED <input type="checkbox"/> SAME AS RPT. <input type="checkbox"/> DTIC USERS				21. ABSTRACT SECURITY CLASSIFICATION			
22a. NAME OF RESPONSIBLE INDIVIDUAL Faran Hafeez, Flt. Lt., PAF.				22b. TELEPHONE (Include Area Code) 513-255-3030		22c. OFFICE SYMBOL AFIT/ENA	

The purpose of this study is to develop a code based on the Approximate Navier Stokes (ANS) equations (in the Vorticity Stream Function delta form). The Wortman FX 63-137 airfoil fitted with leading and trailing edge devices has been analyzed at low Reynolds Number (100,000) at various angles of attack and various deflection angles. results are compared to the experimental data. The agreement is very good at small angles of attack. However, at large angles of attack the disparity is larger, and improvements have been recommended which will resolve this disparity. Overall the present scheme produces very reasonable results, with good repeatability and fast convergence, and has the potential of being developed into an effective design tool.